Investigating Lightning-to-Ionosphere Energy Coupling Based on VLF Lightning Propagation Characterization

Erin Hoffmann Lay

A dissertation submitted in partial fulfillment of the
requirements for the degree of

Doctor of Philosophy

University of Washington

2008

Program Authorized to Offer Degree:
Physics

University of Washington
Graduate School

This is to certify that I have examined this copy of a doctoral dissertation by

Erin Hoffmann Lay

and have found that it is complete and satisfactory in all respects,
and that any and all revisions required by the final examining committee have been made.

Chair of the Supervisory Committee:

_____
Robert Holzworth

Reading Committee:

_____
Robert Holzworth

_____
Abram Jacobson

_____
Michael McCarthy

Date: _____

In presenting this dissertation in partial fulfillment of the requirements for the doctoral degree at the University of Washington, I agree that the Library shall make its copies freely available for inspection. I further agree that extensive copying of the dissertation is allowable only for scholarly purposes, consistent with "fair use" as prescribed in the U.S. Copyright Law. Requests for copying or reproduction of this dissertation may be referred to Proquest Information and Learning, 300 North Zeeb Road, Ann Arbor, MI 48106-1346, to whom the author has granted "the right to reproduce and sell (a) copies of the manuscript in microform and/or (b) printed copies of the manuscript made from microform."

Signature_____

Date_____

University of Washington

Abstract

Investigating Lightning-to-Ionosphere Energy Coupling Based on VLF Lightning Propagation Characterization

Erin Hoffmann Lay

Chair of the Supervisory Committee:
Professor Robert Holzworth
Department of Earth and Space Sciences

In this dissertation, the capabilities of the World-Wide Lightning Location Network (WWLLN) are analyzed in order to study the interactions of lightning energy with the lower ionosphere. WWLLN is the first global ground-based lightning location network and the first lightning detection network that continuously monitors lightning around the world in real time. For this reason, a better characterization of the WWLLN could allow many global atmospheric science problems to be addressed, including further investigation into the global electric circuit and global mapping of regions of the lower ionosphere likely to be impacted by strong lightning and transient luminous events.

This dissertation characterizes the World-Wide Location Network (WWLLN) in terms of detection efficiency, location and timing accuracy, and lightning type. This investigation finds excellent timing and location accuracy for WWLLN. It provides the first experimentally-determined estimate of relative global detection efficiency that is used to normalize lightning counts based on location. These normalized global lightning data from the WWLLN are used to map intense storm regions around the world with high time and spatial resolution as well as to provide information on energetic emissions known as elves and terrestrial gamma-ray flashes (TGFs). This dissertation also improves WWLLN by developing a procedure to provide the first estimate of relative lightning stroke radiated energy in the 1-24 kHz frequency range by a global lightning detection network.

These characterizations and improvements to WWLLN are motivated by the desire to use WWLLN data to address the problem of lightning-to-ionosphere energy

coupling. Therefore, WWLLN stroke rates are used as input to a model, developed by Professor Mengu Cho at the Kyushu Institute of Technology in Japan, that describes the non-linear effect of lightning electromagnetic pulses (EMP) on the ionosphere by accumulating electron density changes resulting from the interaction of the EMP of ten successive lightning strokes with the lower ionosphere. Further studies must be completed to narrow uncertainties in the model, but the qualitative ionospheric response to successive EMPs is presented. Results from this study show that the non-linear effect of lightning EMP due to successive lightning strokes must be taken into account, and varies with altitude, such that the most significant electron density enhancement occurs at 88 km altitude.

TABLE OF CONTENTS

Page

List of Figures v
List of Tables viii
Chapter 1: Introduction 1
1.1 Motivation for real-time global lightning detection 1
1.1.1 Practical Applications 1
1.1.2 Fundamental Geophysics 2
1.2 Types of Lightning 3
1.2.1 Cloud-to-Ground 3
1.2.2 In-cloud 5
1.3 Lightning Detection Systems 6
1.3.1 Satellite Detection 7
1.3.2 Regional Ground-Based Detection 8
1.3.3 Overview of World-Wide Lightning Location Network 9
1.4 Effects of Lightning Energy in the Earth System 10
1.4.1 Elves/sprites 10
1.4.2 Terrestrial Gamma-ray Flashes 13
1.5 Global Electric Circuit 15
1.6 Ionospheric Wave Propagation 17
1.7 Dissertation Outline 18
Chapter 2: World-Wide Lightning Location Network 20
2.1 Network Introduction 20
2.2 WWLLN Hardware 21
2.3 WWLLN Software 23
Chapter 3: Global Detection Efficiency and Location Accuracy 26
3.1 Overview 26
3.2 Brazil Integrated Network/WWLLN Comparison 26
3.2.1 Method 27

3.2.2 Results 28
3.2.3 Summary of Brazil Study 30
3.2.4 Advances in WWLLN since this study 31
3.3 FORTE/WWLLN Comparison 31
3.3.1 Overview 31
3.3.2 FORTE photodiode detector 32
3.3.3 WWLLN/PDD Comparison Methodology 33
3.3.4 Results 34
3.3.5 Conclusion 40
3.4 Detection range of WWLLN stations 40
3.5 Conclusion 45
Chapter 4: Global Mapping of Strong Lightning 46
4.1 Introduction 46
4.2 Land/ocean events in local time 46
4.3 Events in local time: higher resolution 51
4.4 Summary 52
Chapter 5: Narrow Bipolar Events and Ionospheric Propagation 54
5.1 Motivation 54
5.1.1 FORTE RF/WWLLN Comparison 54
5.1.2 Narrow Bipolar Events Hypothesis 55
5.2 Narrow Bipolar Events: WWLLN/LASA coincidence study 56
5.2.1 Method 56
5.2.2 Results 56
5.3 Conclusions 61
Chapter 6: Experimental evidence of energetic lightning effects on ionosphere and magnetosphere 63
6.1 WWLLN/ISUAL elves comparison 63
6.1.1 Motivation 63
6.1.2 Method 63

6.1.3 Results 64
6.1.4 Discussion 70
6.2 WWLLN/RHESSI TGF comparison 71
6.2.1 Motivation 71
6.2.2 Method 71
6.2.3 Results 71
6.2.4 Summary 74
Chapter 7: Lightning stroke radiated VLF energy 75
7.1 Motivation to provide stroke energy 75
7.2 Absolute Calibration 75
7.2.1 Determining A_n by using narrowband VLF Transmitters 77
7.2.2 Frequency response 80
7.2.3 Summary and suggestions for the future 83
7.3 Relative energy radiated as determined by a single station 84
7.4 Relative Calibration 86
Chapter 8: Modeling Lightning EMP/Ionospheric Interaction 92
8.1 Overview 92
8.2 Model Formulation 93
8.3 In situ validation of EM code 96
8.4 Relaxation of enhanced electron density. 98
8.5 Accumulated enhancements due to successive lightning strokes. 100
Chapter 9: Conclusion and Future Work 110
9.1 World-Wide Lightning Location Network Characterization 110
9.2 Findings on energetic events correlated with lightning 111
9.3 Modeling of lightning electromagnetic pulse 112
9.4 Future Work 113
9.4.1 WWLLN Characterization 113
9.4.2 Lightning/Ionospheric Coupling 114
9.4.3 Narrow Bipolar Events 114

9.4.4 Global electric circuit..... 115
References..... 116
Appendix A: Schematics for WWLLN Service Unit and Preamplifier..... 124

LIST OF FIGURES

Figure Number ..... Page

1.1 Examples of electric field changes due to CG lightning 4

1.2 Example of electric field change due to NBE lightning stroke 6

1.3 Averaged global flash density [Christian et al., 2003] 7

1.4 Image of a sprite and an elve 11

1.5 Cartoon of current theory of TGF production [Smith et al., 2007] 15

1.6: A schematic representation of the global electric circuit [Roble and Tzur 1986] ... 16

1.7 Diurnal variation of fair weather electric field and global thunderstorm activity [Roble and Tzur 1986] 16

2.1 WWLLN map of real-time lightning locations 20

2.2 Cartoon schematic of a WWLLN VLF receiving station 22

2.3 Example 64-sample waveform of a lightning sferic 23

3.1 Region of Brazil/WWLLN comparison 28

3.2 Histogram of return stroke peak currents measured by the BIN 29

3.3 Location offsets of shared WWLLN-BIN events. 30

3.4 Time-difference histogram of WWLLN-sferic time minus PDD-trigger time 34

3.5 WWLLN station locations (January 2005) w/ 6 broad region borders 35

3.6 A superposed epoch of PDD waveforms with WWLLN coincidences 39

3.7 Ratio of events detected by Darwin to events detected by network as a whole 41

3.8 Station detection range model for noon 44

3.9 Station detection range for midnight 44

4.1 One year of WWLLN flash density data vs time 47

4.2 Data from Figure 4.1 separated into six broad regions 48

4.3 Overlaid, normalized land data from Figure 4.2 49

4.4 Five days of land/ocean WWLLN flash density data 50

4.5 Percentage of total lightning in nighttime in each region 51

4.6 Total number of nighttime counts for March 2006 – February 2007 53

5.1 Spectrogram of an example of strong IC lightning 55

5.2 Full NBE waveform as detected by 5 LASA stations 57

5.3 Range-normalized electric field of a NBE 58
5.4 Power spectrum of a NBE 59
5.5 Full FP waveform as detected by 5 LASA stations 60
5.6 Ratio of VLF power to total power versus total VLF power 61
5.7 VLF to total power for only coincident WWLLN/LASA sferics 61
6.1 Time difference histogram of coincident WWLLN lightning/ISUAL elves 64
6.2 Locations of elves and coincident WWLLN lightning 65
6.3 Time differences (zoomed) between ISUAL elve and WWLLN stroke 65
6.4 Distance separation between WWLLN location and ISUAL estimated location 66
6.5 Latitude and longitude differences between WWLLN and elve locations 66
6.6 ISUAL-to-WWLLN distance vs elve-to-WWLLN distance 67
6.7 Spatial configuration: ISUAL location, estimated-elve, and WWLLN lightning 68
6.8 More relative locations of satellite, elve location estimate, WWLLN location 68
6.9 Elves (27 October 2005) and all WWLLN lightning within 2 hours of elves 69
6.10 Six non-coincident elves and WWLLN-located lightning within 2 hours 70
6.11 Time difference histogram of coincident WWLLN lightning/TGFs 72
6.12 Locations of all TGFs and coincident TGFs/WWLLN lightning 72
6.13 Time difference (zoomed) between TGF time and WWLLN stroke time 73
6.14 Distance between WWLLN location and RHESSI sub-satellite point 73
7.1 Average value of amplitude of NWC and NPM transmitters 79
7.2 Values of $A_{Dunedin}$ over time 79
7.3 Example spectrogram of frequency calibration procedure 81
7.4 Frequency response of 3 WWLLN stations 81
7.5 Frequency response of preamp and sound card, alone and together 82
7.6 Histogram of the 509 lightning strokes in relative-energy case study 85
7.7 Map of lightning strokes in relative-energy case study 85
7.8 Relative stroke energy estimates from one storm detected by 2 stations 87
7.9 The best fit for relative energy 88
7.10 Relative stroke energy estimates from two storms detected by 2 stations 88

7.11 LWPC-predicted spectra for a simulated stroke at 9N, 95.5W 90
8.1 Lightning current pulse shape used in 2D-EMP model 94
8.2 Comparison of rocket-measured electric field with 2-D EMP model 97
8.3 Comparison of rocket-measured E-field with 2-D EMP model (4-kHz filter) 98
8.4 Numerically-calculated relaxation times for different altitudes 100
8.5 Cumulative lightning probability vs. lightning peak current [Rodger et al., 2005] 101
8.6 Electron density profiles from 2D-EMP model 103
8.7 Percentage change in electron density from 2D-EMP model 103
8.8 Electron density at 92, 90, 88, and 85 km altitude after each successive stroke 105
8.9 Percent change in N_e for 92, 90, 88, 85 km altitude after each successive stroke .. 105
8.10 Perturbed electron density profile 106
A.1 Schematic of WWLLN service unit 124
A.2 Schematic of WWLLN preamplifier 125

LIST OF TABLES

Table Number ..... Page

3-A Active station locations during Brazil comparison study 27

3-B Results of WWLLN/PDD regional comparison 2005 36

3-C Results of WWLLN/PDD land/ocean comparison 37

3-D Results of WWLLN/PDD land/ocean coincidence comparison 38

7-A Properties of narrowband VLF transmitters NPM and NWC 77

ACKNOWLEDGEMENTS

I would like to acknowledge the support of the University of Washington Space Physics Group in the Department of Earth and Space Science. In particular, I would like to thank my advisor, Prof. Robert Holzworth, for his guidance, support, and suggestions over the years. I would also like to thank my secondary advisors, Prof. Abram Jacobson and Prof. Michael McCarthy for their support and guidance and their excellent comments on many drafts of this dissertation. I would also like to thank Prof. Jacobson, for teaching me data analysis techniques and critical thinking, and Prof. McCarthy, for teaching me hardware building and testing as well as critical thinking. I thank Prof. Robert Winglee for teaching me the basics of computer modeling. I very much appreciate the many discussions I have had with Dr. Jeremy Thomas regarding my research. I also appreciate the help and distraction provided to me by fellow graduate students and my officemates Michael Kokorowski and Ariah Kidder. I would like to acknowledge Dr. Mengu Cho for providing me with his lightning EMP model for use in this dissertation, and Dr. Harald Frey and Dr. David Smith for providing ISUAL and RHESSI data, respectively, for use in this dissertation. Finally, I am grateful for my wife, Amy, for her unending support and presence that made my success in graduate school possible.

DEDICATION

To Dad

Chapter 1: Introduction

In this dissertation, the capabilities of the World-Wide Lightning Location Network (WWLLN) are analyzed in order to study the interactions of lightning energy with the lower ionosphere. Section 1.1 describes the motivation for real-time global lightning detection in terms of practical applications and geophysical studies. A brief introduction to different types of lightning is provided in Section 1.2. Section 1.3 describes regional ground-based lightning detection networks and current lightning detection satellite capabilities, as well as an overview of the WWLLN. The effects of lightning energy in the Earth system are described in Section 1.4. The global electric circuit is explained in Section 1.5 and radio wave propagation in the Earth-Ionosphere waveguide is summarized in Section 1.6. A dissertation outline is presented in Section 1.7.

1.1 **Motivation for real-time global lightning detection**

Developments in very-low-frequency (VLF; 3-30 kHz) electromagnetic lightning detection and global-positioning-system (GPS) timing now allow both continental and oceanic lightning detection with comparable efficiency. In particular, the World-Wide Lightning Location Network (WWLLN) monitors global lightning in real-time [Dowden et al., 2002; Lay et al., 2004; Rodger et al., 2004, 2005a]. VLF lightning monitoring with WWLLN is intrinsically long range, because it takes advantage of, rather than rejects, long-range propagation paths in the Earth-ionosphere waveguide. The waveguide propagation paths available in VLF allow useful detection over 10^4 km.

1.1.1 *Practical Applications*

A real-time, global lightning detection system has a variety of applications in the scientific, commercial, and governmental sectors. Scientifically, it could provide better global tracking of severe storms, especially storms and hurricanes over the oceans. Its seasonal and yearly averaged data could be used as an indicator of global climate change [Schlegel et al., 2001]. Lightning estimates in areas with poor radar coverage

can be used to estimate convective rainfall as well as to predict flash flooding [Tapia et al., 1998]. Global lightning data could be used in the commercial sector for shipping or aviation purposes. In fact, several airlines have already begun using WWLLN data to monitor severe convective regions over the oceans. Global lightning data could also be used in the governmental sector for problems such as forest fire management and the initialization of weather forecast models.

1.1.2 *Fundamental Geophysics*

Over the past few decades, a handful of rocket flights in the ionosphere (e.g. Kelley et al., 1985; Li et al., 1991) have detected electric field transients due to lightning strokes at altitudes of 70-400 km, providing the first direct in situ evidence that VLF lightning generated waves can penetrate the ionosphere. Also, it has been shown that lightning generates whistler wave radiation that can propagate into the outer magnetosphere (Holzworth et al. 1999). Lightning-generated whistler waves can also interact with electrons in the radiation belts, causing lightning-induced electron precipitation (Goldberg et al. 1986). Extremely high energy gamma-ray bursts coming from the Earth's atmosphere, now termed terrestrial gamma-ray flashes (TGFs), were first unexpectedly observed by the BATSE satellite (Fishman et al. 1994). TGFs are another indication of very energetic coupling of lightning with the magnetosphere.

In addition to lightning energy coupling with the upper ionosphere and magnetosphere, lightning has the ability to affect conductivity and electron density in the lower ionosphere, which could subsequently affect the ability of lightning energy to couple into the upper ionosphere and magnetosphere. Access to real-time global lightning data could allow a deeper investigation of these effects. It could provide a method to track lightning-driven ionospheric perturbations globally in time and space. These results could provide a better understanding of the daily variation of the global electric circuit [Volland, 1984]. Also, data on global variation in strong lightning would be extremely helpful in estimating the direct impacts on the local, regional and global atmosphere of transient luminous events (TLEs), such as sprites, elves, and halos [Rodger, 1999].

The focus of this dissertation is to address the following questions:

1. How significant is nighttime lightning in perturbing lower ionospheric electron density?
2. What regions of the world have the largest lightning-induced electron density perturbation? How do these regions vary in time?

In order to answer these questions, as well as other geophysical questions, this dissertation focuses on obtaining a better understanding of the WWLLN by addressing the following questions:

1. What are the characteristics of WWLLN in terms of detection efficiency, timing and location accuracy, lightning type, and lightning strength?
2. How do these characteristics vary spatially and temporally?
3. How does one determine lightning stroke radiated VLF energy using the WWLLN?

1.2 **Types of Lightning**

There are many different types of lightning, and even within one family of lightning type, there is no "typical" lightning stroke. This makes studying and modeling the effects of lightning difficult, since each stroke has a different current profile, and radiates different amounts of energy. Average global flash rates have been found to be 44 ± 5 flashes/sec [Christian et al., 2003].

1.2.1 *Cloud-to-Ground*

The type of lightning that most concerns human safety is called cloud-to-ground (CG) lightning. CG lightning strokes form a conductive path between the cloud and ground, along which large amounts of current flow due to a potential difference between the cloud and ground. Because of these large currents flowing between cloud and ground, CG lightning is a safety concern, and humans have developed lightning

detection networks to monitor it. Some of these networks will be discussed in this dissertation.

Within the CG lightning categorization, there are two main types: negative and positive CG lightning. Negative CG lightning transfers negative charge from the cloud to the ground and comprises about 90% of CG strokes. Because the negative charge center of clouds are typically lower in altitude than the positive charge center, stroke channel lengths for negative CGs are typically 5-8 km. It is the current flowing in these kilometer-length channels that allows the generation of radiation with km-scale wavelengths (3-30 kHz, very low frequency; VLF). Figure 1.1(i) shows an example of an electric field waveform as detected by a lightning receiver 474 km from the lightning stroke.

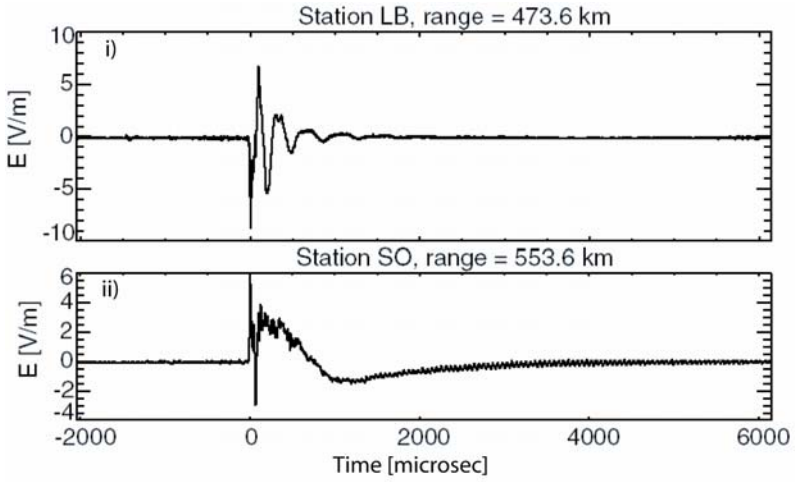

Figure 1.1: Example of electric field changes due to lightning for a i) negative CG stroke and a ii) positive CG stroke, with electric field in V/m and time in μs. The trigger for each lightning stroke is fixed to 0.0 μs on the horizontal axis. The Los Alamos Sferic Array receiver station name and detection range are listed above each plot. Reproduced from Smith et al. [2002].

As mentioned above, there is no "typical" lightning stroke, but statistics have been gathered for a number of CG strokes, and these indicate that negative CG lightning events (flashes) often consist of more than one stroke. The first stroke is typically the strongest, with a median peak current of ~30 kA [Rakov and Uman, 2003 p146]. CGs with large peak currents (>~50 kA) are often able to generate "elves", and optical phenomena about thunderstorms that will be discussed in more depth in section 1.4.1 of

this dissertation [Barrington-Leigh and Inan, 1999]. Negative CGs have an average of ~4 subsequent strokes in a flash that are typically weaker than the first stroke with a median peak current of ~12 kA. Current flows for ~75 μs during the first stroke of flash, and for ~32 μs during the subsequent strokes [Rakov and Uman, 2003 p144-6].

The second main type of CG lightning is positive lightning. Positive CGs often have longer channel lengths due to the fact that the positive charge center in the cloud is usually higher than the negative charge center. Positive CGs are unlikely to have more than one stroke in a flash [Rakov and Uman, 2003], and they also often transfer larger amounts of charge to the ground (median at 80 C as opposed to 7.5 C for negative CGs) than negative CGs because the current flows for a longer amount of time in the stroke channel (median 230 μs) [Rakov and Uman, 2003 p215]. Figure 1.1(ii) shows an example of the electric field change due to a positive CG, plotted versus the same time axis as the example negative CG in Figure 1.1(i).

Often, the charge-moment of positive CGs is calculated as an estimate of strength. The charge-moment is the product of the amount of charge moved from cloud-to-ground (in Coulombs) times the distance moved (in km). It is thought that positive CGs with charge-moments larger than ~350-600 C-km could be correlated with an optical phenomena above thunderstorms called “sprites” [Cummer and Lyons, 2005]. Sprites will be discussed in more detail in Section 1.4.1 of this dissertation.

1.2.2 *In-cloud*

Although CG strokes are well-studied because of the hazards they pose to humans, the most typical type of lightning is actually in-cloud (IC) lightning. This type of lightning occurs between different charge layers within the cloud or between two clouds. It is typically weaker than CG lightning, meaning that it has lower peak currents and transfers smaller amounts of charge over shorter distances. The most common type of IC lightning has a flash duration of anywhere between 15 and 660 ms [Rakov and Uman, 2003 p325]. Because it is about 3 times as frequent on average as CG lightning

[Rakov and Uman, 2003 p44], and it occurs higher in altitude than CG strokes, IC lightning could have significant affects on the atmosphere and ionosphere.

A newly-discovered type of IC lightning, named a Narrow Bipolar Event (NBE), transfers charge between cloud charge layers, but is unusually strong (peak currents ~30-40 kA) and very fast (~25 μs) compared to common IC events [LeVine, 1980; Willett, 1989; Smith et al., 1999]. An example NBE electric field waveform is shown in Figure 1.2. One must note the change in time scale when comparing the NBE duration to CG electric field waveforms shown in Figure 1.1.

Recently, this subset of IC lightning has been a focus of lightning research because it has also been correlated with changes in storm stages that indicate increased convective activity [Wiens et al., 2008]. It is also the most predominant type of lightning measured by high frequency (3-300 Mhz) radio-wave instruments on satellites [Suszcynsky et al., 2000a]. Therefore, it is possible that NBE measurements could be a sensitive indicator of severe storms for satellite-based instruments.

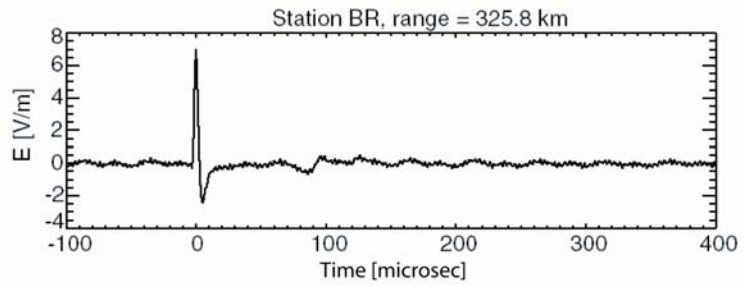

Figure 1.2: Example of electric field change due to NBE lightning stroke. Vertical axis represents electric field in V/m, horizontal axis shows time in μs. The Los Alamos Sferic Array receiver station name and detection range are listed above the plot. Reproduced from Smith et al. [2002].

1.3 **Lightning Detection Systems**

In order to determine location and timing accuracy, detection efficiency, and stroke type detected by WWLLN, we compare WWLLN data to lightning detected by regional ground-based networks and satellite-based lightning detection instruments. This section will describe the detection methods for satellite-based instruments and regional ground-based networks. The section will also provide a brief overview of WWLLN.

1.3.1 *Satellite Detection*

During the past decade, satellite optical lightning imagers, the Optical Transient Detector (OTD) [Boccippio et al., 2000a] and the Lightning Imaging Sensor (LIS) on the Tropical Rainfall Measuring Mission (TRMM) satellite [Christian et al., 1999] have provided a meaningful global map of average lightning occurrence. These two instruments were launched on satellites in low-Earth orbit. The OTD was launched in 1995 aboard the Microlab-1 satellite and had an orbital inclination of ± 70°. This inclination allowed OTD to view nearly all lightning-producing regions on Earth for an average duration of ~2 minutes about 400 times a year. The field of view of the OTD was 1300 x 1300 km^2. The imaging instrument locates lightning within the field of view of a 128 x 128 pixel CCD camera. The optical signal is processed to determine the lightning signal over the background noise. The system is less sensitive to lightning during daytime as the background light levels are higher, and it is more difficult to distinguish a lightning signal from background light [Christian et al., 2003]. The LIS instrument aboard the TRMM satellite has similar hardware and processing algorithms, although its orbit is slightly different. TRMM was launched in 1997 into a ± 35°–inclination orbit and has a field of view of 600 x 600 km^2. The averaged yearly global lightning flash density as determined by OTD is shown in Figure 1.3.

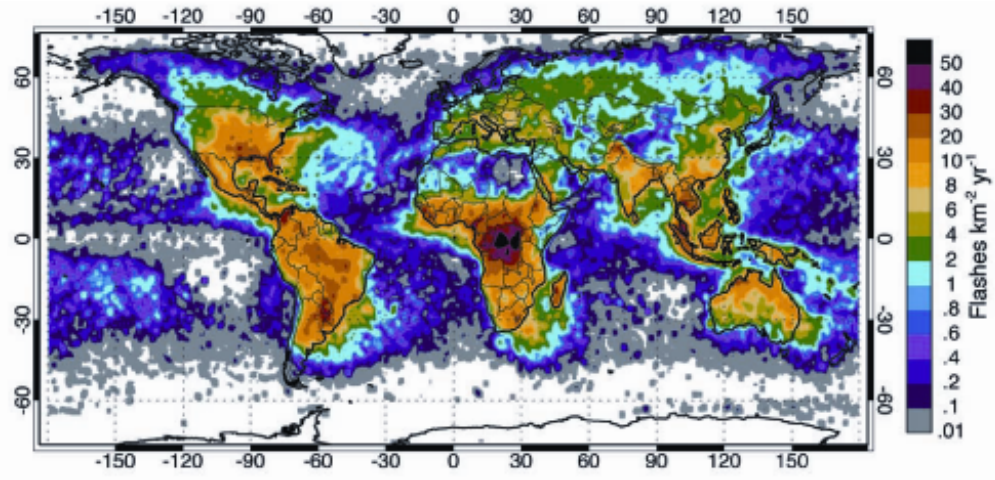

Figure 1.3: Averaged global flash density in km^{-2} yr^{-1} from 5 years of OTD satellite lightning data. Reproduced from [Christian et al., 2003].

In Figure 1.3, the prevalence of lightning over land versus over ocean is apparent. This figure also shows that central Africa is the region on Earth with the highest flash density.

Several years of observations from these two instruments have allowed lightning seasonal and local-time variations to be statistically separated, resulting in a comprehensive lightning distribution versus local time, season, and geographic position [Christian et al., 2003; Boccippio et al., 2000b; Petersen and Rutledge, 2001]. Nesbitt and Zipser [2003] have used data from the TRMM satellite to study the diurnal cycle of precipitation features over land and ocean. However, the infrequency of satellite observations over a given point, and the precession of the satellite's orbit, together, cause years of cumulative data to be required to separate local-time variability from other changes, such as seasonal and geographic effects. In the interest of studying variabilities on a daily basis and in connection to certain storms, real-time global detection by WWLLN is also important.

While the OTD and LIS instruments have provided extremely useful global averages for the lightning community, their data has not been used in comparison to WWLLN data. Instead, we have used data from the FORTE photodiode detector and the radio frequency (RF) antenna lightning detection instruments on the FORTE satellite. These instruments will be described in Sections 3.3.2 and 5.1.1, respectively.

1.3.2 *Regional Ground-Based Detection*

Ground-based regional detection systems, such as the National Lightning Detection Network (NLDN) in the U.S. [Cummins et al., 1998], provide detailed information about lightning strokes in real-time, but only for limited areas on Earth. These networks typically measure lightning radiation in the low frequency range (30-300 kHz) and require a density of 1 receiver every 100-300 km due to signal attenuation. About 300 sensors are deployed in the United States for the NLDN. Ground-based regional networks usually have very high detection efficiencies (>95%) and are able to estimate stroke peak current and lightning type based on the electric field waveform.

This dissertation uses lightning data from 2 regional, ground-based networks, the Brazil Integrated Network (BIN; now called Brazil-Southeast 2 [Pinto et al., 2007]) and the Los Alamos Sferic Array (LASA). Each of these networks is similar to NLDN, but on a smaller scale. The BIN detects lightning in Southern Brazil, and LASA detects lightning in the Great Plains of the U.S. LASA data have the advantage that complete lightning waveforms are available in addition to the locations.

1.3.3 *Overview of World-Wide Lightning Location Network*

The WWLLN has been providing continuous accurate locations and times for lightning strokes globally since August 2003 [Lay et al., 2004; Rodger et al., 2005a; Jacobson et al., 2006]. A variety of comparisons have been made between WWLLN lightning locations and regional ground-based network locations. Jacobson et al. [2006] has shown that in 2004 WWLLN had a flat detection efficiency in the Southeastern U.S. of ~4% for all types of strokes with peak current magnitude above 40 kA by comparison to LASA. The value of 4% from this study may be off by 25-30% because it assumed a LASA detection efficiency of 100% while LASA actually has a slightly lower detection efficiency. Rodger et al., [2004, 2005a] have studied WWLLN capabilities in Australia and New Zealand. We will take these detection efficiencies into account to normalize WWLLN flash rates when using WWLLN to monitor the global effect of lightning EMP on the lower ionosphere. The comparisons between WWLLN and other lightning detection networks will be discussed in more detail in Chapter 3.

The WWLLN has two main advantages in addressing the question of interest of this dissertation: (1) The WWLLN is the only lightning location network with the capability to continuously monitor the location of lightning strokes around the entire world. Thus it is the only network with the capabilities to expand the study of the effects of lightning energy to a global level. (2) The WWLLN detects all types of lightning strokes that have peak currents with magnitudes above ~40 kA with a constant detection efficiency [Jacobson et al., 2006]. Since the magnitude of the lightning electromagnetic pulse is dependent on the peak current, and not lightning type, it is

important to monitor all types of lightning with strong peak current. Regional networks such as the NLDN only report cloud-to-ground lightning activity.

1.4 **Effects of Lightning Energy in the Earth System**

Over the past few decades, a handful of rocket flights in the ionosphere [e.g. Kelley et al., 1985; Li et al., 1991] have detected electric field transients due to lightning strokes at altitudes of 70-400 km, providing the first direct in situ evidence that VLF lightning-generated waves can penetrate the ionosphere. Also, it has been shown that lightning generates whistler wave radiation that can propagate into the outer magnetosphere [Holzworth et al., 1999]. Lightning-generated whistler waves can interact with electrons in the radiation belts, causing lightning-induced electron precipitation [Goldberg et al., 1986]. Optical phenomena that occur above thunderstorms, known as transient luminous events (TLEs), provide evidence of lightning energy coupling to the atmosphere and lower ionosphere. We will describe two main types of TLEs (sprites and elves) in Section 1.4.1. Extremely high energy gamma-ray bursts, now termed terrestrial gamma-ray flashes (TGFs), have been observed as originating from the Earth's atmosphere [Fishman et al., 1994], and will be described in more detail in Section 1.4.2. The research in this dissertation will focus on energy coupling to the lower ionosphere from the lightning electromagnetic pulse (EMP), of which elves are optical evidence, and touch briefly on energy radiated into the magnetosphere via TGFs.

1.4.1 *Elves/sprites*

Lightning has the ability to affect conductivity and electron density in the lower ionosphere, which could subsequently affect the ability of lightning energy to couple into the upper ionosphere and magnetosphere. Transient luminous events (TLEs), such as sprites and elves, are evidence of lightning energy coupling with the lower ionosphere via quasi-electrostatic as well as electromagnetic fields, and can cause

ionization, heating and optical emissions in the lower ionosphere [Inan et al., 1991, Tarenenko et al., 1993, Fukunishi et al., 1996].

Sprites are optical phenomena that occur above thunderstorms between 40 to 90 km altitude and last for 10s of ms [Sentman et al., 1995; Boeck et al., 1995]. Sprites are associated with large electrostatic fields caused by lightning strokes that transfer a large amount of charge to the ground from a given altitude (more than ~350-600 C-km) [Cummer and Lyons, 2005]. The majority of observed sprites have occurred in association with positive cloud-to-ground strokes, but also have been observed rarely in association with negative CGs [Barrington-Leigh et al., 1999, Taylor et al., 2008]. The large altitude extent of the sprite (50-80 km) indicates that changes in conductivity and electron density could arise over a large altitude range. This could be significant in cloud-to-ionosphere charge movement as well as in lightning energy propagation in the Earth-ionosphere waveguide. Figure 1.4(i) shows a sprite imaged by the Tohoku University Sprite Group.

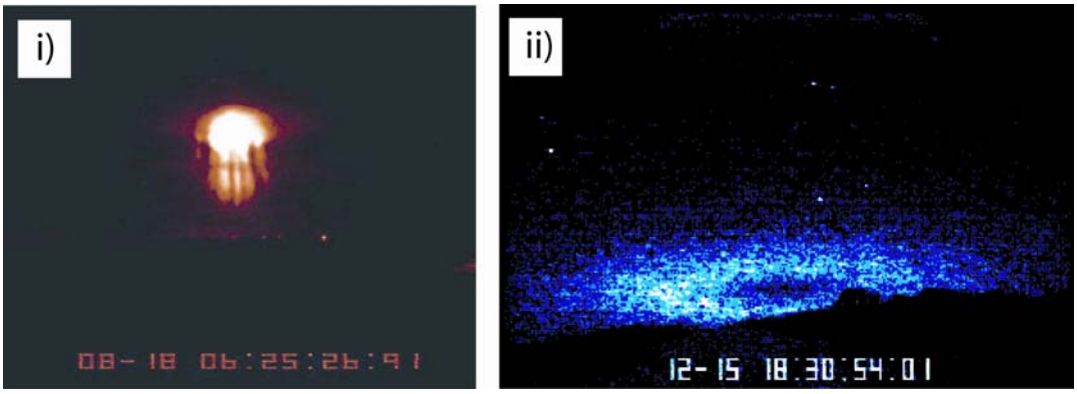

Figure 1.4: Image of i) a sprite and ii) an elve taken by the Tokohu University Sprite Group (http://pat.geophys.tohoku.ac.jp/~thermo/sprites/).

Elves are another type of TLE, but are caused by the lightning electromagnetic pulse (EMP) instead of a quasi-electrostatic field. The lightning EMP expands outward from a high peak current (>50 kA) cloud-to-ground stroke: [Barrington-Leigh and Inan, 1999]. When it reaches an altitude of 85-95 km after ~1 ms, its electric field can interact with the ionospheric plasma, causing optical excitation and secondary ionization. The

elves themselves are the optical emissions, which expand in a ring shape and last 1 to 3 ms. The first images of elves were published in the work of Fukunishi et al., [1996]. Figure 1.4(ii) shows an elve imaged by the Tohoku University Sprite Group. They are more difficult to image than sprites due to the fact that they are produced just ~1 ms after the lightning stroke. If the lightning stroke is visible in the field of view of the imager, then it will overwhelm the sensor and the elve will likely not be visible. Recent successful imaging of elves has occurred by allowing the Earth's limb or cloud cover to obscure the lightning stroke and leave the elve visible, or by sensitive electronics and sophisticated processing algorithms [Frey et al., 2005].

Barrington-Leigh and Inan [1999] have shown by observing elves with a photometric array that the EMP from lightning can interact with a region of the lower ionosphere up to 700 km in diameter. Mende et al. [2005] have reported enhanced electron density in the same region as a detected optical emission from an elve. These observations indicate that the electromagnetic pulse from strong lightning strokes could be creating enhanced electron density over a large region of the lower ionosphere. The ISUAL instrument on the FORMOSAT-2 satellite has been operating since 2004, detecting sprites, sprite halos and elves. In areas of the world with regional ground-based detection networks, some of these detected TLEs have been correlated with possible causative lightning strokes. To better understand the global dynamics of these elves, global lightning detection is needed. Only WWLLN can provide this lightning detection coverage. By monitoring the locations and stroke energies of lightning strokes globally and comparing them to detected TLEs, we could learn what types of lightning storms are connected with energetic events in different regions of the world. From this information it may be possible to predict what conditions of strong lightning cause the greatest effects on the lower ionosphere, and which regions of the world will be affected at any given time.

Given that making in situ measurements of lightning-driven fields in the lower ionosphere is very difficult, and has only been accomplished a handful of times, models

of the interaction between the lightning stroke and that region can be illuminating. Various models predict the interaction between single lightning strokes and the lower ionosphere and are consistent with optical observations of TLEs [Taranenko et al., 1993; Fernsler and Rowland, 1996; Pasko et al., 1997; Cho and Rycroft, 1998]. These models indicate that lightning causes electron heating and ionization of the lower ionosphere that affects local conductivity and electron density. It has also been proposed that in severe thunderstorms with high flash rates of strong lightning strokes, the time between flashes could be smaller than the decay time for ionization changes of 10-100 s, allowing lightning-induced electron density increases to accumulate in the lower ionosphere locally [Barrington-Leigh and Inan, 1999]. By using the electromagnetic model developed in Cho and Rycroft [1998], Rodger et al. [2001] predicted a possible ten-fold increase in nighttime lower ionospheric electron density caused by the accumulated effects of NLDN-located lightning. We will improve on this study by taking into account the non-linear response of electron density variations due to lightning EMP. We will also expand this study globally using WWLLN lightning flash rates of strokes with large amounts of radiated energy.

In summary, previous research based on observations and models of elves indicates that thunderstorms with high flash rates of strong lightning strokes could cause an accumulated increase of electron density and conductivity in the lower ionosphere, a key region for the coupling of lightning energy with the upper ionosphere and magnetosphere.

1.4.2 *Terrestrial Gamma-ray Flashes*

Terrestrial Gamma-ray Flashes (TGFs) are high-energy gamma-rays that have been detected in space as originating from the Earth. These events are a relatively new area of lightning physics, and much progress has been made in the field in the past 5 years. TGFs were first unexpectedly observed by the BATSE satellite that was developed to study gamma-rays from the sun and beyond [Fishman et al., 1994]. TGFs are another indication of very energetic coupling of lightning with the magnetosphere. Since 2002,

the RHESSI spacecraft has detected hundreds of TGFs, which have been used to correlate lightning strokes and TGFs [Smith et al., 2005]. Smith et al. [2005] report an estimated ~50 TGFs per day globally. The mechanism behind TGFs as well as the manner in which they are able to reach the upper ionosphere without severe attenuation are still under investigation. The following are the main questions initially posed regarding TGFs:

Are they associated with lightning strokes, or with some other part of the lightning process? If they are associated with lightning, what type of stroke, and what strength of stroke (either in peak current or charge moment change) are they associated with? Are the gamma-rays beamed away from the source or isotropically radiated? What is the cause of the few extremely energetic TGFs that were detected over regions with no lightning?

Over the past five years, our understanding of TGFs has grown considerably. The contributions from this dissertation research will be explained in Section 6.2, but this introduction explains the current state of understanding. It is now understood that TGFs are associated with the lightning stroke itself, and not some other process in the cloud. TGFs do not seem to be associated with strokes having large charge-moment changes [Cummer et al., 2005]. The process by which TGFs are now thought to be generated is illustrated in Figure 1.5. Primary electrons produced by the lightning stroke are accelerated by relativistic runaway breakdown. Those electrons emit bremsstrahlung gamma-rays before being stopped by collisions with neutral molecules. The gamma-rays then Compton scatter without confinement to magnetic-field lines and some are able to reach the spacecraft altitude of 600 km. Electrons produced near top of atmosphere can escape along magnetic-field lines [Smith et al., 2007, Dwyer and Smith, 2005] and are thought to be the cause of extremely high energy TGFs detected far from lightning areas.

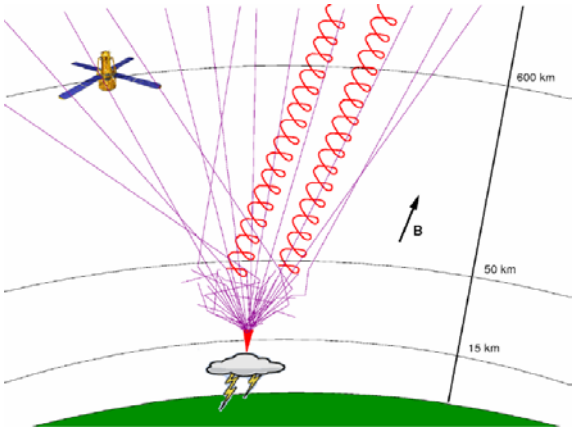

Figure 1.5: Cartoon of current theory of TGF production. Red cone is original electron beam, purple lines are gamma-ray paths from Compton scattering, red spirals show electrons produced near the top of the atmosphere traveling along magnetic field lines (Reproduced from Smith et al., [2007]).

1.5 **Global Electric Circuit**

The global electric circuit (GEC) is the name used to describe the "spherical capacitor" electrical system formed between the conducting Earth and conducting upper atmosphere and ionosphere. An average 300 kV potential exists between the Earth and ionosphere [Roble and Tzur, 1986]. The region between the two is filled with air, which acts as a leaky resistor because of non-zero conductivity. It has long been hypothesized that thunderstorms act as the generator in this circuit, providing current to the ionosphere and maintaining the potential difference [Wilson, 1920]. In fair weather regions, the evidence of this electrical circuit is in the form of the "fair weather return current" which is a current from the ionosphere to Earth of 1 to 2 pA/m^2. Integrating over all fair weather regions gives a total ionosphere-to-Earth current of an average of ~1000 kA. If there was no mechanism to maintain the Earth/ionosphere potential difference, a current of this magnitude would allow the capacitor to discharge within ~40 minutes [Roble and Tzur, 1986]. Therefore, it is hypothesized that ~1000 thunderstorms globally each provide about 1 kA of current up to the ionosphere. A cartoon illustration of this hypothesis of the global circuit is shown in Figure 1.6.

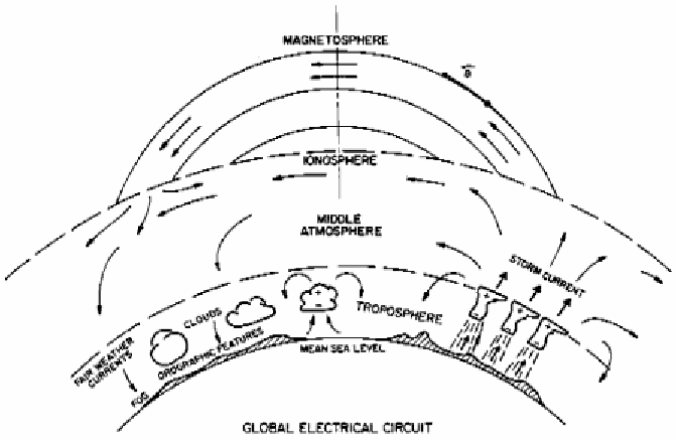

Figure 1.6: A schematic representation of the global electric circuit as hypothesized by Wilson [1920] (reproduced from Roble and Tzur [1986].

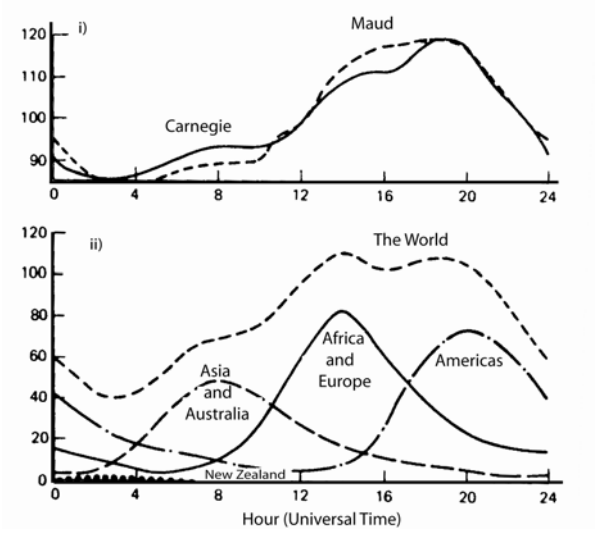

Figure 1.7: Yearly-averaged diurnal variation of (i) fair weather electric field over the oceans as detected on the Carnegie and Maud ships [Parkinson and Torrenson, 1931], and of (ii) global thunderstorm activity [Whipple and Scrase, 1936] (Reproduced from Roble and Tzur [1986]).

Figure 1.7 shows that long term averages of fair weather electric field in local time (Figure 1.7(i)) correspond well with averaged number of thunderstorms as measured in local time (Figure 1.7(ii)). The peak number of thunderstorms occur around 1400 universal time (UT). The plot also shows the contributions of thunderstorms from individual continental land masses. Typically the heating and cooling of land masses

causes increased thunderstorms in the local afternoon. By converting all local times to UT, one can add the different continental thunderstorm contributions to produce the "world" distribution shown in Figure 1.7(ii) [Whipple and Scrase, 1936].

Although thunderstorms have been hypothesized for nearly a century as the generator for the global electric circuit, there have not been detection capabilities available to test this prediction thoroughly. Only in the past 35 years have lightning detection networks been set up in certain regions [Cummins, 1998] and satellites to monitor weather have been launched (Christian et al., 2003). However, as mentioned in Section 1.3, regional networks are limited to small coverage regions and low-Earth orbiting satellites can only monitor a small region at a time and must average over months to determine global activity. To truly address the question of the generator of the GEC and the daily variabilities in the GEC, one must have a method to detect all thunderstorms globally all the time. In the work of Holzworth et al. [2005a], data from the early stages of WWLLN were used in comparison to simultaneously recorded vertical return current detected via electric field sensors on stratospheric balloons. While the detection efficiency of WWLLN was not well characterized at that time, this study indicated that WWLLN could provide an opportunity to more thoroughly investigate the correlation between total global thunderstorm activity and vertical return current.

1.6 **Ionospheric Wave Propagation**

The conducting Earth and conducting ionosphere form an electromagnetic waveguide through which very low frequency (VLF; 3-30 kHz) radiation efficiently propagates with little attenuation. It is this mechanism which makes the long-range detection of VLF energy from lightning strokes, and, hence, the WWLLN, possible. Because VLF radiation can travel for thousands of kilometers in the Earth-ionosphere waveguide, it is possible to receive signals from all over the world at 5 or more WWLLN receiver stations with only about 30 stations world wide.

The Earth-ionosphere waveguide also provides for one of the most useful methods for probing the lower ionosphere. The lower ionosphere (~65-85 km altitude) is difficult to probe by using many traditional techniques; the altitude is too high for balloons (~30 km) and too low for low-earth orbiting satellites (~400-800 km). The electron density in the lower ionosphere is too low to reflect signals from ionosondes and incoherent scatter radars. Rocket flights are useful for in situ measurements, but are very short duration and only make measurements locally. Remote sensing of the lower ionosphere by measuring phase and amplitude of VLF signals that propagate in the Earth-ionosphere waveguide provides longer-term monitoring of the ionosphere than rocket flights allow. Typically the signals available for study are narrowband transmitters run by governments for submarine communication [Helliwell et al., 1973; McRae and Thomson, 2000]. Recently, some researchers have begun to use lightning radiation as a probe of the ionosphere as well [Cummer et al., 1998; Cheng and Cummer, 2005].

In order to better understand the data, ionospheric wave propagation theory was developed in conjunction with these experimental measurements [Budden, 1961; Wait, 1970]. These theories were based on electromagnetic waveguide theory, using the conducting earth and conducting ionosphere as the "walls" of the waveguide. They originally assume a flat earth with a sharply bounded ionosphere, and then add complexity to take into account the curvature of the Earth and the gradual change in ionospheric conductivity. More recently, computer programs have been developed to model the propagation of VLF waves using this waveguide mode theory of radio wave propagation. The most widely used of these programs is the Long-Wave Propagation Capability (LWPC) described in Ferguson and Snyder [1987]. A modified version of this code will be used for some analyses in this dissertation.

1.7 **Dissertation Outline**

This introductory chapter has provided a brief introduction to the scientific questions and previous studies that motivate this dissertation. The focus of this dissertation is to study the coupling between lightning energy and the lower ionosphere.

WWLLN data are used to monitor spatial/temporal variability of strong coupling regions and an electromagnetic model is presented to describe the expected accumulated energy deposition from multiple lightning strokes. This dissertation also presents the research required to validate the WWLLN as well as the application of WWLLN data to provide information on high-density regions of nighttime lightning as well as into elves and terrestrial gamma-ray flashes. The following is a detailed outline of the chapter structure of this dissertation:

Chapter 2 provides a complete introduction to the World-Wide Lightning Location Network. Detection efficiency and location accuracy validation of the WWLLN is presented Chapter 3. Findings from Chapter 3 are used in Chapter 4 to provide time-dependent maps of regions of strong nighttime lightning. Chapter 5 presents an investigation into whether the WWLLN can detect narrow-bipolar pulses as is suggested by initial research. Chapter 6 will focus on two case studies that use WWLLN to provide information on elves and terrestrial gamma-ray flashes. Chapter 7 builds on the existing capabilities of WWLLN by developing a method to determine lightning stroke radiated energy in the VLF band. Chapter 8 investigates the lightning EMP/ionosphere interaction by modifying a model to propagate the lightning EMP to the lower ionospheric plasma. Finally, a summary and conclusion are presented in Chapter 9.

Chapter 2: World-Wide Lightning Location Network

2.1 **Network Introduction**

The WWLLN is the only lightning location network with the capability to continuously monitor the location of lightning strokes around the entire world. The WWLLN detects lightning strokes, regardless of lightning type, that have peak currents with magnitudes above ~40 kA with a constant detection efficiency [Jacobson et al., 2006]. The WWLLN originated from the "toga" network [Dowden et al., 2002].

The WWLLN has been providing continuous accurate locations and times for lightning strokes globally since August 2003 [Lay et al., 2004; Rodger et al., 2005a; Jacobson et al., 2006]. Figure 2.1 shows the real-time global lightning detection capabilities of the WWLLN.

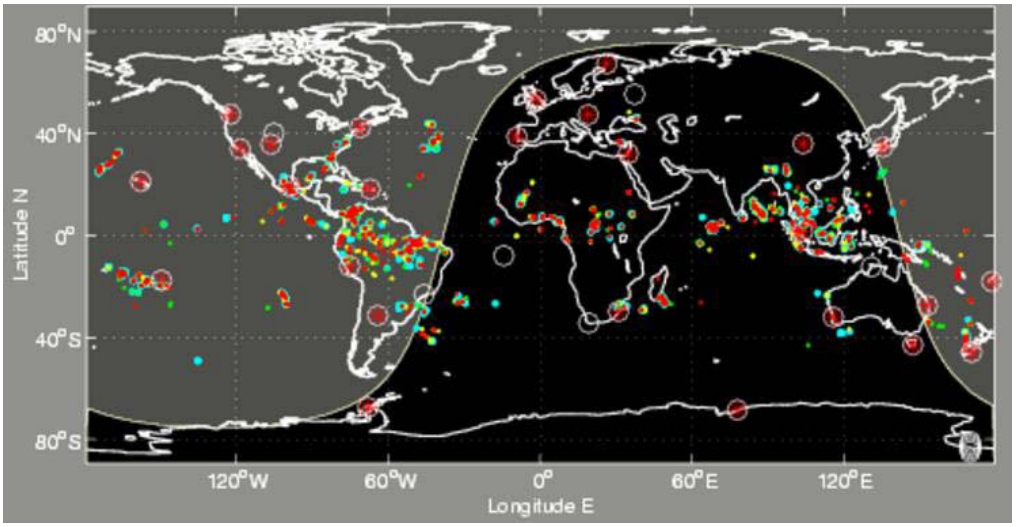

Figure 2.1: WWLLN map of lightning locations 40 minutes previously to 20:40:00 UT on 28 April, 2008. This plot is updated every ten minutes at wwlln.net. Small colored dots represent 40 minutes of lightning strokes, with the blue dots showing the most recent lightning (occurring within the last ten minutes), then green, yellow and, finally, the red dots showing lightning occurring 40 minutes ago. White circles with red stars represent active WWLLN stations. Empty white circles represent a station that is off the air. The terminator is shown separating the daytime (gray background) from nighttime (black background).

This map shows 40 minutes of lightning locations starting at 20:00:00 UT on 28 April, 2008. This plot can be found on the WWLLN webpage http://wwlln.net and is

updated every ten minutes. It shows 40 minutes of global lightning locations, with the blue dots showing the most recent lightning (occurring within the last ten minutes), then green, yellow and, finally, the red dots show lightning occurring 40 minutes ago. The red stars with the white circles around them show the active WWLLN stations around the world. The white line separating the black area from the gray area is the day-night terminator. Jacobson et al. [2006] shows that the WWLLN has a flat detection efficiency of ~4% for all types of strokes with peak current magnitude above 40 kA. Rodger et al., [2005a] has found that the detection efficiency in Australia and New Zealand is dramatically higher, at ~26% of CG strokes. We will take detection efficiency into account in our studies using WWLLN flash rates by normalizing the WWLLN flash rates based on these detection efficiencies.

2.2 **WWLLN Hardware**

Dowden et al. [2002] describe the instrumentation at each site and present data from the initial six receiving sites spanning from New Zealand to Japan. The VLF receiver stations each consist of a short (1.5m) whip antenna, a GPS receiver, a VLF receiver, and an Internet connected processing computer. A cartoon schematic of a WWLLN station is shown in Figure 2.2. The components inside the dotted line are housed inside a building, while the antennas and preamp are mounted outside. Schematics of the preamplifier and Service Unit (containing timing and VLF processing electronics) are found in Appendix A.

The VLF antennas are typically mounted on ferro-concrete buildings. These buildings shield the antenna from local man-made noise because they are adequate conductors at VLF and thus remain at ground potential. In addition, the vertical electric field from strong CG lightning dominates over power-line noise. For these reasons, WWLLN receivers have relative freedom from the restriction of noise-free receiver locations required for other long-range lightning location techniques [e.g., Fullekrug and Constable, 2000]. The antennas measure radio wave pulses (sferics) in the VLF

band (1-24 kHz) radiated by lightning discharges. Lightning-generated waves in this frequency range can propagate many thousands of kilometers in the Earth-ionosphere waveguide because of low attenuation and high power spectral density [Crombie, 1964].

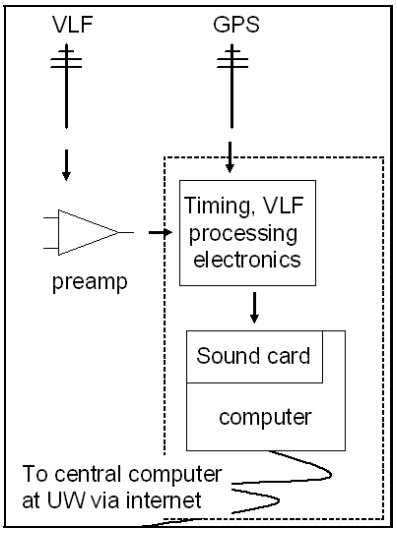

Figure 2.2: Cartoon schematic of a WWLLN VLF receiving station. Elements inside the dotted line are housed inside a building.

The preamp provides a gain of 10 to the electric field signal detected by the antenna. This amplified signal is then routed via a long cable inside a building to the Service Unit, which serves to isolate the signal via an audio transformer and then sends the signal to the computer sound card. The Service Unit also provides power to the preamplifier.

The GPS antenna provides one pulse per second. This pulse is input to the computer sound card and used to adjust the time-stamp on each VLF waveform. The GPS antenna also provides an NMEA signal giving the exact location of the station, that is input to the computer via a serial port connection.

The requirements for the station computer are minimal: It must be able to run RedHat Linux, and must have a sound card and serial port. A sufficient amount of RAM is 248 or 512 MB and 20-40 GB is plenty of hard-disk space. The computer also must be continuously connected to the internet.

2.3 **WWLLN Software**

The software for each WWLLN station was developed by Dr. James Brundell and the TOGA (time of group arrival) methodology was developed by Dowden and his team [Dowden et al., 2002]. This software functions as follows: The VLF electric field is sampled at ~48kHz. When the difference between two consecutive samples exceeds a given threshold level, a 64-sample waveform is saved to short-term memory to be analyzed. This waveform consists of 16 pre-trigger data points and 48 post-trigger points. Figure 2.3 shows an example of such a waveform detected at a WWLLN VLF station.

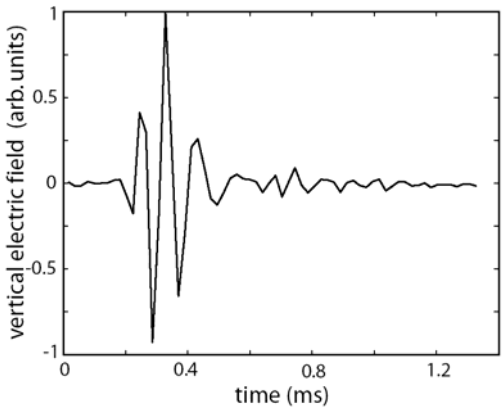

Figure 2.3: Example 64-sample waveform of a lightning sferic. Time is in milliseconds on the x-axis and uncalibrated vertical electric field is on the y-axis.

When a sferic waveform is captured, the software determines the time of group arrival (TOGA) of the group energy for that sferic. The reason the TOGA method was developed was because the sferic waveform becomes dispersed during its propagation of often thousands of kilometers in the Earth-ionosphere waveguide. Thus the trigger time does not necessarily indicate the time of arrival of the group energy. If the wave is extremely dispersed, the arrival of the group energy will occur later than the trigger time.

The TOGA is calculated as follows: The group velocity in a waveguide is given by $v_g(\omega) = d\omega/dk$, where $k(\omega)$ is the frequency dependent wave vector. The electric field

of the wave can be expressed as a sum of Fourier components of the frequency, ω: E(r, t, ω) = $\Sigma A(\omega)\cos(\varphi(\omega))$, where $\varphi(\omega) = \omega t - k(\omega)r + \varphi_0$. The slope of the phase $\varphi(\omega)$ at a given time t and range r, is then given by $\frac{d\varphi}{d\omega} = t - r\frac{dk}{d\omega} = t - \frac{r}{v_g(\omega)}$. This equation shows that $d\varphi/d\omega$ equals zero when t equals the group travel time, $t_g = \frac{r}{v_g(\omega)}$. An instantaneous time for which $d\varphi/d\omega$ at a given value of ω is not sensible for a broadband source such as a lightning sferic. Instead, an average $d\varphi/d\omega$ is determined over the frequency band of 6-22 kHz. This band is chosen because lightning energy is maximum over this band, and our WWLLN stations are sensitive to this band. The TOGA is defined as the instant when the regression line of $d\varphi/d\omega$ has zero slope when averaged over the frequency band of 6 to 22 kHz [Dowden et al., 2002]. The software on each WWLLN VLF station computer determines the TOGA for each sferic by calculating the time when the regression line of $d\varphi/d\omega$ in this frequency band equals zero and then reports that time to the central processing computer to be used in lightning location.

The software also calculates an uncalibrated integrated energy flux density, Y, for each station, which will be used later in this dissertation to determine a calibrated energy radiated per lightning stroke. This energy flux density is the integrated energy in the uncalibrated electric field at the antenna and is determined as follows:

$$Y = \sum_{samples} \frac{(E')^2}{c\mu_0}\Delta t \qquad (2.1)$$

where E' is the uncalibrated electric field as shown on the y-axis of Figure 2.3, c is the speed of light, $\mu_0 = 4\pi*10^{-7}$ W/(A*m), and Δt=1/(sampling frequency). Chapter 7 of this dissertation describes how the uncalibrated integrated energy can be used to help determine the magnitude of the lightning stroke in terms of total radiated energy.

The integrated energy in the electric field waveform, the TOGA, and the station identification number are sent to the central processing station. If five or more stations

detect an event, the location and time of the discharge is determined by using the downhill simplex method to minimize the difference in location and time given by the five or more stations. While detection of an event by 4 stations would be enough to produce a location estimate, the 5th station allows error analysis. The minimization routine produces a location and timing "residual" that indicates an accuracy estimate of the measurement. The global data are then posted to the internet every 10 minutes (see http://wwlln.net), and sent in real-time to research groups and commercial customers.

Chapter 3: Global Detection Efficiency and Location Accuracy

3.1 **Overview**

In order for WWLLN to provide useful global coverage, we must understand its global detection efficiency. During the development of the network, a number of studies have been completed to achieve this goal. The studies presented here include (1) a case-study comparison of WWLLN detection efficiency and location accuracy done in Brazil in 2003 (Section 3.1), and (2) a comparison of WWLLN lightning locations to optical lightning detector data on the FORTE satellite in order to determine a relative global detection efficiency for the network (Section 3.2). Section 3.3 will investigate the detection range of WWLLN stations.

These studies have been conducted in conjunction with additional detection efficiency studies done by members of the WWLLN team: Rodger et al. [2005a] completed a comparison of WWLLN data in Australia to the local Australian lightning location network, Kattron, and found a detection efficiency of ~26% of CG strokes in Australia and ~10% of IC strokes, with a location error of 4.2 ± 2.7 km. By comparison to the Los Alamos Sferic Array (LASA) in the southeastern U.S., Jacobson et al. [2006] found that WWLLN detects ~4% of all strokes, CG and IC, with peak current greater than ~30 kA, and detects with a spatial accuracy of ~15 km. Of the coincident events between WWLLN and LASA, 26% were labeled as IC lightning by LASA. Similarly, Rodger et al. [2006a] found the result of a flat detection efficiency for strokes with peak currents larger than ~40 kA by comparison to the New Zealand Lightning Detection Network (NZLDN).

3.2 **Brazil Integrated Network/WWLLN Comparison**

The March 2003 comparison between WWLLN and the Brazilian Integrated Network (BIN) was motivated by the desire to study the “worst-case scenario” for the

WWLLN system, as it covered a region of the world where the nearest WWLLN receiver was >7000 km away during a time when WWLLN had not yet implemented the TOGA algorithm. Instead, the trigger time at the station was used as the time of arrival of the sferic. During data-collection period for this study (March 2003), the WWLLN was composed of just 11 active VLF receivers. Table 3-A shows the locations of these receivers.

Table 3-A: Station locations for stations active during Brazil comparison study

Station	Latitude (deg)	Longitude E (deg)
Dunedin, New Zealand	-45.8639	170.514
Darwin, Australia	-12.3718	130.868
Perth, Australia	-32.0663	115.836
Singapore	1.2971	103.779
Brisbane, Australia	-27.5534	153.052
Osaka, Japan	34.8232	135.523
Tainan, China	22.9969	120.219
Budapest, Hungary	47.4748	19.062
Seattle, USA	47.654	-122.309
Cambridge, USA	42.3604	-71.0894
Durban, South Africa	-29.8711	30.9764

3.2.1 *Method*

We compare WWLLN lightning events with residuals (error estimates) less than 20 μs that occurred on 6, 7, 14, 20, and 21 March 2003 in the range of 40º to 55º W, 15º to 25º S to events in the same range measured by a land-based local Brazil lightning detection network, the Brazilian Integrated Network (BIN) [Pinto and Pinto Jr., 2003; Pinto Jr. et al., 2003]. Figure 3.1 shows the region of interest in Brazil. We study these data because the BIN data had already been procured by our group for use in the sprite balloon campaign in 2002-2003 in Brazil [Holzworth et al., 2005b].

BIN consists of 21 sensors in the region of interest, with an overall stated detection efficiency of 80% of all cloud-to-ground lightning strokes. However, the efficiency is dependent on return stroke peak current. Detection efficiency of events with peak current greater than 50 kA is 90% with a location accuracy of less than 1 km. For events with peak current less than 10 kA, detection efficiency could be as low as 30% with

approximately 5 km location accuracy. The return stroke peak current measurement also includes uncertainty due to assumed lightning return stroke speeds, as expected for detectors of this type [e.g., MacGorman and Rust, 1998]. BIN cites an uncertainty of 20-30% for strokes with peak current greater than 10 kA and up to 100% uncertainty for strokes with less than 10 kA peak current [Pinto Jr., personal communication, 2003].

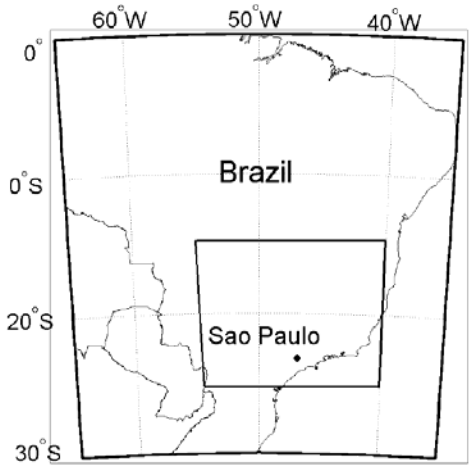

Figure 3.1: Region of Brazil comparison between lightning location networks used in this study. As there were no WWLLN receivers in South America, this region of Brazil is a low-coverage region of the WWLLN.

3.2.2 *Results*

In the five-day time period, 671 WWLLN events and 63,893 BIN events were reported in the region of interest. Taking into account the 80% accuracy of BIN [Pinto Jr. et al., 2003], a rough estimate of the percentage of all CG lightning events measured by WWLLN in this region is ~0.8%. To measure the accuracy of WWLLN, we compare the data sets from the two networks to find "shared" events. A lightning stroke is assumed to be shared if each network measures an event within 3 ms and 50 km of the other. According to these criteria, 289 of the 671 WWLLN events are common to the BIN stroke data.

The shared events have an average return stroke peak current of 86 kA, as measured by BIN. In contrast, the average peak current of the entire BIN dataset is 33.3 kA, suggesting that the WWLLN network only detects large discharges that exceed an

approximate "threshold" in return stroke peak current. The histogram in Figure 3.2 represents this threshold by comparing the BIN peak current distribution of the entire BIN data set to only the BIN events which were also observed by WWLLN. Overall, a greater fraction of the strokes have negative polarity, as expected. However, for discharges with an absolute value of peak current less than 50 kA the figure shows that there is a larger proportion of such low-current lightning in the overall BIN dataset (black) than in the subset made up of only shared events (white). For events with peak current greater than 50 kA, the relative pattern is reversed. This pattern illustrates that WWLLN detection is biased towards lightning strokes with large peak currents.

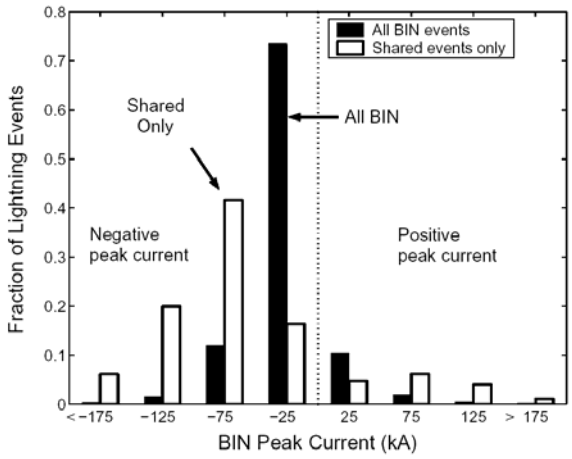

Figure 3.2: Histogram of return stroke peak currents measured by the BIN, shown in 50 kA bins centered on the single peak current value noted beneath them. The two outermost bins contain data for all strokes with peak current greater or less than 175 kA. Distributions are shown for shared WWLLN-BIN events (white) and all measured BIN events (black).

Next, we estimate the spatial and temporal accuracy of WWLLN by analyzing the shared events. Time differences between the shared strokes are on average 0.06 ± 0.2 ms. To calculate location offsets for WWLLN strokes relative to their shared BIN events, we plot each shared BIN event at (0,0) and determine the east-west and the north-south deviation of the WWLLN positions (Figure 3.3).

WWLLN events have a mean deviation of 3.2 km north (dashed-dotted line), 7.3 km east (dotted line) from BIN events. The plotted ellipse of one standard deviation encompasses (0,0), indicating no statistically significant difference in the location of the

shared events. The elongation of the data spread is possibly a systematic error due to differences between east-to-west and west-to-east VLF propagation in the Earth-ionosphere waveguide [Wait, 1970]. The location errors might be improved by using an enhanced location finding algorithm that incorporates ionospheric propagation. In analyzing the data for random error, we find that the absolute location error is 20.25 ± 13.5 km for WWLLN network observations in this part of Brazil.

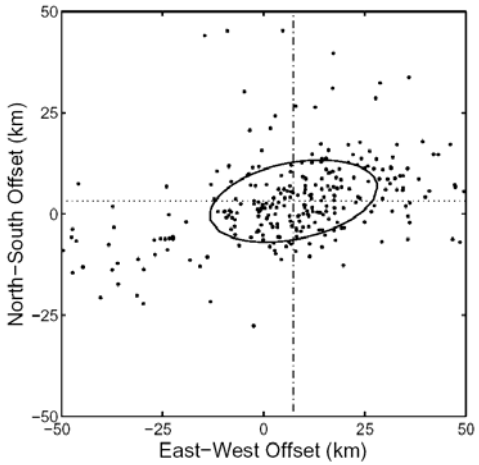

Figure 3.3: Location offsets of shared WWLLN-BIN events relative to the BIN-determined discharge position. Each shared BIN event is taken to be at (0,0) and the corresponding WWLLN event is plotted relative to (0,0). Mean location offset is 3.2 km north (dashe-dotted), 7.3 km east (dotted). One standard deviation (ellipse) encompasses (0,0).

3.2.3 *Summary of Brazil Study*

This analysis has shown that WWLLN provides lightning location of about 0.8% of lightning events in Brazil with an accuracy of 20.25 ± 13.5 km and 0.06 ± 0.2 ms. The WWLLN detection efficiency, while low compared to the BIN, suffices to mark storm occurrence due to the large number of total lightning strokes that occur in storm systems. In addition, this study was the first study of WWLLN to show that WWLLN detects high-peak-current lightning.

The greatest advantage of WWLLN is global lightning coverage in real time at low cost. By comparison with a regional network on the outskirts of the current WWLLN coverage zone, our analysis indicates that the WWLLN-reported lightning events have

spatial resolution on the order of magnitude of an isolated thunderstorm and excellent temporal accuracy. For many applications, the benefits of a global overview in real time may outweigh the fact that a very low percentage of the total lightning activity is reported. The WWLLN is shown to be an important scientific and operational tool for lightning and severe-storm researchers to characterize remote storms, and should prove to be a highly useful tool for the atmospheric-sciences community.

3.2.4 *Advances in WWLLN since this study*

Two improvements have been made since this study to increase the total percentage of lightning events measured by the WWLLN. The first is the installation of additional stations in the low coverage region. One may refer to Figure 2.1 for a complete station coverage map as of April 2008. The second is the implementation of the TOGA timing algorithms, described in Section 2.3, that takes the dispersion of the sferic into account by measuring time of group arrival (TOGA) of the sferic. This new algorithm accounts for the long propagation distance of VLF waves from Brazil and thus increases accuracy of the timestamp at each VLF receiving station that is used in the location of each lightning event. Since January 2008, WWLLN has been running a new lightning location algorithm that recycles packets (TOGAs from VLF stations) if they were not used in locating a lightning stroke, meaning that if a particular set of packets did not produce a valid location, only the first packet is thrown out, and the others are reused to try to find a valid location.

3.3 **FORTE/WWLLN Comparison**

3.3.1 *Overview*

Although comparisons of the WWLLN to ground-based networks have determined its detection efficiency over small geographic regions as discussed in sections 3.1 and 3.2, and some attempts have been made to model the global detection efficiency [Rodger et al., 2005a, 2006], the detection efficiency of WWLLN has not yet been

determined on a global scale. Given that WWLLN VLF receiver stations are not spread uniformly around the world, and that topographical features vary over the earth, the detection efficiency around the world could vary as well. We also study the relative detection efficiency over land and over ocean for WWLLN. One might expect a difference in detection efficiency given that lightning-generated VLF radio waves propagate with less attenuation over sea water than over land [Wait, 1970]. Since the WWLLN requires that the signal from a lightning sferic be detected by five or more WWLLN VLF stations, a larger attenuation over land could mean that a lightning stroke over land may be less likely to trigger the required five stations.

In this section we describe a systematic check of the long-range VLF relative detection efficiency over land and over ocean, and over diverse geographical regions, using the FORTE satellite photodiode detector (PDD) optical measurements of lightning as a reference.

3.3.2 *FORTE photodiode detector*

We use optical lightning data from the photodiode detector (PDD) on the Fast On-Orbit Recording of Transient Events (FORTE) satellite [Suszcynsky et al., 2000b, 2001; Kirkland et al., 2001]. The PDD is a non-imaging silicon photodiode collecting light from within a circular field of view of diameter 1200 km at ground level. Because the PDD is non-imaging, any event it detects can be located only to within this 1200-km footprint. The PDD is triggered by a rising optical signal intensity. Once the intensity exceeds the threshold level and a trigger occurs, a 128-sample register is stored in memory, including 32 samples preceding and 96 samples following the trigger. The sample interval is 15 μs, so the record duration is about 1.9 ms. The FORTE satellite is in a 70º circular orbit at 800-km altitude. Thus the PDD "spotlight" sweeps out the entire region where lightning is found on Earth.

Because the PDD instrument is satellite-based, it observes lightning from above, meaning that it can only detect light that manages to escape from the cloud tops. Previous studies have shown that the majority of PDD-detected events are in-cloud (IC)

lightning [Susczynsky et al., 1999], although the PDD is also able to detect scattered light from the in-cloud portion of a cloud-to-ground (CG) lightning stroke [Susczynsky et al., 2000b].

Because of high daytime background light levels, the trigger level for the PDD instrument is set higher during daytime than nighttime to avoid contamination from false triggers. This trigger level difference has the effect of biasing the daytime PDD data to high peak current strokes.

It has been shown that PDD has a detection efficiency lower than, but constant relative to, LIS detection efficiency over all areas of the world [Light et al., 2003]. Thus, we are confident that PDD data serve as an adequate proxy for LIS or OTD data, with the proviso that the PDD locates lightning only to within the 1200-km-diameter field of view, as opposed to within an individualized pixel of an imager. An advantage of PDD for this study is that we can examine optical waveforms relative to the VLF lightning trigger. For this study we assume equal PDD detection efficiencies for land and ocean.

3.3.3 *WWLLN/PDD Comparison Methodology*

In this study we search for coincident lightning events between WWLLN-detected lightning sferics and PDD-detected optical waveforms measured between 1 August 2003 and 31 December 2005. To find coincident events, we first exclude any WWLLN events that occur outside the PDD 1200-km field of view. From this reduced WWLLN data set, we compare the WWLLN sferic time to the optical trigger time. All PDD events that are within 200 ms of a WWLLN-located sferic are corrected in time for the optical signal delay to the satellite, by assuming the WWLLN sferic location as truth. A histogram of the corrected time differences of WWLLN-measured sferic time minus optical trigger time is shown in Figure 3.4. Figure 3.4 peaks at -0.25 ms, indicating that the sferic time usually precedes the optical trigger by about 0.25 ms. From this histogram, we choose a classification for coincident events as pairs having a corrected time difference for sferic-optical trigger time between -0.80 ms to 0.30 ms. We choose

these limits so that the number of random coincidences occupying the coincidence region is less than 2% of the total: The random coincidence rate of ~20 counts per bin can be seen on the far edges of Figure 3.4 (absolute value of time differences > 3 ms). Using the random coincidence rate of 20 counts per bin and the total number of coincidences in the region between -0.80 ms to 0.30 ms, we find the number of random coincidences does not exceed 2% of the total. Also visible in Figure 3.4 is a smaller secondary bump at a time difference of ~2 ms. This bump is an artifact of the ~ 2 ms dead time after triggering of the PDD instrument.

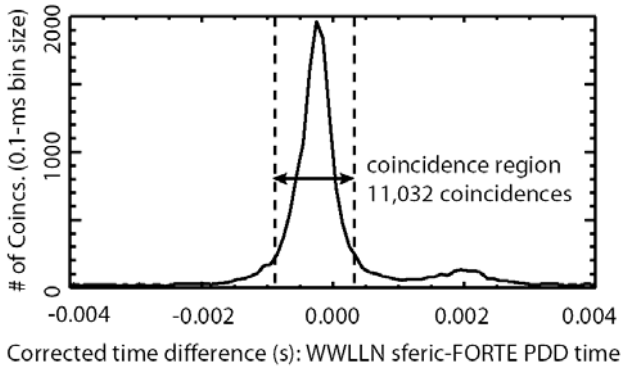

Figure 3.4: Time-difference histogram of WWLLN-sferic time minus FORTE PDD trigger time, corrected for optical signal delay to satellite. Bin size is 0.0001 second. The peak occurs at ~ -250 μs, indicating that the PDD optical is triggered about 250 μs after WWLLN detects the sferic. The two vertical dashed lines indicate the timing cutoffs for coincident events (-0.80 to 0.30-ms timing difference). 11,032 events fall within the cutoff times.

3.3.4 *Results*

In the time period of the comparison, the PDD instrument on FORTE measured 2,520,211 optical events, while WWLLN located 26,430 lightning strokes within the PDD footprint. Of the total number of WWLLN and PDD events, 11,032 participate in a coincident pair. In comparison to earlier WWLLN coincidence studies, this number of pairs is 55 times larger than the comparison by Lay et al. [2004] and about 2 times larger than the analysis by Rodger et al. [2006].

To examine regional differences in the WWLLN detection efficiency, we separate these events into the six global regions shown in Figure 3.5. The motivation of the division locations was to try to avoid cutting major continental landmasses apart.

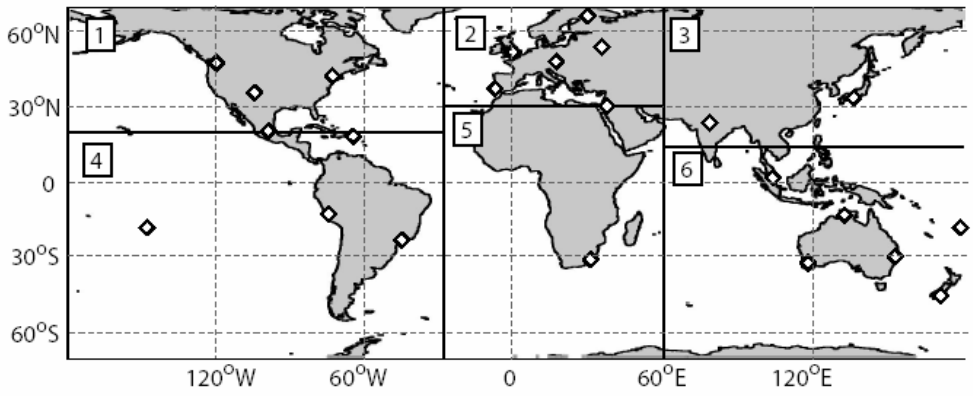

Figure 3.5: WWLLN station locations (diamonds) in January 2005 and the six broad regions used in this study. The thickness of the coastlines shows the size of the coastal region used in the land/ocean study.

Table 3-B shows the results of this categorization. The data are divided into six columns corresponding to the six global regions of interest. The first and second rows show the number of PDD events and WWLLN events, respectively, in each regional box. The third row shows the number of coincident events in each region. The fourth row shows relative detection efficiencies (the total number of WWLLN events detected divided by the total number of PDD events detected) and the fifth row shows the fraction of WWLLN events in each region that were coincident with a PDD event.

One must note that the values shown in Table 3-B do not represent absolute detection efficiencies, since, in general, the PDD instrument detects mainly IC lightning while the WWLLN detects mainly CG lightning. In a comparison of PDD to NLDN, which estimates a detection efficiency of ~90% for high peak current strokes, Suszcynsky et al. [1999] found that the PDD only detected 5.5% of NLDN-detected negative CG lightning and 8.3% of positive CG lightning. However, even without an absolute detection efficiency calibration, this analysis can provide an understanding of the relative detection efficiency of the WWLLN on a global scale.

The region with the highest detection efficiency is Australasia (region 6), and the lowest detection efficiency is in Europe (region 2), followed by Africa (region 5). The fraction of WWLLN strokes that are coincident with PDD events (row 5 in Table 3-B) does not correspond directly to the detection efficiency. The lowest fraction is once again in region 2 (Europe), but the highest fraction is now in region 5 (Africa). This difference may mean that the strokes that are detected by PDD in Africa are more likely to be the type of stroke that also is detected by the WWLLN (high-peak current CG strokes). We have now also been able to analyze data from 2006 for these 6 regions. In 2006, WWLLN stations were added in Honolulu, Hawaii; Rothera, Antarctica; Kingston, Australia; Cordoba, Argentina; Ascension Island; and Lanzhou, China. These additions have increased the detection efficiency as compared to PDD, by 20% overall, and regionally by ~100% in Region 1, ~50% in Region 4, and ~10% in Region 5.

Table 3-B: Results of WWLLN/PDD regional comparison 2005

Region #	**1**	**2**	**3**	**4**	**5**	**6**
PDD total	232,380	88,474	187,935	480,907	802,771	727,744
WWLLN total	2,204	428	1,552	4,198	4,821	13,227
# coincs	905	161	655	1,692	2,131	5,488
$\frac{\text{WWLLN total}}{\text{PDD total}}$	0.009	0.005	0.008	0.009	0.006	0.018
$\frac{\#\text{coincs}}{\text{WWLLN total}}$	0.411	0.376	0.422	0.403	0.442	0.415

To examine land/ocean differences in the WWLLN detection efficiency, we separate these events into land and ocean subsets in two ways. In the absence of a coincident WWLLN-located lightning stroke, PDD events can be located only to within the 1200-km-diameter PDD footprint, meaning that an optical event detected with the sub-satellite point located within 600 km of the coastline could have occurred over either the land or ocean.

Therefore, the first classification (shown in Table 3-C) labels events as "over land" (1st column, Table 3-C) only if either the WWLLN location, or the FORTE sub-satellite point, is over land *and* more than 600 km from the coastline, and labels events as "over ocean" (2nd column, Table 3-C) only if either the WWLLN location, or the FORTE sub-satellite point, are over ocean *and* more than 600 km from the coastline. The lightning "within 600 km of coast" (3rd column, Table 3-C) is all the remainder and corresponds to lightning that occurred over any surface within 600 km of coast. Most of the lightning-prone areas of Australasia and central America are swept into the coastal category in Table 3-C. This classification scheme provides us a basis to compare land/ocean differences for all PDD and WWLLN events, as opposed to only coincident events.

Table 3-C: Results of WWLLN/PDD land/ocean comparison using 600-km coastal areas

	over land & >600km from coast	over ocean & >600km from coast	within 600km of coast	**total**
PDD total	401,902	255,107	1,863,202	**2,520,211**
wwlln total	2,892	2,064	21,474	**26,430**
wwlln/PDD	**0.007**	**0.008**	0.012	**0.010**

In addition to showing lightning counts in the three categories described above, Table 3-C also includes a "total" column to provide a quick reference to the total number of PDD and WWLLN events that were detected within the PDD "spotlight" during the time period of the study. We find the ratio of total number of WWLLN events to total number of PDD events over land and ocean in the last row of Table 3-C. WWLLN detects 0.7% of the number of events PDD detects over land and 0.8% over ocean, indicating a difference of less than 13% in WWLLN detection efficiency over land and over ocean. The ratio of total coastal WWLLN to total coastal PDD events is slightly higher, at 1.2%. We believe this increased ratio can be explained thus: the number of events within 600 km of the coastline is dominated by lightning in Australasia, as most of the land in that region is not more than 600 km from a coastline,

and Australasia is the region of highest WWLLN detection efficiency as seen in Table 3-B.

Next, we focus on coincident events measured by PDD and WWLLN. For this second grouping of data, we take advantage of the more accurate WWLLN location in analyzing events by first assigning each PDD event coincident with a WWLLN event with the location of that WWLLN event. Because WWLLN-measured strokes have a location accuracy of 15-20 km, we next sort coincident events into land and ocean subsets with only a ~50-km-semi-width "coastal" region. The land/ocean/coastal separation map was created using high-resolution continental borders, including major islands, on a 1440×900 pixel grid, covering –70 to 70 degrees latitude. The pixels covering land areas were given a value of 1 and those covering ocean were given a value of zero. A smoothing procedure over 4 pixels gives any land or ocean within 2 pixels of the coastline a value in between 0 and 1, and it is these pixels that are classified as coastal. At the equator, this gives a coastal area of ~55 km from the coast. Therefore, islands smaller than ~110 km will not be included in the 'land' category. The continental border thickness in Figure 3.5 indicates the width of the coastal region in this study. WWLLN events located in the coastal region are not used in the land/ocean local time study (Chapter 4), but are included in Table 3-D as coastal events. The 50-km-semi-width swath of rejected data additionally allows us to reduce the occurrence of erroneously classifying an oceanic lightning event as over land (or vice versa) due to the 15-20 km location accuracy of WWLLN [Lay et al., 2004; Rodger et al., 2004; Jacobson et al., 2006].

Table 3-D: Results of WWLLN/PDD land/ocean coincidence comparison

	over land	over ocean	coastal	**total**
# coincs	4,307	4,122	2,603	**11,032**
WWLLN total	11,074	9,290	6,066	**26,430**
$\frac{\#\text{ coincs}}{\text{WWLLN total}}$	**0.389**	**0.444**	0.429	**0.417**

Table 3-D shows the results of this stratification. The 1st row shows the number of coincident events, separated into "over land", "over ocean", and "coastal" events by using the criteria described in the previous paragraph. In the second row of Table 3-D, all WWLLN data are also separated into the three categories using the 50-km-semi-width "coastal" region. The bottom row shows the total number of coincident events divided by the total number of WWLLN events. These results show that 38.9% of WWLLN events over land participate in a coincidence with a PDD event, while 44.4% of oceanic WWLLN events participate in a coincidence. The small percentage difference in land/ocean coincidence detection efficiency indicates that it is unlikely that the WWLLN will completely miss a storm with lightning of similar magnitude over ocean relative to over land. With these statistics, we can begin to use the WWLLN to study relative differences in the effects of strong lightning over land versus over ocean.

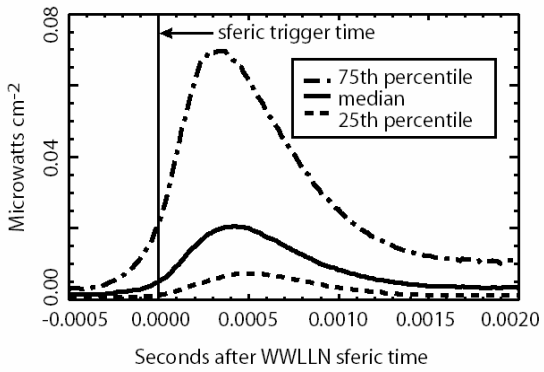

Figure 3.6: A superposed epoch of PDD waveforms with WWLLN coincidences. The median (solid line), 75th percentile (dashed-dotted line), and 25th percentile (dotted line) in amplitude of all PDD waveforms which participated in a 1.1-ms coincidence with WWLLN are separately plotted. These statistics are computed independently for each time bin. The waveforms are individually shifted in time to place the WWLLN-calculated sferic time at 0.00 seconds.

A superposed-epoch accumulation of the optical waveform and the sferic stroke time has been performed to further validate the comparison. Figure 3.6 shows the median, 75th percentile, and 25th percentile in amplitude of all PDD waveforms which participated in a coincidence with WWLLN. The amplitudes are considered separately in each time bin. The waveforms are shifted in time to position the WWLLN-calculated sferic time at 0.00 seconds. The 0.3- to 0.4-ms delay in the optical peak is slightly

longer than found by Susczynsky et al. [2000b] in a VHF/optical comparison, in which a 243-μs average delay of the optical peak was attributed to a 105-μs average delay between VHF and optical emission plus an average 138-μs broadening due to scattering delay of light in its travel through the cloud. Figure 3.6 shows general agreement with the timing data and waveform shapes of previous studies, giving cause to trust the coincidences found by this comparison.

With confidence in the WWLLN/PDD-detected coincidences and in the relative detection efficiency of WWLLN over land and ocean, we can use the entire, not just PDD-coincident, WWLLN data set to look at land/ocean effects in high peak current lightning occurrence. In Chapter 4 of this dissertation, we will look at local time differences in lightning over land and over ocean and demonstrate the suitability of WWLLN as a tool to study these variations on shorter time scales than can be seen from satellite averages.

3.3.5 *Conclusion*

The comparison of the World-Wide Lightning Location Network with satellite optical data has provided global verification of the capabilities of the WWLLN in detecting lightning globally and over land versus ocean with a similar relative detection efficiency. It has also provided relative detection efficiencies for six large geographical regions over 2 years that will be used in this dissertation to determine global lightning count rates.

3.4 **Detection range of WWLLN stations**

Figure 3.7 indicates that WWLLN stations can detect lightning at very large distances, as expected from fundamental VLF propagation [Crombie, 1964]. By using WWLLN observational data we can characterize the typical WWLLN station observing range, i.e., at what distance can a particular station detect a lightning stroke. We use a sample of WWLLN data from 1–30 April 2005 to determine the detection range of each

station. To calculate the detection range, we find which events of the entire WWLLN data set each station participated in detecting.

For this example, we will discuss and calculate the detection range of the Darwin WWLLN station, hosted by Charles Darwin University. We calculate the distance between the Darwin station location and each lightning event that was detected at the Darwin WWLLN station. We then determine the number of events Darwin detected versus distance from the station, in 200-km bins, as well as the number of events the WWLLN as a whole detected versus distance from Darwin. Because of the spherical geometry of the Earth, the bins increase in area until 10 megameters (Mm) and then decrease in area for the larger distances. Thus, the bins that contain data from 10 Mm have better statistics than those at either 1 Mm or 20 Mm. Figure 3.7 shows a histogram of the ratio of the events the Darwin WWLLN station "saw" over the total number of events the WWLLN network detected versus the distance of the lightning stroke from the Darwin station. A ratio of one would indicate that the Darwin station participated in the detection of all the lightning that the WWLLN reported in that 200-km-width bin. The black dots show the ratio for events that occurred ±2 h around local noon, and the gray plusses show the ratio for events that occurred ±2 h around local midnight. While lightning located very far from the Darwin WWLLN station may have propagated under a mixture of both day and night ionospheres when considering the case of local noon at Darwin, this situation will be dominated by the daytime ionospheric propagation conditions around the WWLLN station.

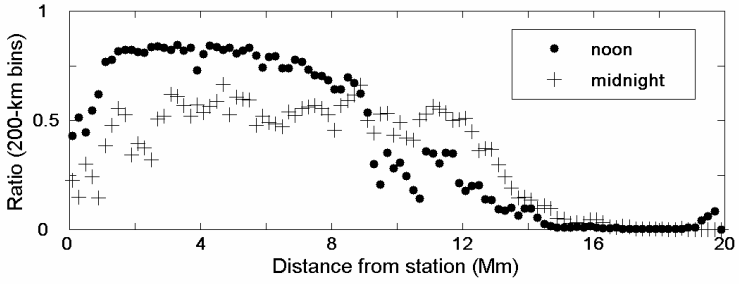

Figure 3.7: Ratio of the number of events detected by the Darwin station to the number of events detected at the same range from Darwin by the network as a whole. The black dots show this ratio for ±2 h around local noon, while the gray plusses are for ±2 h around local midnight.

Figure 3.7 shows that Darwin has a larger detection range around local midnight than around local noon, as is expected because of ionization density changes between day and night in the Earth-ionosphere waveguide, leading to lower attenuation for propagation under the nighttime ionosphere than for propagation under the daytime ionosphere [Wait, 1970]. The longer propagation distances during nighttime is typical of the 18 WWLLN stations that were part of the network in April 2005. The plot also shows that during the day, Darwin detects the majority of lightning within ~8 Mm, and the detection ability drops to zero at around 14 Mm. For the other 17 stations, these values ranged from 5 to 10 Mm for noon, and 6 to 13 Mm for midnight. Figure 3.7 also shows that the Darwin station does not detect as large a percentage of strokes within ~0.5Mm of the receiver. Strokes that occur very near Darwin will have low propagation-produced dispersion and may not have a very dispersed waveform at the station. As the dispersion is tested at each station to determine if an observation is consistent with a lightning-produced sferic [e.g., Rodger et al., 2005a], such sferics may be rejected. This rejection may explain the lower detection ability at short ranges from the WWLLN station. The plot shows that during nighttime, the detection ability falls off more slowly with distance, becoming zero around 14-Mm to 15-Mm distance.

The Darwin detection-range findings are representative of all WWLLN stations. Note that the ratio does not reach unity, particularly during local midnight conditions. We interpret this finding as due to lightning detected by the necessary 5 stations without Darwin participating in the detection. Due to higher attenuation in the daytime ionosphere, it is less likely for a sferic to trigger 5 stations excluding Darwin around noon than around midnight, making the maximum noon ratio larger than the maximum midnight ratio. Note that if we only include lightning reported by exactly 5 stations including Darwin, the ratio would always be 1, such that values which lie below 1 are caused by multiple-station detection of lightning. These results could allow more accurate modeling of global detection efficiency, and could be the starting point to address differences in detection efficiency between nighttime and daytime.

By using station detection ranges found for the other stations in this 1-30 April 2005 data set, and by using an average station detection range for stations that were not yet in operation during this time, we generate a map that shows how many stations are within detection range of a given point on Earth. Figure 3.8 and Figure 3.9 show the results of this global model using a 2^{o} latitude x 2^{o} longitude pixel resolution. Figure 3.8 shows results for noon and Figure 3.9 shows results for midnight. Since it is never noon or midnight over the entire globe at once, this representation shows how many stations would be in detection range of each point when that point is at local noon or midnight. The color scale indicates how many stations could participate in locating a stroke at each location. One can see that in the daytime, there are many regions for which the minimum number of stations (5) is not reached. This finding does not mean that lightning will never be located in that region during the daytime since the cutoffs in detection ranges are not sharp as used in the model, but more gradual. For example, for the case of Darwin studied specifically in Figure 3.7, one can see that detection ability for daytime starts falling off around 8 Mm, but does not reach zero until ~ 14 Mm. In Figure 3.8, the regions for which the minimum number of stations is not reached could indicate lower detection efficiency, since it is more unlikely that 5 stations would detect a lightning stroke. In the nighttime, the minimum number of stations covering a given region is 11, so the detection efficiency should be higher and more uniform during the nighttime. This type of plot could be produced on a more regular basis to determine a time-dependent detection efficiency.

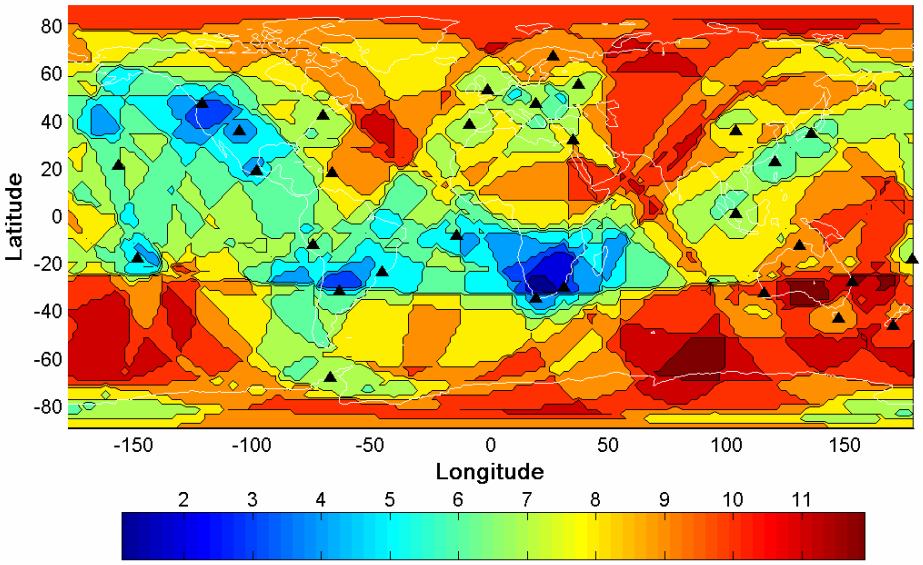

Figure 3.8: Station detection range model for noon. Color scale represents average number of stations that could detect a stroke at a given location. Station locations are indicated by triangles. One can see that the required number of 5 stations is not met in certain regions.

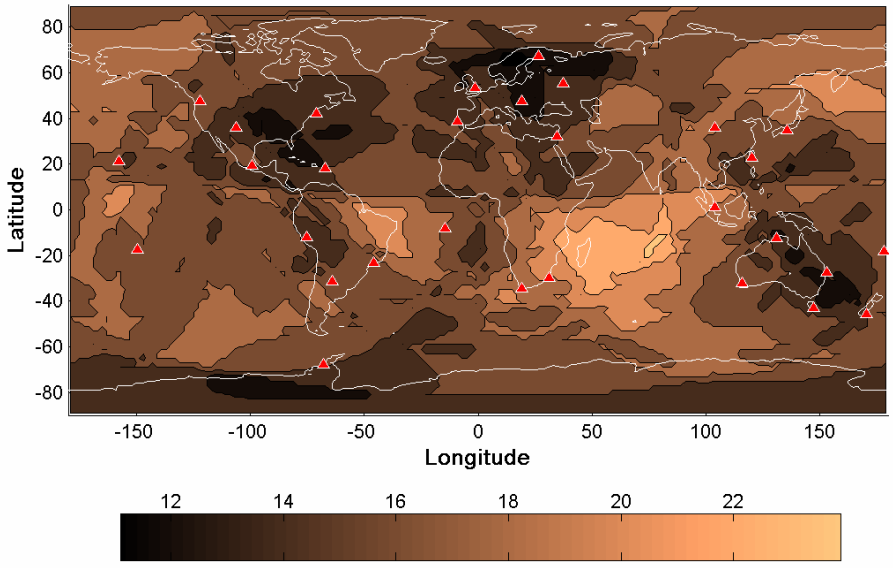

Figure 3.9: Station detection range for midnight. Color scale represents average number of stations that could detect a stroke at a given location. Station numbers are indicated by triangles. One can see that the required number of 5 stations is met in all regions.

3.5 **Conclusion**

These studies to determine detection efficiency, location accuracy, and timing accuracy have provided crucial understanding about the WWLLN that will be used in this dissertation. To summarize these findings, a study of the WWLLN in a "worst-case scenario" in which the closest WWLLN station was > 7000 km away and in which the TOGA algorithm had not been implemented showed a location accuracy of 20.25 ± 13.5 km and a timing accuracy of 0.06 ± 0.2 ms. The comparison between the WWLLN and FORTE PDD optical data produced an experimentally-determined, global relative detection efficiency. It also indicated that the WWLLN detects lightning over the land and over the ocean with comparable efficiency. Finally, the study of detection range of individual WWLLN stations showed that a station can detect lightning out to a range of ~8 Mm during the daytime and to a range of ~12 Mm during the nighttime. The detection range can be used in global modeling of detection efficiency, and, if calculated on a more frequent basis, could be useful in future global detection efficiency models.

Chapter 4: Global Mapping of Strong Lightning

4.1 **Introduction**

After determining a best estimate of global detection efficiency, we would like to use WWLLN to map regions most likely to have significantly-modified ionospheric electron density from lightning EMP. Such a global map of regions with significantly-modified electron density could be used in determining which regions are likely to produce TLEs such as elves or sprites, or would be helpful in further study of the global electric circuit. In mapping such regions, we consider nighttime lightning. During the daytime, the sun is the dominant source of enhanced ionization in the ionosphere. Therefore, EMP from nighttime lightning could have a significant effect on the ionosphere since the solar source is gone. For that reason, we are interested in how much of a region's total lightning occurs under the nighttime ionosphere.

4.2 **Land/ocean events in local time**

Using WWLLN data from 2005, we will show that WWLLN local time variations of flash density are consistent with previous satellite and regional ground-based studies, and can be used as a tool to further study the land/ocean diurnal cycle of lightning in real-time or over a short time scale. Figure 4.1 indicates that WWLLN data, taken over one year and the entire globe, shows a peak in lightning over land in the local afternoon around 1800 local time, and shows that the diurnal cycle of oceanic lightning, while having a much smaller amplitude than that of land lightning, peaks in the morning around 0800 local time. Local time for each stroke is defined as local solar time at the location of the lightning stroke.

This global study shows that the annually averaged WWLLN diurnal variation is consistent with previous studies using satellite optical detectors: Williams et al. [2000] show lightning counts over land peak around 1600 local time while lightning counts over ocean remain relatively constant throughout a local day. Nesbitt and Zipser [2003]

find precipitation features indicating high levels of convection and possibly lightning peak in number around 1500 local time over land, while these precipitation features over ocean have a smaller amplitude in their diurnal cycle and peak in the local morning, around 0500-0700 local time.

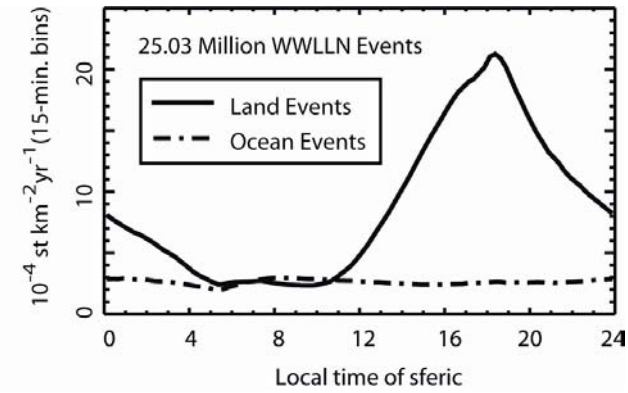

Figure 4.1: One year (2005) of WWLLN flash density data (in units of 10^{-4} strokes per square kilometer per year), separated into land and ocean events, and plotted versus local time in 15-minute bins. The diurnal amplitude variation of land events is about three times larger than the diurnal amplitude variation in oceanic events. Land events peak in the local evening, around 1800 LT, while oceanic events peak in the morning, around 0800 LT.

In addition, WWLLN's real-time global coverage can separate the effects on the diurnal variation of separate continental bodies, seasonal effects, and individual storms. In Figure 4.2 we separate the data from Figure 4.1 into the same six regions as shown in Figure 3.5 to demonstrate WWLLN's capability in studying diurnal lightning variation of geographic regions. Figure 4.2 shows the contribution each region makes to the position of the local time peak in lightning flash density.

The flash density in each region varies based on the strength of the region in producing lightning as well as the WWLLN detection efficiency in that region. For example, WWLLN has the highest detection efficiency in Australasia (region 6), so the lightning flash density is high for that region. Detection efficiency is lower in Africa (region 5), but Africa has the highest flash density of all the regions [Christian et al., 2003], so the WWLLN flash density is also high in that region. The local afternoon peak in land lightning flash density is evident in all regions, but shifted slightly based on region.

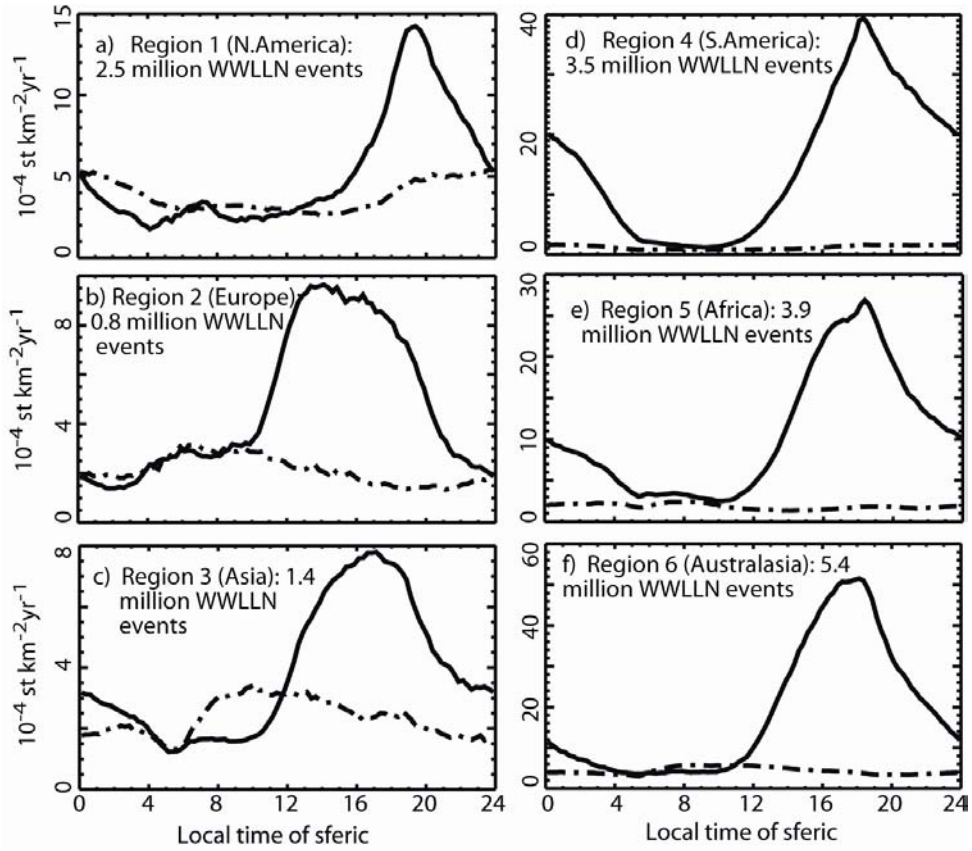

Figure 4.2: The same year of WWLLN flash density data as shown in Figure 4.1, now separated into the six broad regions shown in Figure 3.5. a)-f) show data from regions 1-6, respectively. Similar diurnal patterns are seen in each region. However, the land and ocean peak amplitudes do not occur at the same LT in each region. Poisson statistics define error bars on the order of the width of the line.

To better represent the relative positions of the peak, Figure 4.3 shows land lightning data for all six regions on the same plot, normalized to the same peak amplitude. As the peaks are fairly broad, the center of a full-width-half-max (FWHM) estimate is marked at the top of Figure 4.3, with each adjusted peak labeled by region number. Land lightning over Europe (region 2) peaks earliest, around 1500 local time, while land lightning over North America (region 1) peaks latest, around 1900 LT. The time of peak lightning flash density over North America is consistent with findings from 5-year and 10-year averaged NLDN data that indicate that, in areas of the U.S. with significant diurnal variation, peak lightning flash rates occur between 1600 and 2000 LT [Zajac and Rutledge, 2001; Orville and Huffines, 2001]. Both of these studies looked at

geographic effects on a much finer scale and determined that orography and local continental weather patterns have a large effect on the time of the peak lightning flash rate. Variations in the local time of peak lightning flash rates for the regions presented in this paper may also be due to differing continental weather patterns. WWLLN data could also be used to study smaller-scale variations in any region of the world, although we leave this study for future work.

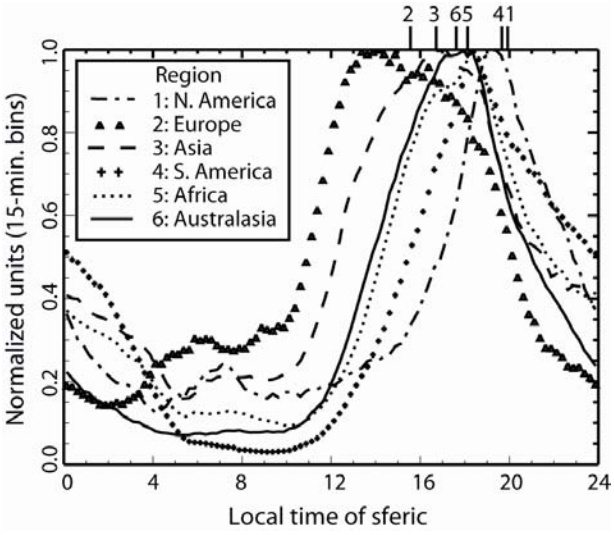

Figure 4.3: Land data from the six regions in Figure 4.2, normalized to unit height and overlaid to observe relative local time positions of the peak amplitude. The center of the FWHM peak for each region is marked at the top of the figure, with region number labeling each adjusted peak. Land flash density in Europe peaks earliest, at 1530 LT, while the land flash density in North America peaks latest, at 1950 LT.

Figures 4.1, 4.2, and 4.3 show that the WWLLN is consistent with previous studies over long durations and can provide new information about geographic effects on high peak current lightning. Moreover, the WWLLN has the advantage of real-time global coverage that satellites cannot achieve, meaning that WWLLN can be used to look for local time variations in the high peak current lightning flash density on shorter time scales. Figure 4.4 shows that the WWLLN can provide a meaningful picture of local time variation in lightning count rates on a five-day time scale. Global lightning flash density, in 15-minute local time bins and separated into land and ocean events, is plotted for 1-5 January 2005 in Figure 4.4(i) and 1-5 July 2005 in Figure 4.4(ii). The global five-day interval was chosen to illustrate the capability of the WWLLN in

studying small time scale variabilities, but essentially any interval of time in any region could be analyzed.

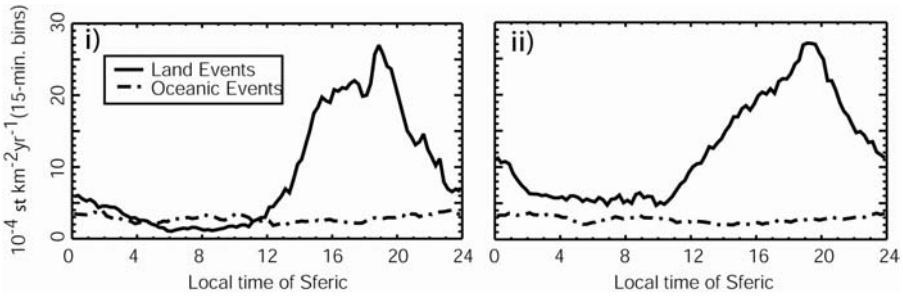

Figure 4.4: Five days of land/ocean WWLLN flash density data (in units of 10^{-4} strokes per square kilometer per year) from 1-5 January 2005 (i) and 1-5 July 2005 (ii). Poisson error bars are on the order of the width of the data line. Using WWLLN, one can study local time variations of lightning during very short time intervals.

By plotting WWLLN flash density versus local time, we see regional differences in the location of the peak lightning flash density in local time. Previous studies have shown that WWLLN detects large peak current lightning strokes [Lay et al., 2004; Rodger et al., 2005a; Jacobson et al., 2006]. Barrington-Leigh and Inan [1999] reported that all CG lightning strokes with peak currents larger than ~50 kA produce doughnut-shaped optical emissions called elves in the lower ionosphere through lightning-generated electromagnetic pulse (EMP). Thus, this local time study of WWLLN strokes over land and ocean effectively shows the regional local time variation of large lightning strokes and therefore elves. The late temporal peak of lightning over land in North America indicates that many large peak current strokes occur under the nighttime ionosphere, where the lightning EMP has a long-lasting effect in the D-layer ionization [Rodger et al., 2001]. We can use lightning count rates in local time to estimate the fraction of elves-producing lightning that occurs under the nighttime ionosphere in each region. We will define the time of the nighttime ionosphere from 1800-0600 LT. Figure 4.5 shows this fraction in each region. More than 60% of lightning in regions 1 and 4 (North and South America) occurs under the nighttime ionosphere, where high peak current lightning strokes can have a long-lasting effect in the D-layer ionization. In contrast, only ~43-44% of lightning in regions 1 and 3 (Asia and Australasia) occurs

under the nighttime ionosphere. This ~20% difference suggests high peak current lightning in the Americas may input a more significant amount of energy into the nighttime ionospheric D-region than would Asia and Australia.

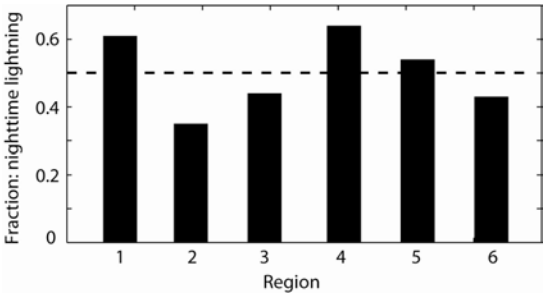

Figure 4.5: Percentage of total lightning in nighttime (1800 – 0600 LT) in each region. More than 60% of lightning in regions 1 and 4 (North and South America) occurs under the nighttime ionosphere, where strong lightning strokes can have a long-lasting effect in the D-layer ionization.

Local time studies of WWLLN lightning data show that peak flash density of strong lightning varies for the different continents by up to five hours in local time. We have suggested that WWLLN data can give an indication of the local time distributions of effects from strong lightning strokes, such as elves, sprites, and electron density and conductivity variability in the lower ionosphere. WWLLN is shown to have the ability to address questions regarding land/ocean lightning differences in local time on any time scale in any location on Earth. WWLLN data could be useful for researchers trying to verify lightning count rates during short campaigns, or, as is commonly the case, during a time when low-Earth orbiting optical lightning satellites are not viewing the regional area of interest. In the next section, local time variations are analyzed at a higher spatial resolution.

4.3 **Events in local time: higher resolution**

In addition to local time effects broken into land and ocean for the six large geographic regions, these local time effects are analyzed with higher resolution. In this case, the chosen resolution is 3.6º x 3.6º bins in latitude and longitude. This bin size is useful because it covers a region about the same size as can be affected by the lightning EMP (200-700 km diameter). The count rate has been scaled by the area of the bin to

reflect number of counts per square kilometer in each bin. The global detection efficiency, as determined by using the regional networks and satellite comparisons discussed in Chapter 3, was used to scale the WWLLN counts, in 1-hour bins. Figure 4.6 shows the total number of nighttime counts, on a $\log_{10}$ scale, for March 2006 - February 2007.

In Figure 4.6, we see that the Central American region has a large amount of nighttime lightning. Central America is also a region that has higher-than-average numbers of detected elves and terrestrial gamma-ray flashes. This analysis shows that possibly this region has large peak current lightning during the nighttime that could be correlated to these increased numbers for energetic lightning effects.

4.4 **Summary**

This analysis has shown that WWLLN can be used to provide an idea of where and when nighttime lightning is prevalent globally. Globally averaged, the data are consistent with satellite measurements of diurnal variation in lightning activity. By separating the WWLLN data into regions – an analysis that is difficult to do with satellite data while still having enough lightning counts to make the results meaningful – we find that more than 60% of lightning in the Americas occurs under the nighttime ionosphere, while less than 40% of lightning in Europe occurs under the nighttime ionosphere. Furthermore, using WWLLN data, we can map global variations of strong nighttime lightning on a much finer spatial scale for different seasons. This information could be useful to determine the timing of future rocket-based, balloon-based, or ground-based campaigns to further study energetic effects of lightning above thunderstorms and in the ionosphere.

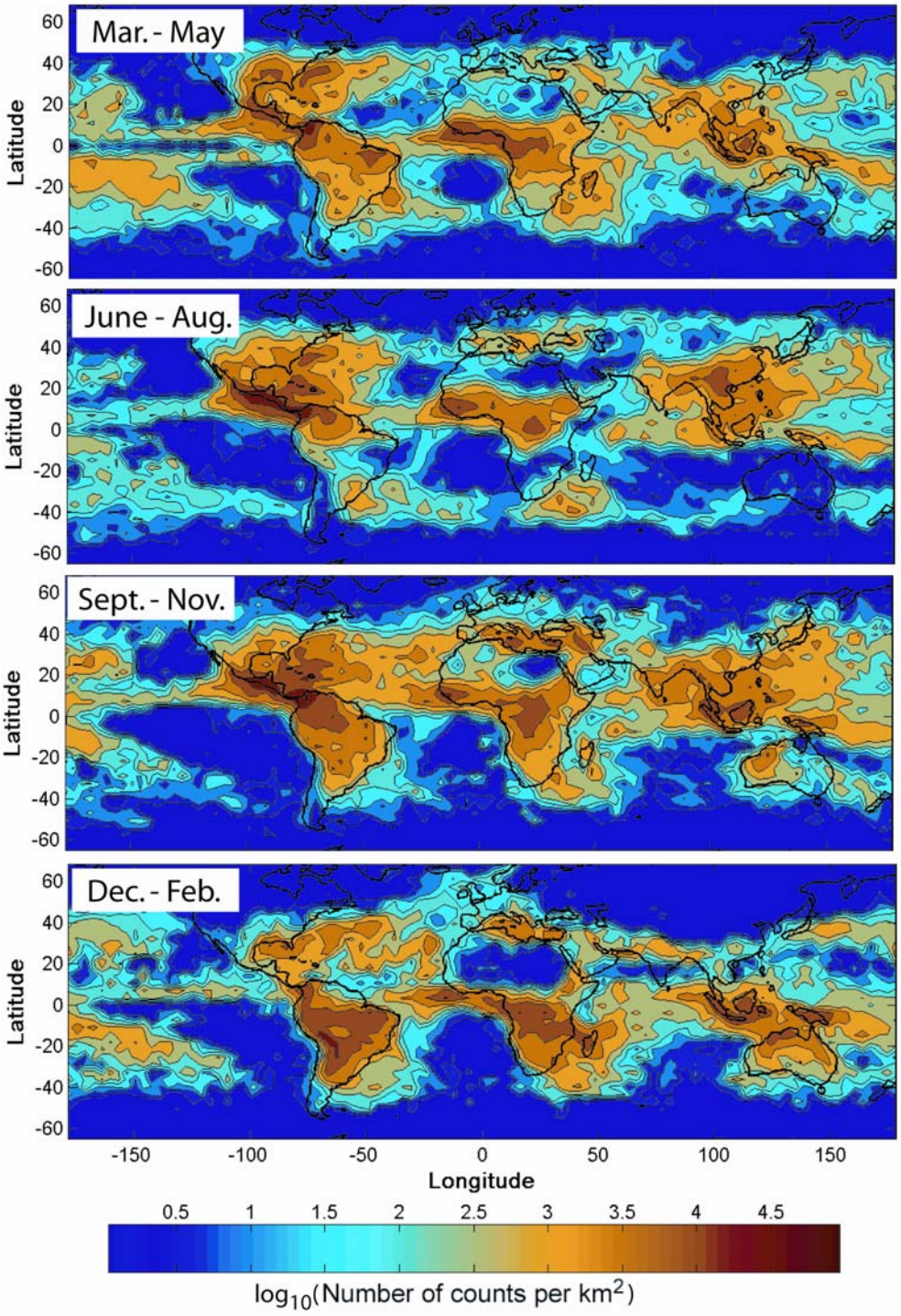

Figure 4.6: Total number of nighttime counts/area for March 2006 – February 2007 on a log10 scale. Bin size is 3.6 x 3.6 degrees in latitude and longitude.

Chapter 5: Narrow Bipolar Events and Ionospheric Propagation

5.1 **Motivation**

As described in Chapter 3, many comparison studies between WWLLN and ground-based regional networks and between WWLLN and FORTE satellite measurements indicated that WWLLN is able to detect in-cloud (IC) lightning. In fact, Jacobson et al. [2006] found that WWLLN detected 4% of lightning with peak current greater than ~40 kA regardless of lightning type. The LASA data in that particular study included more than 50% IC strokes, indicating that WWLLN could detect high-peak current IC lightning.

5.1.1 *FORTE RF/WWLLN Comparison*

In a similar study to that presented in Section 3.3, we have compared WWLLN lightning to lightning detected by the FORTE radio frequency (RF) (3 – 85 MHz) instrument from which one can better understand the type of causative lightning stroke. Unfortunately, the RF instrument stopped working in June of 2003, so the overlapping data set with WWLLN occurs when WWLLN is in its test phase, with receivers only covering Australasia (longitude 60E to 180 E, latitude 40S to 40 N). However, there were about 35,000 FORTE RF events in this region from June 2002 – June 2003 with 1760 coincident WWLLN events. From these coincidences we were able to determine likely lightning types for the coincident WWLLN strokes. A visual inspection of many coincident waveforms revealed that about 10% of the coincident events were IC lightning. Figure 5.1 shows an example of an RF waveform as detected by FORTE that was coincident to a WWLLN event.

Given that narrow bipolar events are thought to make up this category of strong pulse pairs [Smith et al., 1999], this would indicate that WWLLN is able to detect NBEs. A more quantitative comparison made use of predefined criteria on waveform timing, the SNR of the autocorrelation function, total energy and median energy in

order to automatically classify FORTE RF events. This quantitative comparison found that in this region, WWLLN detected coincident events with 5% of the total FORTE RF events, and with 6.9% of FORTE "strong pulse pairs" which are correlated with NBEs. These results suggest that WWLLN preferentially detects NBEs compared to other events detected by the FORTE RF instrument.

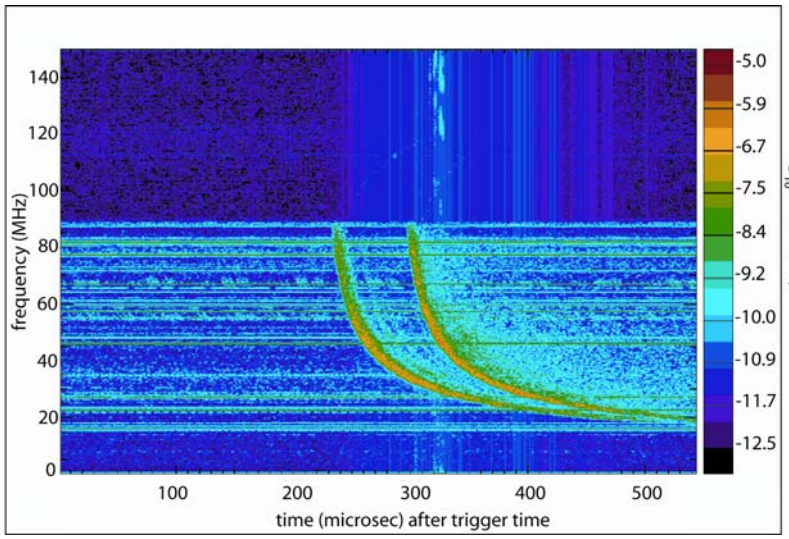

Figure 5.1: Spectrogram of an example of strong IC lightning. The first pulse represents the radio waves that travel directly from the cloud to the satellite, while the second pulse represents the radio waves that bounce off the ground before being detected at the satellite.

5.1.2 *Narrow Bipolar Events Hypothesis*

Based on these findings, we hypothesize that the IC lightning detected by WWLLN mainly consists of Narrow Bipolar Events (NBEs), which are very energetic, extremely short (tens of μs) IC lightning strokes (described in more detail in Section 1.2).

We investigate this issue further by completing another WWLLN/LASA comparison, similar to that of Jacobson et al. [2006]. However, this time waveforms of the coincident IC-classified events were analyzed in addition to simply using the automatic LASA classification to determine what types of lightning are seen by WWLLN. This investigation will be discussed in Section 5.2.

5.2 **Narrow Bipolar Events: WWLLN/LASA coincidence study**

5.2.1 *Method*

This study searched for WWLLN events coincident within 2 ms and 200 km of a LASA event with an archived NBE/Fast Pulse (FP)-classified waveform. The NBE classification is done via an automatic procedure based on the relationship between the signal-to-noise ratio and the rise-plus-fall time of the initial pulse. The FP classification includes events that are very narrow temporally, but do not have such high signal-to-noise ratios as NBEs. Both NBEs and FPs are then classified as in-cloud, since it is assumed that cloud-to-ground processes cannot occur on this time scale [Smith et al., 2002]. The full NBE/FP waveforms have been archived for 49 days in 2006: May 02-08, 10, 13-18, 20-30; June 01, 07-22, 30; and July 01-07. Only at LASA events detected by the Great Plains Network, covering the region 107.3 W to 95.3 W and 43.3 N to 31.3 N, were included in this study.

5.2.2 *Results*

Twenty-two WWLLN events were coincident with a LASA event using this criteria. This small number of coincidences was surprising when compared with the large number of FORTE RF coincidences. While this is still not well understood, this small number of coincidences could stem from many sources. The location and time of the two comparisons differ. It could be that WWLLN does not detect NBEs as efficiently in the U.S. Great Plains as in Australasia, or it could be that NBEs comprise a smaller percentage of total lightning events in the Great Plains region. Upon examination of the waveforms of these events, we find that 3 are unambiguously NBEs. The three coincident WWLLN/LASA NBE events all occur on the same day, 26 May 2006, and are detected by only the 5 nearest WWLLN stations: Seattle, Boston, Los Alamos, Mexico City, and Puerto Rico. Figure 5.2 shows the full waveform as detected by 5 LASA stations. Each panel shows a waveform detected by a different station, along with the distance (range) between the lightning stroke and each station. The top

panel represents the closest station to the stroke and the bottom panel the farthest station from the stroke. Because the stations are different distances from the lightning stroke, the signal arrived at each with different time delays. The trigger time at each station is represented at zero μs, and the x-axis label of each panel tells how large of a time delay that trigger time is from the lightning stroke time. In the first three panels, one can see the narrow-bipolar nature of the signal, with the initial rise above zero V/m, and then fall to below zero V/m. In the first two panels, one can clearly see the two ionospheric reflections of the signal: the first reflection reflects from the ionosphere and

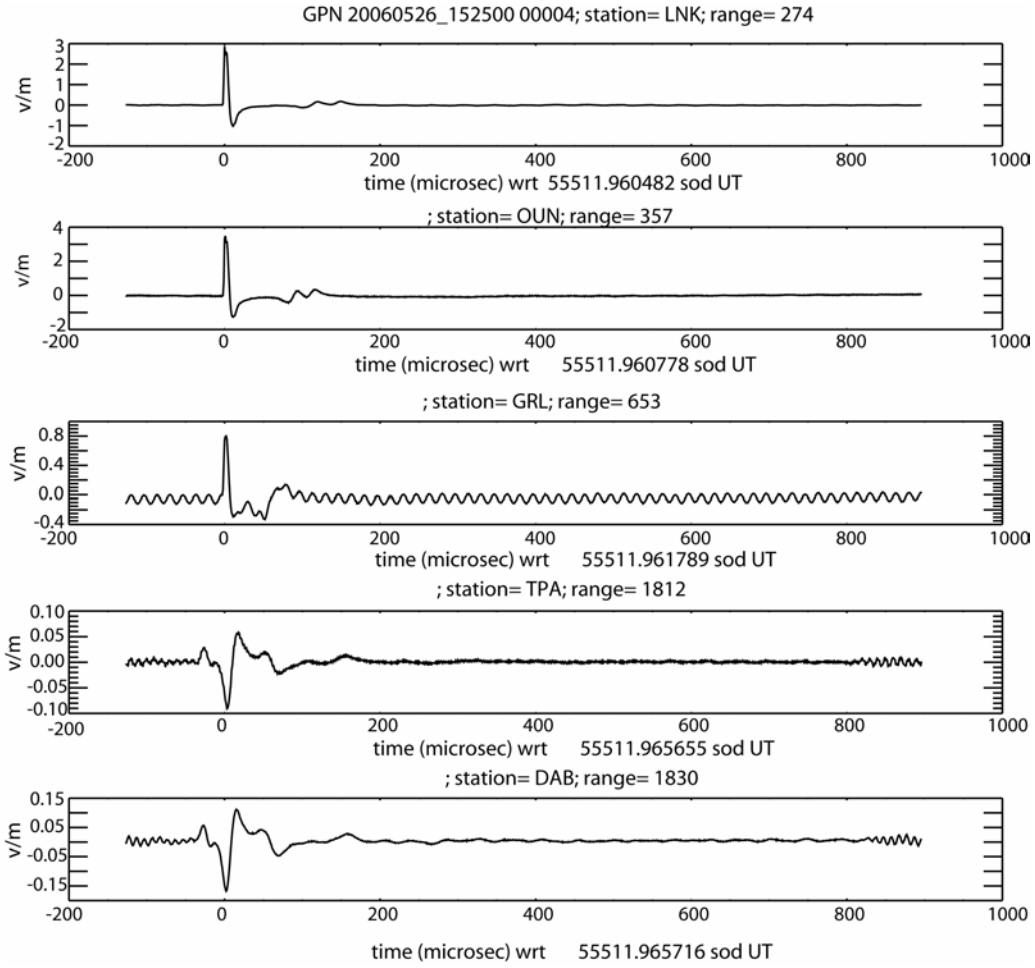

Figure 5.2: Full NBE waveform as detected by 5 LASA stations. Each panel shows a waveform detected by a different station, along with the distance (range) between the lightning stroke and each station. The trigger time at each station is represented at zero μs, and the value of seconds of day (sod) below each panel shows time delay between lightning stroke time and trigger time.

then reaches the detector; the second reflects off the ground, then the ionosphere and then reaches the detector. In the bottom two panels, the ground pulse has decayed over distance, so the detector triggers on the reflection pulses, which is why the narrow bipolar nature is no longer evident.

In order to compare lightning strokes of different magnitudes, we normalize the electric field of the sferic to a range of 100 km, using a radial amplitude attenuation over distance of r^{-1} for LF radiation along a line of sight. For normalization, we choose one of the waveforms of the same stroke detected at multiple stations based on the largest signal-to-noise ratio, and with the requirement that the stroke be farther than 100 km from the receiver (to avoid electrostatic signatures). The waveform shown in the first panel of Figure 5.2 is normalized in this manner in Figure 5.3. This waveform is detected by the LNK station at a range of 274 km, and then normalized to 100 km.

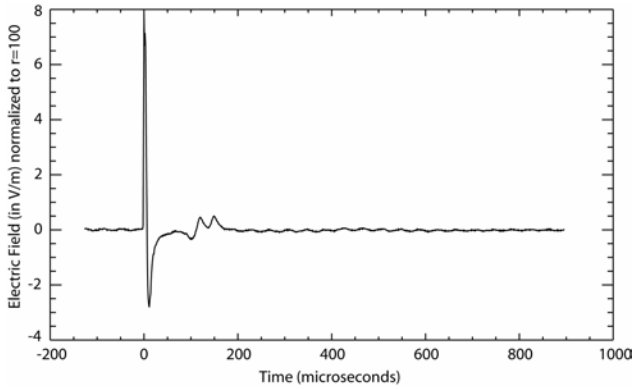

Figure 5.3: Range-normalized electric field of a NBE sferic detected by the LNK station at a range of 274 km, and then normalized to 100 km, using 1/r amplitude attenuation.

From the range-normalized electric field, we find the power spectrum, to determine how much power is radiated versus frequency, as WWLLN detects sferics in the 1 to 24 kHz range. Figure 5.4 shows the power spectrum of the sferic in Figure 5.3. We then integrate power over frequency: first, we integrate over the entire frequency band to get the total power in the waveform. Second, we integrate the power over only the VLF band (1 to 24 kHz) to determine how much power is radiated in the WWLLN-detectable

range. In a typical NBE, about one third of the total power is emitted in the 1 to 24 kHz range.

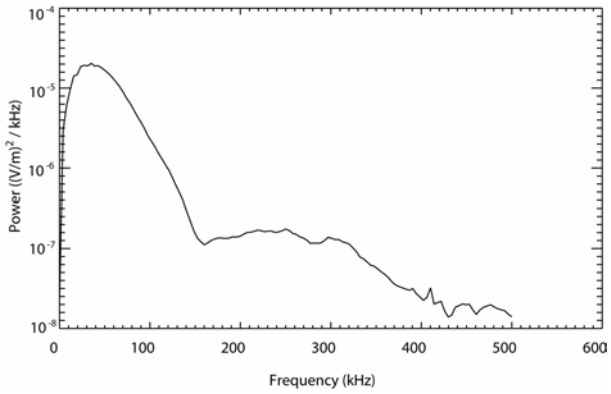

Figure 5.4: Power spectrum of the sferic in Figure 5.3.

We will next investigate the 19 coincident WWLLN/LASA events in the NBE/FP category that have ambiguous waveforms. Figure 5.5 shows one of these waveforms, as detected by 5 LASA stations. This waveform has a very fast rise time (~15 μs), typical of a NBE but the lack of a clear ionospheric reflection of the pulse indicates that this may be a cloud-to-ground stroke. Also, instead of being detected by only the 5 closest WWLLN stations, as would be likely if the NBE had very little power in the VLF band, these events often triggered WWLLN stations half way around the world. These two pieces of evidence suggests that the automatic LASA classification of FPs as ICs may be erroneously classifying strange CG events as IC lightning. Possibly many of WWLLN events coincident with LASA "IC events" in the Jacobson et al. [2006] study were of this type.

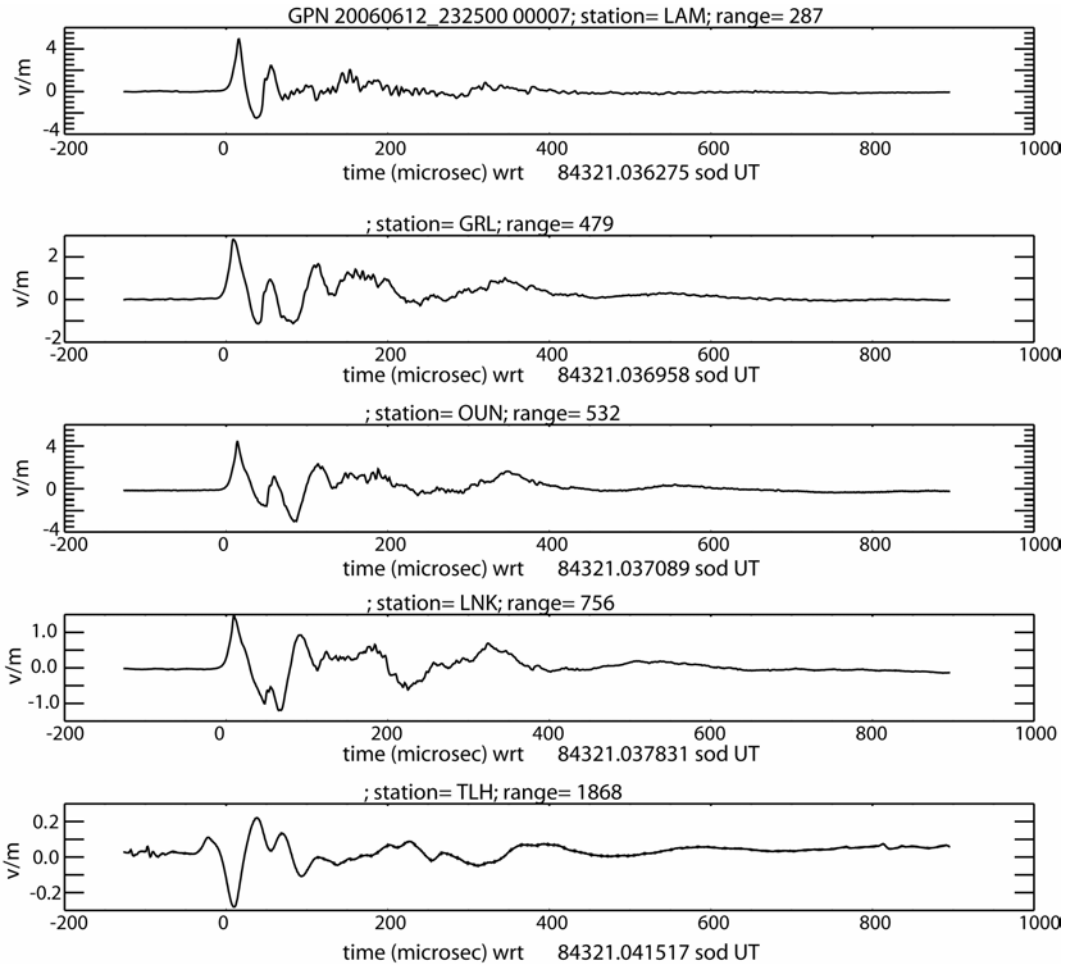

Figure 5.5: Full FP waveform as detected by 5 LASA stations. Each panel shows a waveform detected by a different station, along with the distance (range) between the lightning stroke and each station. The trigger time at each station is represented at zero μs, and the value of seconds of day (sod) below each panel shows time delay between lightning stroke time and trigger time.

In order to better determine what about the WWLLN-detected NBEs makes them detectable, those three NBEs are compared with the total 218 NBE/FP-classified events that occurred on 26 May 2006. Figure 5.6 shows the ratio of VLF power to total power along the horizontal axis versus total VLF power on the vertical axis. The coincident NBEs are in red. One can see that many of the NBE/FPs have low VLF power, and the coincident NBEs have a ratio of VLF power to total power around 0.3.

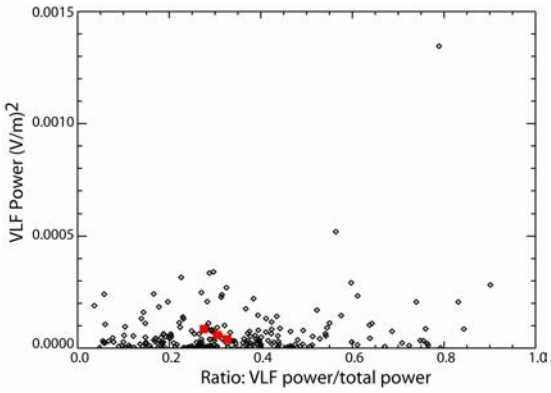

Figure 5.6: Ratio of VLF power to total power along the horizontal axis versus total VLF power on the vertical axis. The coincident NBEs are in red.

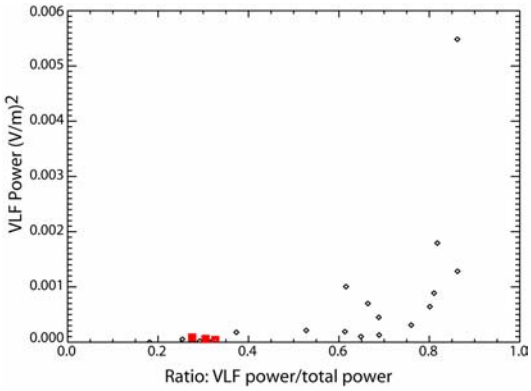

Figure 5.7: Same type of plot as Figure 5.6, but showing only the 22 coincident WWLLN/LASA sferics.

Figure 5.7 shows the same type of plot as Figure 5.6, but with only the 22 coincident WWLLN/LASA sferics. Here, we see that the VLF power ratio of the three WWLLN-detected NBEs is on the very low end of coincident events, indicating that the radiated VLF energy from these NBEs may be very close to the WWLLN-detection threshold for strokes in the LASA-covered region. It is possible that only very powerful NBEs located within a reasonable distance of 5 WWLLN stations have enough VLF energy to trigger the required 5 WWLLN stations.

5.3 **Conclusions**

Based on comparisons with LASA ground-based waveforms and FORTE RF satellite-based waveforms, the WWLLN network is able to detect NBEs if the NBE is

powerful enough to trigger 5 required stations. In the region covered by the LASA Great Plains network (107.3 W to 95.3 W and 43.3 N to 31.3 N) the majority of NBEs seem unable to trigger the required 5 stations. However, in the Austral-asia region in 2003, a large percentage of NBEs detected by the FORTE RF instrument were coincident with WWLLN events, indicating that either NBEs radiate more energy from Austral-asian storms, or similarly energetic NBEs are more likely to be detected by 5 WWLLN stations due to higher station density.

We also find that many of the LASA-classified FPs do not have waveforms that are unequivocally IC lightning strokes. In fact, the majority of LASA FP/WWLLN coincidences were detected by extremely distant WWLLN stations (up to halfway around the world), a finding that is more consistent with CG lightning.

Chapter 6: Experimental evidence of energetic lightning effects on ionosphere and magnetosphere

6.1 **WWLLN/ISUAL elves comparison**

6.1.1 *Motivation*

The ISUAL instrument has been taking optical images and spectroscopy data on elves globally since May of 2004. We were provided ISUAL elves data for October 2005 by Dr. Harald Frey of the Space Sciences Lab at UC Berkeley. In order to more accurately determine the location and time of the elve-producing lightning, it is useful to have ground-based measurements of lightning activity. WWLLN is particularly useful in this case because it is the only network able to detect lightning globally, so it could potentially enhance information of elve-producing strokes over oceans where there is no other lightning coverage. It has been found that detected elves are more often seen over water, so this oceanic coverage is particularly important if the majority of elves occur over water, and if one intends to determine the difference between elve-producing conditions and non-elve producing conditions. WWLLN data also is able to provide better location and timing information on ISUAL-detected elves that occur in regions without coverage from any other lightning detection network.

6.1.2 *Method*

We look for ISUAL elve/WWLLN lightning coincidences occurring during October 2005 by using the following criteria: Time-difference between WWLLN lightning stroke and elve detected by ISUAL, corrected for the time of flight from the WWLLN location to the satellite, must be less than or equal to 200 ms and the distance difference between WWLLN location and ISUAL-estimated elve location must be less than 1500 km. Because the satellite observes elves from 1000 to 4000 km away, the magnitude of the timing error introduced by considering time of flight from the WWLLN location (on the ground) to satellite instead of from 90 km above the ground-

based WWLLN location (elves altitude) is a maximum of 10 μs. We plot the time difference histogram of coincidences meeting these two criteria in Figure 6.1, and from this plot we further reduce the coincident data set to contain the closest matches (time differences between -5 and 15 ms). A zoomed-in version of the close coincidences is shown in Figure 6.3.

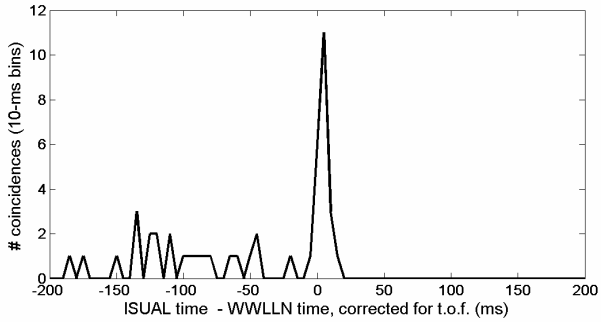

Figure 6.1: Time difference histogram of all coincident WWLLN lightning/ISUAL elves. Positive values indicate that the elve occurred *after* WWLLN stroke time. The background level for negative time differences is higher than for positive, meaning that WWLLN often detects a subsequent stroke from the elve-causative stroke, but never an earlier stroke than the elve-producing stroke.

6.1.3 *Results*

We find that 29 of 159 elves have one or more coincident WWLLN events within 200 ms and 1500 km (18.2%). Of those 29 elves, 13.8% of the total, or 22 elves, are in the closely coincident subset (time differences between 5 and 20 ms). The locations of all elves detected by ISUAL in October 2005 (blue dots) along with the WWLLN locations (green stars) and ISUAL locations (red dots) of the closely coincident events are plotted in Figure 6.2. Close coincidences are found in all regions, meaning that WWLLN seems to be able to detect elve-producing strokes fairly uniformly over the world.

Next, we study the information from the comparison in timing differences between WWLLN lightning strokes and ISUAL-detected elves. As can be seen from Figure 6.1, the background level of coincidences on the left side of the peak (negative time differences) is higher than on the right side, meaning that WWLLN often detects a subsequent stroke from the elve-causative stroke, but never an earlier stroke than the

elve-producing stroke. An interpretation of this result is that elves are most often caused by the first stroke in the flash.

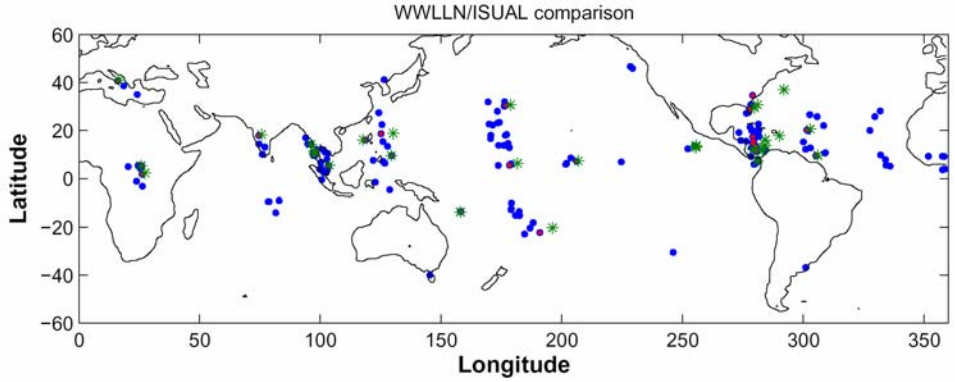

Figure 6.2: Locations of all ISUAL-detected elves (blue dots), locations of elves closely coincident to a WWLLN stroke (red dots), and locations of WWLLN lightning locations (green stars) closely coincident with an ISUAL detected elve. Coincidences are found in all regions, meaning that WWLLN seems to be able to detect elve-producing strokes fairly uniformly over the world.

Figure 6.3 shows a zoomed-in view of the histogram in Figure 6.1 to look at only the close coincidences with time differences between -5 and +15 ms. For these close coincidences the WWLLN stroke precedes the elve by 4.8 ± 3.4 ms, where 3.4 ms is the standard deviation. This indicates that ISUAL timing may be late by ~3.5 ms in order for the timing to be consistent with electromagnetic theories of elves (speed-of-light propagation of the EMP would result in an elve 1 to 2 ms after the lightning stroke).

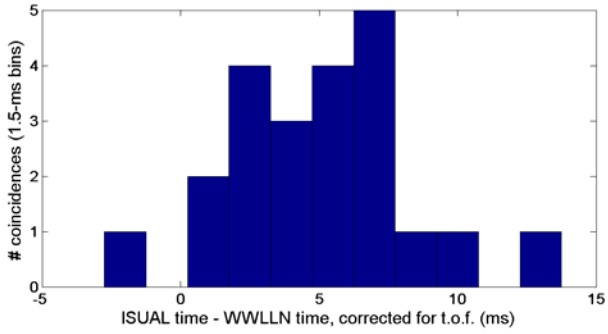

Figure 6.3: Time difference between ISUAL elve and WWLLN stroke. Only closely coincident events are included in this histogram. These coincidences indicate that typically the stroke precedes the elve by 4.8 ± 3.4 ms, indicating that ISUAL timing may be late by ~3.5 ms in order for the timing to be consistent with electromagnetic theories of elves.

ISUAL data analysis provides an estimate of the latitude and longitude of the detected elves. Next, we analyze that location estimate by using the location of the closely coincident WWLLN events as "ground truth". As discussed above, previous studies have shown WWLLN location accuracy to be ~15 km [Jacobson et al., 2006, Rodger et al., 2005a]. To provide this error analysis of ISUAL-estimated locations, we look at the distance separation between the WWLLN location and the ISUAL-estimated elve location for the closely coincident events. Figure 6.4 shows that the majority of close coincidences have a distance separation of less than 400 km even though the imposed criteria for a coincidence allowed a distance separation of 1500 km.

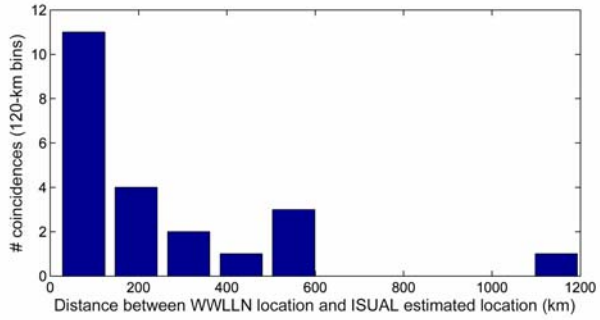

Figure 6.4: Distance separation (km) between WWLLN location and ISUAL estimated location. Even with a 1500 km distance limit, the majority of coincidences have a separation of less than 400 km.

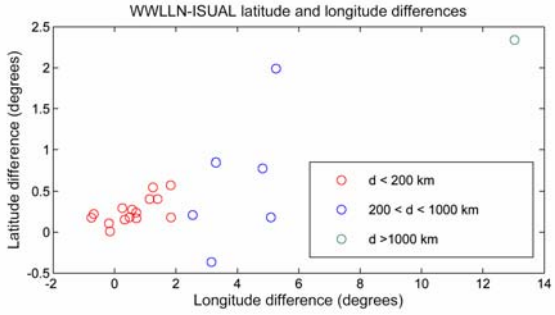

Figure 6.5: Latitude and longitude differences between WWLLN locations and ISUAL estimated locations shows a consistent skew. ISUAL typically estimates a location that is too far west and too far south. Error is 2.1 ± 3.0 in longitude degrees and 0.45 ± 0.61 in latitude.

As shown in Figure 6.5, latitude and longitude differences between WWLLN locations and ISUAL estimated locations shows a consistent skew to the estimated ISUAL location. The ISUAL processing algorithm systematically estimates a location

that is too far west and south. The error in latitude and longitude is 0.45 with a standard deviation of 0.61 in latitude and 2.1 with a standard deviation of 3.0 in longitude degrees. We look at these same data in a slightly different manner in Figure 6.6, in which we plot the distance between the ISUAL sub-satellite point and the WWLLN location versus distance between ISUAL-estimated elve location and WWLLN location. As shown in Figure 6.6, the error in the ISUAL estimated elve location begins increasing rapidly at a sub-satellite distance of more than 3100 km from the WWLLN stroke.

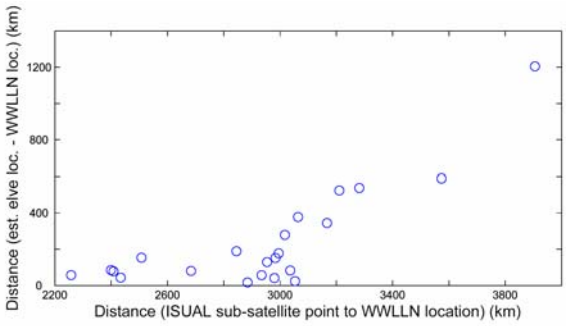

Figure 6.6: Distance between ISUAL sub-satellite point and WWLLN location is plotted versus distance between ISUAL-estimated elve location and WWLLN location. Error in ISUAL-estimated elve location begins increasing rapidly at a sub-satellite distance of more than 3100 km from WWLLN stroke.

Next, we investigate possibilities for the increased error at distances of greater than 3100 km in Figure 6.6 by looking more closely at the coincident event with the greatest location error (~1200 km). Figure 6.7 represents the spatial configuration of the ISUAL sub-satellite point (red diamond), ISUAL-estimated elve location (blue diamond), and WWLLN location (blue asterisk) for that particular coincident event. The estimated elve location is between the sub-satellite point and the WWLLN location. In this case, an elve that is estimated to have occurred over land, may have actually occurred over the ocean.

We look further into the systematic error made evident by Figure 6.5 by studying the spatial configurations of 4 more coincident events (plotted in Figure 6.8). The symbols are the same as in Figure 6.7. We find that ISUAL data processing consistently estimates the elve to be closer to the satellite than it actually is. A hypothesis as to the

cause of this systematic error is that the elves actually occur over the visible horizon (~3100 from the spacecraft), and yet the processing algorithm assumes they must be closer than the horizon. If the data is reprocessed allowing the possibility of the elve to occur over the horizon, then a much closer estimate to the WWLLN location results. Reprocessing the event with a 1200 km location error makes the distance error less than 400 km.

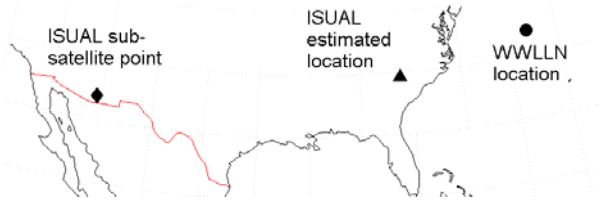

Figure 6.7: The spatial configuration of ISUAL sub-satellite point (diamond), estimated ISUAL elve location (triangle), and WWLLN location (circle) for the coincident elve event (at 4:44:34.646 UT on 1 October 2005) with distance error of ~1200 km. In this case, an elve that is estimated to have occurred over land, may have actually occurred over the ocean

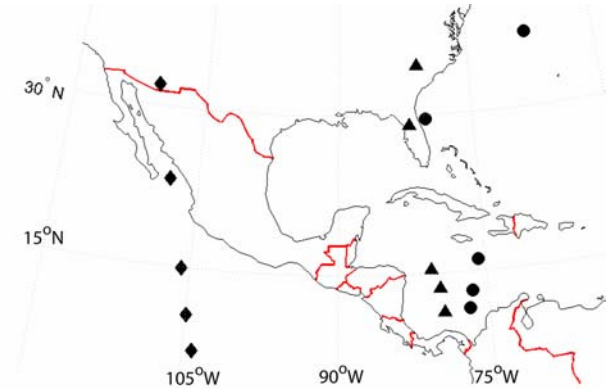

Figure 6.8: More relative locations of satellite (diamonds), elve location estimate (triangles), WWLLN location (circles). It seems that ISUAL estimates the elve to be closer to the satellite than it actually is. The uppermost event is the same as that in Figure 6.7.

Finally, we look at a few case studies of elves with all local WWLLN lightning are also shown (as opposed to only coincident elves/WWLLN events). Figure 6.9 shows results from the first case study, on 27 October 2005. Elves detected in the region are shown as asterisks. Green triangles represent elves that are coincident with a WWLLN stroke. Red triangles are elves without a coincident WWLLN event. Blue dots represent all WWLLN lightning occurring in this region between 2 hours before the first detected

elve in Figure 6.9 and 2 hours after the last detected elve. Red circles show the WWLLN locations coincident with the elve in red. The one coincident elve is located in a region with no lightning activity, but is matched to a stroke in a storm 344 km to the east of the estimated elve location. Since the two elves without coincidences are also in the middle of a region with no lightning, one might guess that they too should be associated with the storm to the east. From this example, we learn that WWLLN can be used to more accurately locate more elves than just the coincident elves.

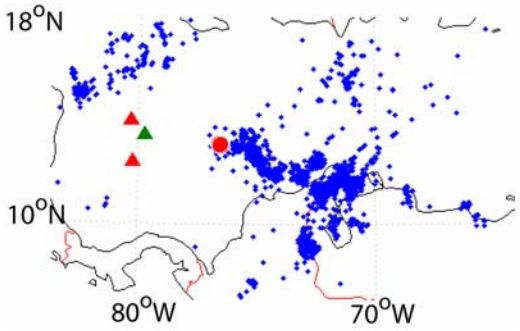

Figure 6.9: Elves detected on 27 October 2005 are shown as green triangles if they are coincident with a WWLLN stroke and red triangles if they are not coincident with a WWLLN event. Blue dots represent all WWLLN lightning within 2 hours of detected elve. The one coincident elve is located in a region with no lightning activity, but is matched to a stroke (red circle) in a storm 344 km to the east of the estimated elve location. Since the two elves without coincidences are also in the middle of a region with no lightning, one might guess that they too should be associated with the storm to the east.

In the second case study (Figure 6.10), elves are situated immediately above active lightning regions, even though there are no coincident strokes. Six non-coincident elves (red triangles) in one night are located very near to WWLLN-located lightning regions (blue dots represent WWLLN lightning). This type of analysis indicates that WWLLN is able to measure elve-producing storm regions, even if it does not detect the coincident lightning stroke. Further study must be done to distinguish elve-producing WWLLN-lightning regions from non-elve-producing regions by studying the differences in lightning characteristics between the two regions.

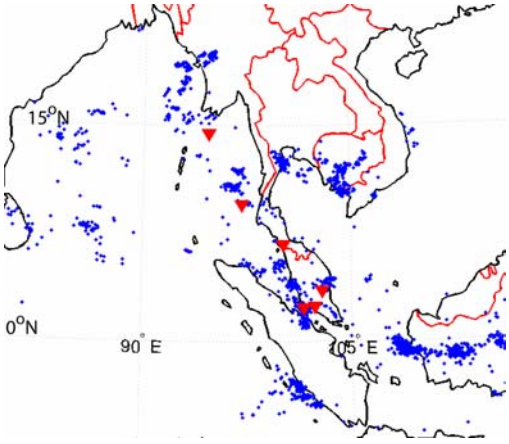

Figure 6.10: Six non-coincident elves (red triangles) in one night (9 October 2005) are located very near to WWLLN-located lightning (blue dots). This type of analysis indicates that WWLLN is able to measure elve-producing storm regions, even if it does not detect the coincident lightning stroke.

6.1.4 *Discussion*

From the comparison of WWLLN lightning events to ISUAL-detected elves during October 2005, we find close coincidences globally, meaning that WWLLN seems to be able to detect elve-producing strokes fairly uniformly over the world (Figure 6.2). Secondly, we find that WWLLN often sees subsequent strokes from the same lightning flash (Figure 6.1) but not previous strokes. An interpretation of this result is that elves are most often caused by the first stroke in the flash. The comparison has also shown that it is possible to use WWLLN data to more accurately locate ISUAL-detected elves. This could be useful for determining the relative frequencies of elves over land versus over water by more accurately locating the elves over land or water. Finally, we find that WWLLN is able to measure elve-producing storm regions, even if it does not detect the coincident lightning stroke (Figure 6.10). Further study should be done to try to distinguish elve-producing WWLLN-lightning regions from non-elve-producing regions. In particular, the energy-calibrated WWLLN may help in this endeavor, to determine the strength of lightning strokes in given storms as well as how much energy is input in the lower ionosphere from elve-producing strokes.

6.2 **WWLLN/RHESSI TGF comparison**

6.2.1 *Motivation*

RHESSI-detected terrestrial gamma-ray flashes are similar to ISUAL-detected elves in that they are also energetic events associated with lightning and detected by a satellite. Similarly, WWLLN will be useful to provide information on TGFs on a global scale because it has global lightning coverage. In the TGF case, we use WWLLN locations to determine possibilities for the beaming of gamma-ray energy. We also use WWLLN data to help determine the magnitude of lightning possibly associated with TGFs.

6.2.2 *Method*

The method of comparison for WWLLN lightning and RHESSI-detected Terrestrial Gamma-Ray Flashes (TGFs) is similar to that of the WWLLN/ISUAL comparison. We look for RHESSI TGF/WWLLN lightning coincidences occurring between June 2002 and October 2006 by using the following criteria: Time-difference between WWLLN lightning stroke and RHESSI-detected TGF, corrected for the time of flight from the WWLLN location to the satellite, must be less than or equal to 200 ms and the distance difference between WWLLN location and RHESSI-estimated TGF location must be less than 1500 km. We plot the time difference histogram of coincidences meeting these two criteria in Figure 6.11, and from this plot we further reduce the coincident data set to contain the closest matches (time differences between –3.0 and 5.0 ms). Again, the time of flight between the source and satellite was taken into account for all time differences.

6.2.3 *Results*

Of the 713 TGFs detected by RHESSI during this time period, 64 have one or more coincidences with WWLLN events within 200 ms and 1500 km (9.0%). Using the criteria for closely coincident events, we find that 31 of those 64 TGF/ WWLLN

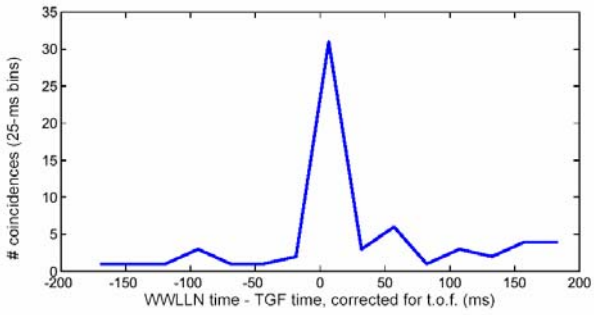

Figure 6.11: Time-difference histogram of all coincident events. Positive values of the time difference indicate that the TGF occurred *before* the WWLLN stroke time.

coincidences have a time difference between –3.0 and 5.0 ms (4.3%). Figure 6.12 shows these results graphically. Locations of all TGFs (blue dots), locations of TGFs closely coincident to a WWLLN stroke (red dots), and locations of WWLLN lightning locations (green stars) closely coincident with a TGF. The percentage of TGFs coincident with WWLLN strokes (4.3%) is similar to the detect efficiency for high peak current strokes as found in Jacobson et al. [2006]. This possibly indicates that RHESSI-detected TGFs are produced by lightning strokes with peak current greater than ~40 kA.

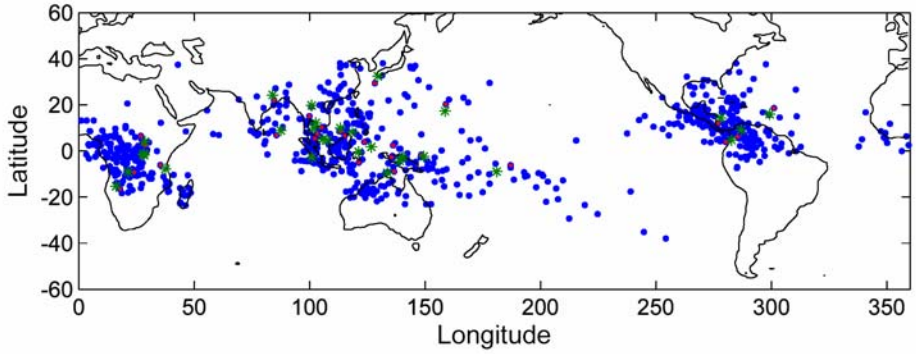

Figure 6.12: Locations of all TGFs (blue dots), locations of TGFs closely coincident to a WWLLN stroke (red dots), and locations of WWLLN lightning locations (green stars) closely coincident with a TGF.

Next we analyze the average time differences of the close coincidences in Figure 6.13 and we find that the TGF precedes the stroke by 1.1 ± 1.2 ms. This is consistent with findings from other comparisons between ground-based lightning detection networks and RHESSI-detected TGFs: Cummer et al. [2005] found 13 TGFs preceding

strokes detected by the Duke University electric field sensor by 1.24 ± 0.97 ms, and Stanley et al. [2006] found 5 TGFs preceding LASA-detected lightning by 1.8 to 5.1 ms.

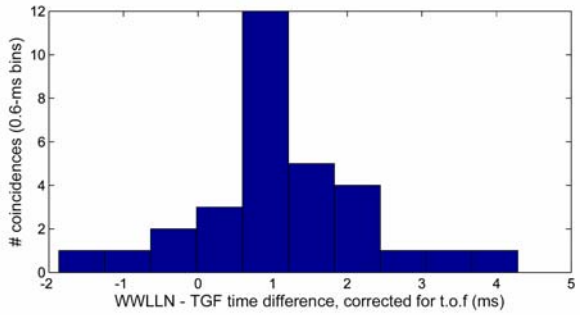

Figure 6.13: Time difference between TGF time and WWLLN stroke time, corrected for the time of flight to the satellite. Only closely coincident TGFs are included in this histogram. These coincidences indicate that typically the TGF precedes the stroke by 1.1 ± 1.2 ms.

Next we study the distance separation between coincident lightning and the RHESSI sub-satellite point in order to address the question of whether TGF energy is tightly beamed or not. The majority of close coincidences have a separation between WWLLN location and RHESSI sub-satellite point of less than 400 km (Figure 6.14). The mean separation is 373 km, with standard deviation of 169 km. However, the maximum distance separation is ~700 km, giving the first indication that TGF-energy may not be tightly beamed from the source.

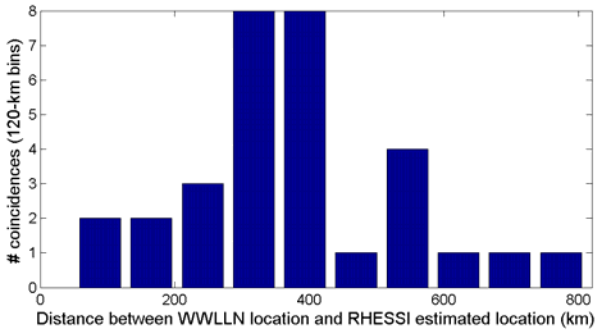

Figure 6.14: Distance between WWLLN location and RHESSI sub-satellite point. Even with a 1500 km distance limit, the majority of close coincidences have a separation of less than 400 km. The mean separation is 373 km, with standard deviation of 169 km.

6.2.4 *Summary*

In this comparison, we find close coincidences in all global regions, meaning that WWLLN seems to be able to detect TGF-producing strokes fairly uniformly over the world (Figure 6.12). The percentage of TGFs coincident with WWLLN strokes (4.3%) is similar to the detection efficiency for high peak current strokes as found in Jacobson et al. [2006]. This finding indicates that RHESSI-detected TGFs are possibly produced by lightning strokes with peak current greater than ~40 kA. In the comparison of time differences between TGFs and WWLLN strokes, we find that WWLLN sees fewer preceding strokes than subsequent strokes from the TGF-coincident lightning stroke (Figure 6.11). A possible interpretation of this result is that TGFs are most often caused by the first stroke in the flash, but not always. A study of the distances between the RHESSI sub-satellite point and WWLLN location gives no evidence for a small beaming angle of the TGF energy as the separation could be greater than 700 km.

Similarly to the investigation of elves, a calibrated stroke energy estimate from WWLLN would also enhance the knowledge of how strong a stroke must be to produce a TGF, as well as how much energy is input to the magnetosphere from TGFs globally.

Chapter 7: Lightning stroke radiated VLF energy

7.1 **Motivation to provide stroke energy**

The WWLLN has been providing accurate lightning locations and times globally for the past five years. An important next step in its development is to implement an algorithm that estimates stroke-radiated energy along with its location and time. No other network or satellite has the capability to monitor the strength of lightning strokes globally, and this additional capability would enhance the possibilities for a variety of studies in lightning science. Most notably it would provide useful data for a study of how lightning energy can affect lower-ionospheric electron density and conductivity on a global scale. Using radiated energy estimates, we could determine when in local time and where on Earth the strongest lightning occurs. Also, knowing which storms contain the strongest lightning strokes would help in determining which storms globally are most likely to affect conductivity in the lower ionosphere. Also, this information would be useful in order to correlate elves detected by ISUAL and TGFs detected by RHESSI with lightning strokes world-wide with known stroke energy. This comparison may help determine the conditions necessary for elves and TGFs as well as predictions for regions most likely to be affected by these phenomena. The steps taken to determine the stroke energy are explained in this chapter.

7.2 **Absolute Calibration**

The radiated energy of a vertical cloud-to-ground lightning stroke propagates outward from the lightning stroke, mainly confined in the Earth-Ionosphere waveguide (EIWG). A given WWLLN station measures the uncalibrated, integrated energy flux at the station location as described in Section 2.3. As a reminder, this quantity has been defined as

$$Y = \sum_{samples} \frac{(E')^2}{c\mu_0} \Delta t, \tag{7.1}$$

where E' is the uncalibrated electric field as shown on the y-axis of Figure 2.3, c is the speed of light, $\mu 0 = 4\pi * 10^{-7}$ W/(A*m), and Δt=1/(sampling frequency). In order to know the calibrated electric field in units of V/m, E, we must determine the conversion factor, A_n, to convert computer sound card units to V/m for each station *n*. This conversion factor is influenced by two variables. The first variable is the system gain that depends on antenna configuration, preamplifier gain, service unit gain, and sound card gain. The system gain could potentially be calculated by subjecting each station to similar calibration procedures. The second variability results from different electrical effects due to site geometry (i.e. location of the antenna on building roof relative to other buildings, the quality of the ground plane to which it is connected). The electrical environment variability may be much more difficult to determine than the system gain.

If station conversion factors are determined, we may define the absolute electric field as detected at station *n* as $E = E'A_n$. The calibrated integrated energy flux at a given station is:

$$W(energy/m^2) = \sum_{samples} \frac{E^2}{c\mu_0}\Delta t = \sum_{samples} \frac{(A_n E')^2}{c\mu_0}\Delta t = YA_n{}^2. \qquad (7.2)$$

Here we have assumed that B=E/c in the far field of the radiated lightning energy, where B is the magnetic field of the sferic. Therefore, in order to calculate W in calibrated units, we must determine the conversion factor, A_n. We could then estimate the total energy radiated at the stroke location by the following formula:

$$\varepsilon = 2\pi\rho h W(\exp(\alpha r)), \qquad (7.3)$$

where ρ is the radius of a small circle on the Earth with the lightning stroke at its center and the WWLLN receiving station on the circle, *r* is the great-circle stroke-to-receiver distance, *h* is the height of the ionosphere, *W* is the time-integrated energy flux at the receiver, and α is the attenuation of the stroke. Therefore, in order to calculate the energy radiated at the location of the stroke, we must know *r, h, W*, and α. The WWLLN location algorithm determines *r* to within 20 km, as described in Chapter 3. The height of the ionosphere, *h*, is estimated to be ~75 km in the daytime and ~85 km at

nighttime [Ferguson and Snyder, 1987]. Therefore, the remaining quantities needed to determine stroke energy are the calibrated value of the integrated energy flux density (W) and the attenuation of the signal over the propagation path (α). As mentioned above, one must determine A_n in order to determine W.

7.2.1 *Determining A_n by using narrowband VLF Transmitters*

We will use high-power, narrowband VLF transmitter signals that radiate within the bandwidth of each station (3-30 kHz) to attempt to calibrate the WWLLN stations. These transmitters are typically governmentally-run for submarine communication, and thus their transmitting power, fixed frequencies, and locations are known quantities. The call signs, locations, frequencies, and transmitting power for the transmitters used are found in Table 7-A.

Table 7-A: Call signs, locations, frequencies, and transmitting power for the narrowband transmitters.

Call Sign	Location	Latitude	Longitude	Freq. (kHz)	Power (kW)
NPM	Hawaii	21° 25' 30"N	158° 09' 20" W	21.4	500
NWC	Australia	21° 49' 01"N	114° 09' 50" E	19.8	1000

Using this known information, we use the Long-Wave Propagation Capability (LWPC), developed in Ferguson and Snyder [1987] and modified by Dr. Craig Rodger, to determine the expected RMS amplitude in μV/m of the transmitter at a given station. We then calculate the RMS amplitude of that transmitter as detected by the station in sound card units to get:

$$A_n = \frac{RMS_{\mu V/m}}{RMS_{scu}}. \tag{7.4}$$

The LWPC models the expected RMS amplitude of a narrowband frequency at a given location based on time of day and year, as the sun is the major forcing factor of ionospheric electron density variation. It does not take solar flare or other ionospheric modifications, such as lightning EMP, into account. One must keep that limitation in mind when using output from this model. To determine the calibration factor at a given

frequency, we use the estimated RMS amplitude in μV/m predicted by the LWPC for a given WWLLN station/VLF transmitter pair, and compare that value to the actual detected amplitude of that frequency band at the WWLLN station in computer sound card units (scu). The LWPC-predicted signal strength of the NPM transmitter at the Dunedin station is 422 μV/m and 1245 μV/m from the NWC transmitter.

Next, we find the measured amplitude in sound card units of these narrowband transmitters as detected by the Dunedin WWLLN station. To determine this amplitude, 15-second waveforms recorded at local noon in Dunedin for the period of 15 January 2007 to 8 March 2007 are analyzed. From each of these waveforms, we find the average RMS value of the signal in a ± 1 kHz band surrounding the center frequency of the NWC and NPM VLF transmitters. A 4^{th} order Butterworth bandpass filter with 3dB point at the transmitter frequency ± 1 kHz is used to determine the amplitude of each transmitter as measured in sound card units.

Figure 7.1 shows the average value of the amplitude of the NWC and NPM transmitters as detected at the Dunedin station in sound card units over time. The sporadic dropouts in amplitude occur when the transmitter was turned off. The error in the 15 second measurement is on the order of the size of the data points in Figure 7.1. Therefore, before 1 March 2007, the main source of variation in the RMS_{scu} amplitude is the daily variation on the order of 6% for NWC and 5% for NPM. A day-to-day variation of this magnitude is excellent for a VLF electric field antenna in the middle of a high noise area; McRae and Thomson [2000] reports a minimum variation of 0.5 to 1 dB in magnetic field amplitude as measured in a quiet location using a loop antenna. This variation is most likely caused by error in the measurement techniques in addition to ionospheric variability of 0.1 to 0.3 dB not taken into account in the LWPC model, such as solar flares and strong lightning strokes. The variation of 5-6% in RMS_{scu} amplitude will limit the accuracy to which we can know A_n.

After 1 March 2007, the amplitude of both transmitters changes dramatically. This change continues for months after 8 March 2007 and could have occurred due to a

change in the grounding of the instrument. In fact, the preamplifier in Dunedin was recently replaced due to weathering and water damage of the electronics. This damage could have caused the change in gain of the instrument. The possibility of a sudden gain change such as shown in Figure 7.1 indicates that the conversion factor should be monitored on a daily or weekly basis at each station.

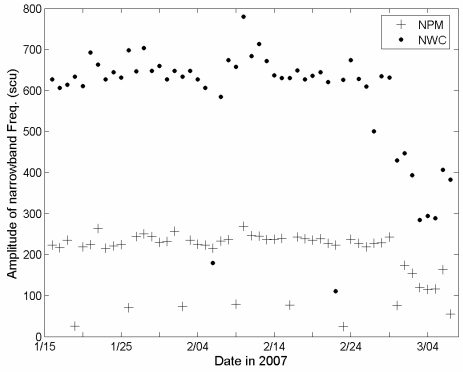

Figure 7.1: Average value of amplitude of NWC (dots) and NPM (plusses) transmitters as detected at the Dunedin station in scu over time. The daily variation in RMS amplitude is less than 6% before 1 March 2007. After 1 March 2007, the amplitude of both transmitters changes dramatically. This could be a problem with the grounding of the instrument. The semi-regular drop-outs in amplitude are due to the transmitter being turned off.

From these data, to get $A_n = \frac{RMS_{\mu V/m}}{RMS_{scu}}$, we must divide the amplitude predicted by the LWPC code by the RMS_{scu} amplitude detected at the station. The values for A_n over this period of time are shown in Figure 7.2.

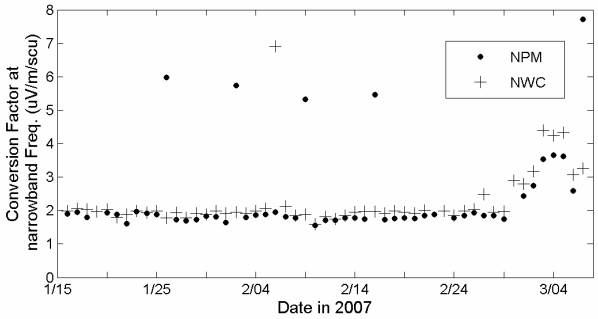

Figure 7.2: Values of $A_{Dunedin}$ over time. The conversion factors track each other well over time, adding reliability to the measurement.

The average conversion factor for 15 January to 1 March 2007, as determined by the NWC transmitter when it is turned on, is 1.94 ± 0.13 $\mu V/m$/scu. As determined by NPM, the average conversion factor is 1.81 ± 0.10 $\mu V/m$/scu. However, this conversion factor holds for the narrowband frequency of the transmitter. The next section describes the process to determine the conversion factor at 13 kHz from the conversion factors at the narrowband transmitter frequencies. We find the conversion factor at 13 kHz to determine the amplitude of the sferic, which covers the frequency range of 1 to 24 kHz. Thirteen kHz is chosen as it is the middle of the band of maximum sferic amplitude of 10-16 kHz [Dowden et al., 2002]. For that same reason, it is also the frequency for which the approximate group velocity of the sferic is used in the downhill-simplex lightning location algorithm, as is mentioned in Section 2.3.

7.2.2 *Frequency response*

Once we have determined this conversion factor at certain frequencies, we must take into account the frequency response of the WWLLN station in order to determine the conversion factor at 13 kHz. To determine if all antennas behave similarly, we have taken a frequency spectrum at the WWLLN station in Dunedin, New Zealand; the network WWLLN station in Seattle, Washington; and a test station on the roof of another building on the University of Washington campus. The Dunedin and Seattle network stations have the same VLF antenna design (wire wrapped tightly around a pole of ~1 inch diameter) but different environments. The test station antenna in Seattle has a newer design that was implemented in many of the more recently-installed WWLLN stations (2 wires, crossed at the top of the antenna, splayed out inside of a 2 to 4 inch diameter tube, and connected at the bottom of the antenna). The frequency-response study of all 3 stations was completed to determine whether the frequency response from one station could be used on all stations.

To measure these frequency spectra, we cover the antenna with a metal sleeve to shield out external electric fields. We then drive the metal sleeve with a frequency-

ramping signal generator from 1-30 kHz. The electric field capacitively couples to the antenna, similar to the way a sferic couples to the antenna. An example spectrogram from this procedure is shown in Figure 7.3, with frequency in kHz on the vertical axis, time in seconds on the horizontal axis, and intensity of the signal in dB represented by color.

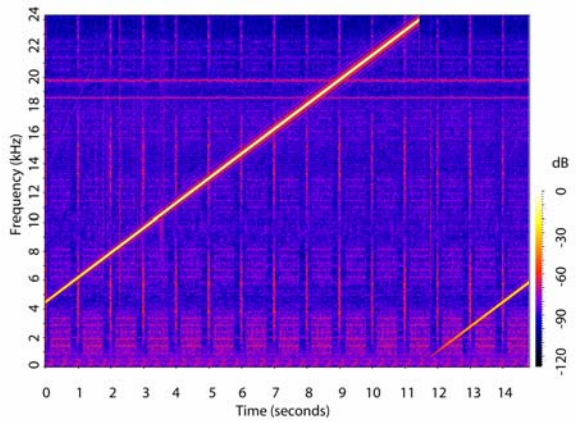

Figure 7.3: Example spectrogram of frequency calibration procedure. Vertical axis is frequency (kHz), horizontal axis is time (seconds), and color bar shows intensity of the signal (dB).

The frequency response curves for the three stations tested are shown in Figure 7.4. Dunedin has a fairly linear increase in sensitivity until about 22 kHz, and then a rapid fall-off. Seattle sensitivity peaks around 13 kHz, and then falls off rapidly, most probably due to the notch filter at 24.7 kHz.

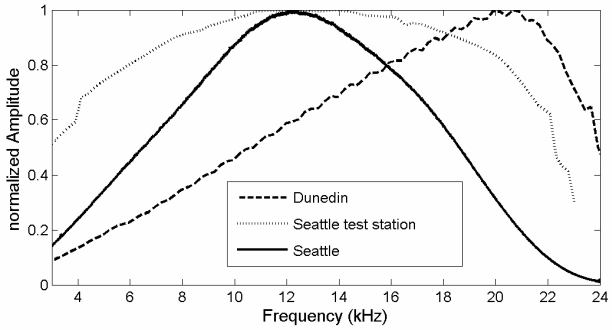

Figure 7.4: Frequency response of 3 WWLLN stations: Dunedin (dashed), Seattle (solid), and Seattle test station (dotted).

The frequency response of the preamplifier only and the computer sound card only from the test station, and then the response of the preamplifier and sound card together

are shown in Figure 7.5. The response of the Seattle test station is remarkably similar to the convolution of the two, meaning that the frequency response of the antenna in its surrounding environment is relatively flat.

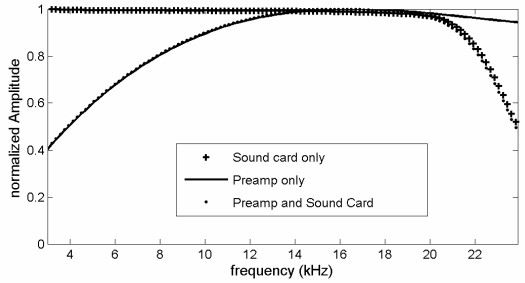

Figure 7.5: Frequency response of preamplifier only (solid line), sound card only (plusses) and preamp and sound card together (dots).

Figure 7.4 shows that the two other stations have a differently shaped response. The Seattle station has a narrowband filter to remove the aliased signal from the NLK transmitter at 24.7 kHz, which transmits from less than 100 miles away. As one can see, each station is dramatically different in frequency response, indicating that we will not be able to generalize frequency response curves to all stations. Because each station host puts up their own VLF antenna in the best possible location in their environment and provides their own computer, the differences in frequency response could arise from different antenna designs at the different stations, different electrical environments (nearby buildings, etc.), or different sound card responses. It is possible that by measuring the preamplifier response and sound card response of each station, along with the frequency response of any filters included in that station, we may be able to provide a fairly good approximation to the frequency response to each station. However, access to many of the already-installed stations is difficult, so it will be difficult to measure these quantities. It would also be difficult to compare the preamplifier/sound card convolved response to actual response for more cases by repeating the calibration procedure described above. For this reason, another method by which to determine stroke energy is developed and analyzed. This method is explained in the following section.

From the frequency response curve of the Dunedin station, we find that the conversion factor at 19.8 kHz must be multiplied by 1.61 to get 3.13 ± 0.21 $\mu V / m$ /scu at 13 kHz from NWC and 2.99 ± 0.16 $\mu V / m$ /scu from NPM, which are in agreement with one another. For lightning strokes detected by the Dunedin station during this time period, we could use these conversion factors to determine their energy flux density in absolute units. The process by which we determine the amount of radiated energy produced by these strokes will be described in Section 7.3.

7.2.3 *Summary and suggestions for the future*

Results from the frequency response analysis and the narrowband transmitter analysis are as follows: The daily ionospheric variation affects the narrowband signals as measured at WWLLN stations by as much as 6%. Stations can suddenly change in gain based on grounding factors (i.e. Dunedin). These two findings indicate that transmitter amplitudes and calibration factors should be monitored on a frequent basis. Also, the frequency response of each station needs to be monitored. We cannot simply use the frequency response curve found at one station to calibrate all the rest. It is possible that, by determining the frequency response of each station's preamplifier and sound card, we could produce a useable estimate of station frequency response. However, this may not be true if environmental factors affect the antenna frequency response. Testing all stations by shielding out the external field with a metal sleeve and driving the antenna with known frequencies is not feasible.

Two improvements to the network are suggested as solutions to these problems. One is to measure transmitter amplitude at each station on a regular basis (1-2 times per day) this will allow us to take ionospheric variability into account in the calibration factor, and it will provide an added benefit of making WWLLN a global ionospheric monitoring network. Another suggestion is to develop a small, calibrated transmitter that sweeps through frequencies and that can be run at each station to get a frequency response for each station. That transmitter could also emit a frequency wave with a

given amplitude at a certain time each day to provide a second calibration point in addition to the VLF transmitters. This calibration point would be useful in determining the system gain for each VLF station, but ultimately may not be able to decrease the error significantly in the calibration amplitude estimate due to the electrical environment of the antenna.

7.3 **Relative energy radiated as determined by a single station**

While we work on implementing the above suggestions for an absolute calibration of the stroke energy, this dissertation has addressed the question: "how big is one stroke relative to another?" If stations are not calibrated relative to one another, then we can still determine the relative energy radiated by strokes in a given storm as observed by a single station.

We look again at Equation 7.3: $\varepsilon = 2\pi\rho hW\left(\exp(\alpha r)\right) = 2\pi\rho hYA_n^{\,2}\left(\exp(\alpha r)\right)$. We do not know A_n, but all energies measured by station n will be scaled by that same factor, as well as by all other constants. Therefore, we can find a relative energy as determined by that station: $\varepsilon_{rel} = \rho Y\left(\exp(\alpha r)\right)$. (7.5)

Here we have assumed that h, the ionospheric height, is a constant, which reasonably can be assumed for a storm-to-station great circle path that does not cross the terminator. For a conservative estimate, it is required that, for the daytime ionosphere, the solar zenith angle of the stroke and the station be 70 degrees or less (0 degrees is solar noon, 90 degrees is sunset or sunrise). For the nighttime ionosphere, it is required that the solar zenith angle be 120 degrees or greater (180 degrees is solar midnight).

An example case study analyzes a conglomeration of storms off the west coast of Central America on 1 July 2007. This study was limited to strokes detected by the Sao Paulo WWLLN station between 3:00 UT and 7:30 UT. All stroke-to-receiver paths in this study are under the nighttime ionosphere, as defined above. For each stroke, ε_{rel} was determined as detected by the Sao Paulo station. That value is then divided by the

minimum value of ε_{rel} in this case study to produce a normalized value of stroke magnitude, $\varepsilon_{rel,norm}$. Figure 7.6 shows a histogram of the 509 lightning strokes that are included in the studied range, with $\varepsilon_{rel,norm}$ represented along the x-axis, and number of counts in each bin along the y-axis.

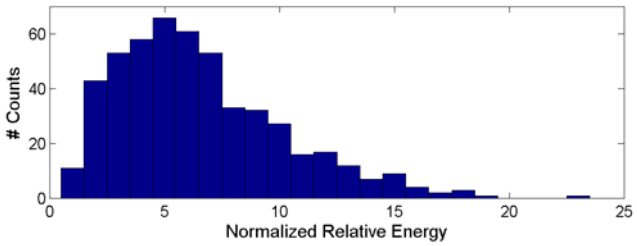

Figure 7.6: Histogram of the 509 lightning strokes in relative-energy case study. $\varepsilon_{rel,norm}$ is along the x-axis, and number of counts in each bin along the y-axis. Mean value of $\varepsilon_{rel,norm}$ is 6.6 ± 3.6.

The mean value of is $\varepsilon_{rel,norm}$ is 6.6 with a standard deviation of 3.6. Figure 7.7 is a map of the lightning strokes in this case study. Strokes with a normalized energy within one standard deviation of the mean are plotted in red, strokes more than one sigma below the mean are in blue, strokes more than one sigma above the mean are in green, and strokes more than 2 sigma above the mean are in black. The sizes of the dots represent the different magnitude ranges, although they are not to scale, relatively.

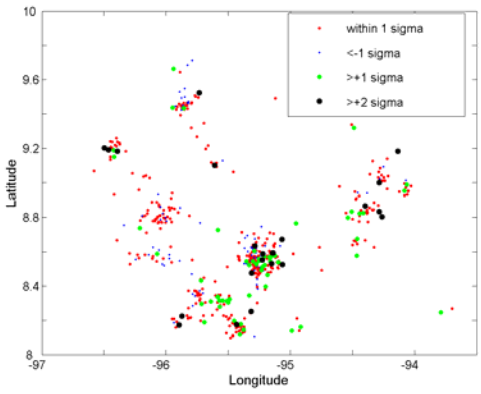

Figure 7.7: Map of lightning strokes in relative-energy case study. Strokes plotted have normalized energy within one σ of mean (red), more than one σ below mean (blue), more than one σ above mean (green), and more than 2 σ above mean (black). Sizes of the dots represent the different magnitude ranges, although they are not to scale, relatively.

This section has described a possible method for determining relative magnitudes of lightning strokes in a given storm region, a capability that could greatly enhance the utility of the network in addressing a wide range of scientific questions. As is shown in the following section, relative magnitudes determined separately from two stations agree, in that both stations find the same smaller magnitude strokes and larger magnitude strokes. The next step to verify this technique would be to compare relative magnitudes as determined by WWLLN to peak currents or charge moments of lightning located by a regional ground-based lightning detection network.

7.4 **Relative Calibration**

Section 7.3 demonstrates a method to determine relative normalized magnitudes of WWLLN lightning strokes in a given storm by using data from a single station. Next, the relative energies of a given storm detected by two different WWLLN stations are used to try to determine the relative conversion factor A_{n1}/A_{n2}, where A_{n1} is the conversion factor for station $n1$ and A_{n2} is the conversion factor for station n_2. The following analysis is performed on the same case-study storm as in Section 7.3, but here we require that each stroke be detected by the Sao Paulo station and the Cordoba, Argentina station. Since the absolute calibration factors, A_{n1} and A_{n2}, for these two stations (as discussed in Section 7.2) have not yet been resolved, the absolute energy of each stroke cannot be determined, but only the relative energy (from Section 7.3).

For example, we take the relative energy estimate from Equation (7.5) and include the calibration factor A_n. The energy estimate from the same stroke, as estimated by a second station, should be the same, since it is the same lightning stroke. We then get the following equation:

$$\bar{\varepsilon} = \rho_{n1} Y_{n1} A_{n1}{}^2 \left(\exp\left(\alpha_{n1} r_{n1}\right)\right) = \rho_{n2} Y_{n2} A_{n2}{}^2 \left(\exp\left(\alpha_{n2} r_{n2}\right)\right) \tag{7.6}$$

The unknown variables in this equation are A_{n1}, A_{n2} α_{n1}, and α_{n2}, and we hope to determine a relative calibration factor, A_{n1}/A_{n2}, by assuming values for α_{n1}, and α_{n2}. For the storm in the case study, the storm-to-receiver distance is comparable for the Sao

Paulo (~6,500 km) and Cordoba (~5,600 km) stations. Therefore, we assume that sferics propagating on each path will undergo the same attenuation of 2dB/Mm under the nighttime ionosphere [Wait, 1970]. Relative stroke energy estimates are shown in Figure 7.8. In this case, the energy estimate using $Y_{SaoPaulo}$ is plotted along the x-axis and the estimate using $Y_{Cordoba}$ is plotted along the y-axis. One can see that for large strokes, the slope increases, possibly indicating that the Sao Paulo station is reaching a maximum value in electric field. Because each station only records and transmits the time-integrated energy flux, we cannot verify this limiting hypothesis with the current information. In order to verify for certain that the Sao Paulo station was reaching a threshold, one would need to save full waveforms as detected at the station and analyze the shape of the waveforms. Without the full waveforms, the finding in this dissertation indicates either that a non-linear model for $A_{Cordoba}/A_{SauPaulo}$ may be required for larger amplitude strokes, or that this method of calibration may only be valid for smaller magnitude strokes.

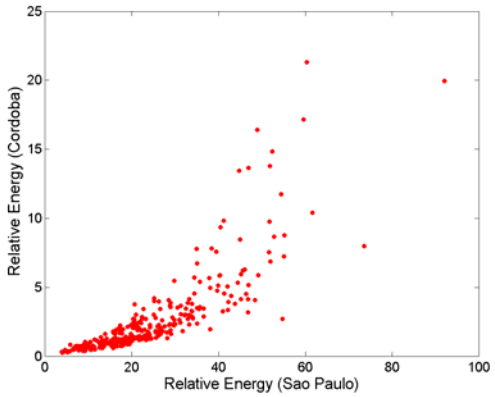

Figure 7.8: Relative stroke energy estimates from one storm detected by 2 stations. X-axis shows energy estimate using $Y_{SaoPaulo}$ and y-axis shows the energy estimate using $Y_{Cordoba}$.

Therefore, we will try to determine the best estimate for the slope for the strokes with lower amplitudes. To make this estimate, the best linear fit to points within one standard deviation of the mean is calculated. In this case, the best fit to these data points gives $A_{Cordoba}/A_{SauPaulo} = 0.091 \pm 0.004$, with an R-squared value of 0.62. The best fit for

the strokes with relative energy within one standard deviation of the mean is shown in Figure 7.9.

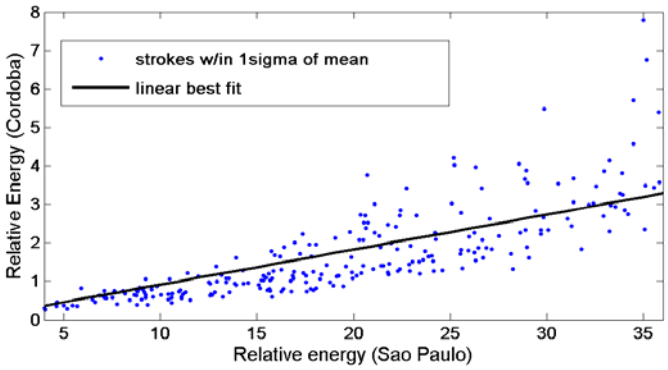

Figure 7.9 The best fit for the strokes with relative energy within one standard deviation of the mean.

The next question is, how accurate is the attenuation estimate along both great-circle paths of 2dB/Mm? To answer this question, in Figure 7.10, we plot the same lightning strokes as in Figure 7.8, overlaid with the same plot of strokes in another storm (centered on 19.5N, 74.5W) at the same time. As shown by Figure 7.10, the slope of the line, $A_{Cordoba}/A_{SauPaulo} = 0.066 \pm 0.001$, is not the same for the second storm. This finding indicates that perhaps the attenuation coefficients cannot be assumed to be the same for both these paths.

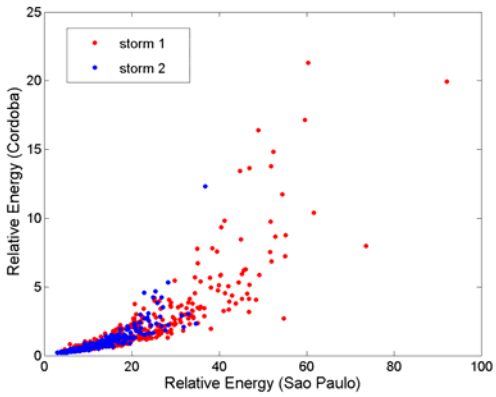

Figure 7.10: Relative stroke energy estimates from two storms detected by 2 stations. Storm 1 (in red) is the same as in Figure 7.8. Storm2 (in blue) is a storm centered on 19.5N, 74.5W that occurred at the same time as Storm 1 and was detected by the same two stations.

Next, we determine better estimates for the attenuation coefficients by using results from the LWPC code as described in Rodger et al. [2005a] in which a sample lightning stroke waveform with a peak current of 28 kA is propagated to a receiver location. This model may provide a more accurate attenuation rate of the sferic because it takes into account the ionospheric propagation conditions along specific great-circle paths instead of an averaged estimate for many propagation conditions. In this case, we propagate a typical waveform from the center of the storm region (9 N, 95.5 W for storm 1, 19.5 N, 74.5 W for storm 2) to both the Cordoba and Sao Paulo WWLLN station. Figure 7.11 shows the LWPC-predicted spectra received at these two stations for a simulated stroke at 9N, 95.5W. The vertical axis shows the magnitude of the electric field waveform at a point 110 km away from a stroke (top panel), at the Sao Paulo receiver 6472 km from the source (middle panel), and at the Cordoba receiver 5592 km from the source (bottom panel). The horizontal axis represents frequency in kHz. The stronger attenuation at the higher frequencies is evident in the bottom two panels. Each waveform is integrated over the frequency range of 2 to 24 kHz to estimate the total VLF energy received at that location. Then the attenuation in the VLF wave packet is calculated from the difference in amplitude between the VLF energy at 110 km from the source and the VLF energy at the WWLLN receiving station.

The same simulated sferic waveform is propagated from 19.5N, 74.5W to the Sao Paulo and Cordoba stations. Based on these simulation results, we find an average attenuation of 4.67 dB/Mm over the storm 1/Sao Paulo great circle path, an average attenuation of 5.08 dB/Mm over the storm 1/Cordoba path, 6.12 dB/Mm for storm 2/Sao Paulo, and 6.41 dB/Mm for storm 2/Cordoba. Error in the LWPC estimate has been determined for narrowband transmitters as between 0.5 and 1.0 dB at the receiver location. However, it is nearly impossible to experimentally determine LWPC uncertainties for broadband emitters (lightning strokes) since one typically does not know the expected amplitude in V/m at a receiving station from a lightning stroke. For

this case, we will assume that the attenuation rates for broadband emitters to be 0.5 to 1.0 dB as well.

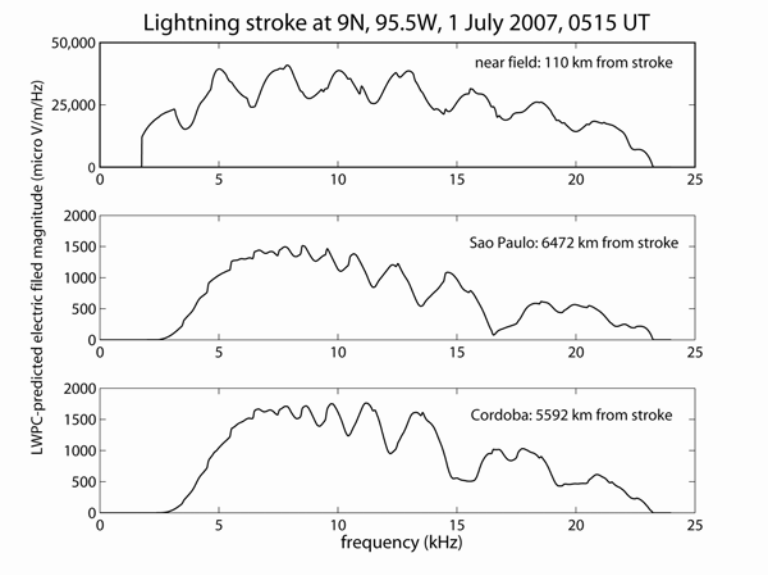

Figure 7.11: LWPC-predicted spectra for a simulated stroke at 9N, 95.5W. Vertical axis shows the magnitude of the electric field at a point 110 km away from a stroke (top panel), at the Sao Paulo receiver 6472 km from the source (middle panel), and at the Cordoba receiver 5592 km from the source (bottom panel). The horizontal axis represents frequency in kHz. The stronger attenuation at the higher frequencies is evident in the bottom two panels.

An explanation of the difference in LWPC-calculated attenuation rates from the Wait rates is that these are broadband attenuation rates as opposed to narrowband estimates from a single frequency. Also, the estimate of 2 dB/Mm from Wait [1970] is an average of the many paths and frequencies measured, but the attenuations in the many cases varied from less than 2 dB/Mm to 3 or 4 dB/Mm. In any case, the variability in these attenuation rates and the difference between these estimated rate and the previous assumed rate of 2 dB/Mm from Wait [1970] shows the sensitivity of attenuation of VLF sferics to ionospheric parameters, and better knowledge of ionospheric behavior would greatly enhance the ability to estimate stroke energy via VLF measurement of lightning sferics.

Using these new attenuation rates, code estimates A_{n1} =0.090 ± 0.004, A_{n2}= 0.084 ± 0.002. While the values of the conversion coefficient are still not equal within the

bounds of error for the two storms, the values are much closer than the first estimate that assumed an attenuation coefficient of 2 dB/Mm for each storm/station great circle path. Again, one must keep in mind that the LWPC method does not take into account sporadic disturbances to the waveguide, such as solar flares, solar proton events, or strong lightning activity. The modeled attenuation rates of 4.67 to 6.41 dB/Mm for these great circle paths may be much closer to the actual attenuation than 2 dB/Mm, but they have an estimated error of 0.5 to 1.0 dB as mentioned above. This finding indicates that before being able to calibrate the stations relative to one another, we need to better understand the ionospheric attenuation coefficient and the factors that affect that coefficient.

In summary, while we cannot determine an absolute calibration for the energy of strokes for the network, we can determine relative energy of strokes in a single storm by using data from a single station, and we have developed a method that could be used to determine relative calibration factors of WWLLN stations using 2 stations and 2 storms when a more accurate measure of ionospheric propagation effects is developed. The 2-stations-2-storms comparison shows that relative magnitudes of strokes agree when determined via energy estimates from 2 separate stations, in that both stations find the same smaller magnitude strokes and larger magnitude strokes. To improve these estimates to an absolute level, it may be a good idea to develop a well-calibrated VLF generator that can be positioned at each station to transmit a given electric field to the antenna and sweep through all 3-30 kHz. This would provide a frequency response calibration and could provide an improved value for calibration amplitude. However, there may always be a fairly high uncertainty in the absolute conversion factor due to unknown effects from the differing electrical environments for each VLF antenna.

Chapter 8: Modeling Lightning EMP/Ionospheric Interaction

8.1 **Overview**

As mentioned above, electric fields radiated by lightning can surpass required thresholds in the lower ionosphere to produce enhanced attachment, optical emissions, and ionization and many models have been developed to describe this interaction. However, the majority of EMP simulation codes only model a single lightning stroke. Recent articles suggest the possibility of accumulated electron density enhancements if the stroke rate exceeds the relaxation rate of the electron density enhancements [Barrington-Leigh and Inan, 1999; Tarenenko et al., 1993]. Rodger et al. [2001] used the model developed in Cho and Rycroft [1998] to accumulate ionization enhancements based on the peak currents of NLDN-detected strokes in the continental US. They found a possible 100% to 900% increase in conductivity in the 88 to 92 km altitude range for a period of more than an hour. However, they did not include the non-linear effect of the EMP interaction with the ionosphere. The non-linear effect refers to fact that when one lightning stroke causes enhanced ionization in a certain region, the next lightning stroke will interact in a medium with a different background electron density if enough time has not passed for the electron density to return to its original conditions. This section builds on the study of Rodger et al. [1999] by addressing non-linear effects of the lightning EMP/ionosphere interaction. This study uses the Cho and Rycroft [1998] model with a few modifications to describe the accumulated effect of strong lightning strokes on the nighttime lower ionosphere.

Section 8.2 presents the model developed in Cho and Rycroft [1998] that is used in this dissertation to describe the interaction of the ionosphere and the electromagnetic pulse radiated by lightning. Section 8.3 compares the Cho and Rycroft [1998] model to in situ rocket electric field measurements to provide the first in situ validation of an EMP model in the lower ionosphere. Section 8.4 presents a numerical method used to determine the relaxation behavior of a region of perturbed electron density. Section 8.5

presents results on accumulated electron density enhancements that consider the non-linearity of the interaction of lightning EMP with the ionosphere, and the relaxation of electron density during the inter-stroke time.

8.2 **Model Formulation**

This section describes the model developed in Cho and Rycroft [1998] to predict the interaction of the ionosphere and the electromagnetic pulse radiated by lightning. It also describes the modifications made to the nighttime background electron density profile used in the code.

This model is an axi-symmetric model that places a vertical lightning stroke at the origin. It uses the Finite Difference Time Domain technique to propagate the EM field in time and 2-dimensional space. The electric field interacts with the electrons in the ionosphere, causing attachment, recombination, optical emission, and ionization when the reduced electric field (magnitude of the electric field divided by the neutral number density) surpasses certain thresholds.

The initial cloud charge distribution governed by the following equations, with **E** as electric field, ρ_t representing the thundercloud charge density, ρ_s representing the space charge density, and $\mathbf{j_t}$ representing current density in the lightning channel:

$$\nabla \cdot \mathbf{E} = -\frac{\rho_s + \rho_t}{\varepsilon_0} \tag{8.1}$$

$$\frac{\partial \rho_s}{\partial t} + \nabla \cdot (\sigma \mathbf{E}) = 0 \tag{8.2}$$

$$\frac{\partial \rho_t}{\partial t} + \nabla \cdot (\mathbf{j_t}) = 0 \tag{8.3}$$

One can refer to Cho and Rycroft [1998] for equations for ρ_t, ρ_s, and $\mathbf{j_t}$. By integrating $\mathbf{j_t}$ one gets a current pulse shape similar to that shown in Figure 8.1. The time constant and total charge transferred can be varied in the input to the model. Figure 8.1 shows an example for a transfer of 20 coulombs of charge with a time constant of 15 μs.

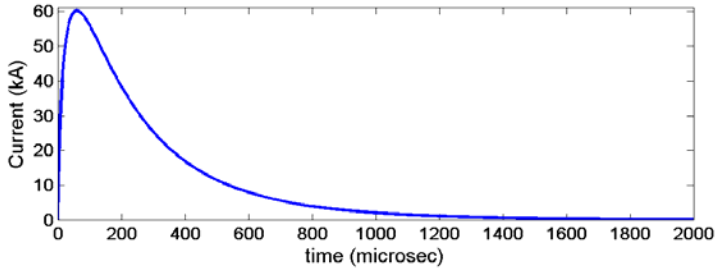

Figure 8.1: Lightning current pulse shape used in 2D-EMP model. Total charge transferred and time constant are variable inputs to the code.

The model uses the following equations to govern the propagation of the EM field in a medium:

$$\nabla \times \mathbf{E} = -\frac{\partial \mathbf{B}}{\partial t} \tag{8.4}$$

$$\nabla \times \mathbf{B} = \mu_o \varepsilon_o \frac{\partial \mathbf{E}}{\partial t} + \mu_o \mathbf{j} \tag{8.5}$$

$$\mathbf{j} = \sigma \mathbf{E} + \mathbf{j_t} \tag{8.6}$$

$$\sigma = \sigma_e + \sigma_i \tag{8.7}$$

where **E** is the electric field and **B** is the magnetic field. Constants in these equations are μ_0, the magnetic permeability of a vacuum; ε_0, the permittivity of free space, e, the electric charge of an electron; and m_e, the mass of an electron. **J** is the total current density and $\mathbf{j_t}$ is the current density of the lightning stroke. The electrical conductivity of the medium, σ is the sum of the electron and ion conductivities, σ_e and σ_i, respectively. Ion conductivity is approximated by the following function of altitude only, as the effect of the wave electric field on the ion density is insignificant:

$$\sigma_i(z) = 1.7 \cdot 10^{-13} e^{(z/7.4km)} - 2.8 \cdot 10^{-20} e^{(z/4.3km)} * e^{(z/7.0km)}. \tag{8.8}$$

Electron conductivity is given by

$$\sigma_e = e n_e \mu_e = \frac{e^2}{m_e} \frac{n_e}{n_n \langle \Theta \nu \rangle_m}, \tag{8.9}$$

where the conditions of the medium (ionospheric plasma) are n_e, electron density; n_n, neutral density; $<\theta\nu>_m$, momentum transfer collision rate in m^3/s; and σ_i, the ion

conductivity. A typical way to write electron conductivity is $en_e\mu_e$, where μ_e is the electron mobility. In Equation (8.9),

$$\mu_e = \frac{e}{m_e}\frac{1}{n_n\langle\Theta v\rangle_m} \quad . \tag{8.10}$$

The electron mobility is a decreasing function with respect to an increasing electric field because the collision frequency increases as electrons are heated. This effect is represented in the momentum transfer collision rate, $<\theta v>_m$, which is approximated from experimental measurements of electron swarms in laboratory experiments [Razier, 1991]:

$$\langle\Theta v\rangle_m = 3.2\cdot 10^{-15}\, m^3/s \quad \text{for } E/n_n < 10^{-24}\ \text{Vm}^2 \tag{8.11}$$

$$\langle\Theta v\rangle_m = 4.66\cdot 10^{-7}\left(\frac{E}{n_n}\right)^{0.34} m^3/s \quad \text{for } E/n_n \geq 10^{-24}\ \text{Vm}^2 \tag{8.12}$$

The neutral density is a function of altitude only, given by

$$n_n(z) = 2.5\cdot 10^{25}\exp(-z/h_n), \tag{8.13}$$

where h_n is the scale height for neutral density, 7 km.

The electron density is governed by the following equation:

$$\frac{\partial n_e}{\partial t} = n_n n_e\left(R_i(E/n_n) - R_a(E/n_n)\right), \tag{8.14}$$

where, n_n is the neutral number density, n_e is the electron number density, and R_i and R_a are the ionization and attachment rates, respectively.

As mentioned above, the background electron density is not well known at any particular time, and has a significant impact on the magnitude of the electric field as it penetrates the ionospheric medium. The original profile used in the Cho EMP model is given by:

$$n_e(z) = 0.08e^{(z/4.3\text{km})}\text{m}^{-3} \quad \text{for z} \leq 105 \text{ km and } n_e(\text{z} > 105 \text{ km}) = n_e(\text{z} = 105 \text{ km}). \tag{8.15}$$

For this comparison, the original electron density profile used by Cho and Rycroft [1998] in their 2-D EMP model was replaced with the electron density profile proposed

by Wait and Spies [1964], named the "Wait profile", because the Wait profile has been experimentally determined to correlate well with data [Thomson, 1993; McRae and Thomson, 2000]. The Wait electron density profile is given by:

$$n_e(z) = 7.857 * 10^{-5} e^{\beta(z-H')} \nu(z) \,(\mathrm{cm}^{-3}), \tag{8.16}$$

where z is the altitude, β is a parameter of "steepness" of the ionospheric profile (β = 0.5 determined for nighttime ionosphere) [Ferguson and Snyder, 1987], H' is 85 km for a nighttime ionosphere, and ν(z) is the collision frequency given by:

$$\nu(z) = 1.86 * 10^{11} e^{-0.15z} \,(\mathrm{s}^{-1}). \tag{8.17}$$

8.3 **In situ validation of EM code.**

Since in situ measurements of ionospheric electric fields at the 85 to 95 km altitude range can only be measured by instruments on rockets, very few measurements have been made. Therefore, this comparison is the first validation of this lightning EMP model to electric fields measured on a rocket. We have existing ac and dc electric field data from an ionospheric rocket flight from Wallops Island, VA on 2 September 1995 [Barnum, 1999]. Here, we compare model results for a -19.5 kA lightning stroke that was detected by the electric field instrument on this rocket and was located by the ground-based SUNY lightning detection network to have occurred at 37.865º latitude and -75.403º longitude at 1:22:53.257 UT. At the time of this lightning stroke, the rocket was located at 260 km horizontal distance from the stroke location at an altitude of 90 km.

Figure 8.2 shows the rocket-measured vertical electric field (solid line) radiated by this lightning stroke and the modeled electric field (using the Wait nighttime electron density profile) at the rocket location (dotted line). The modeled electric field has been filtered using an 18-kHz Butterworth filter to simulate the filter on the rocket electric-field instrument, that had a Nyquist frequency of 20 kHz. Even with the 18-kHz Butterworth filter, there was some aliasing of signals with frequencies greater than 20 kHz [Barnum 1999]. With the exception of the high-frequency initial peaks in the

modeled data, the model using the Wait profile is consistent with the measured in situ electric field in terms of timing of the pulses and the magnitude of the electric field. When comparing modeled data using the original Cho and Rycroft [1998] electron density profile, the magnitude of the model output is ~10 times larger, indicating a much lower agreement with the data.

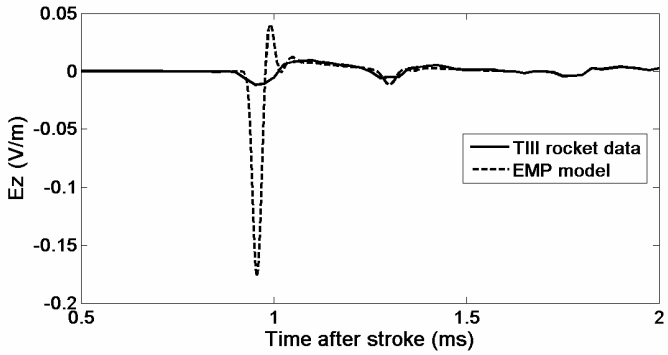

Figure 8.2: Comparison of rocket-measured vertical electric field (solid line) with 2-D EMP model output (dotted line) for a -19.5 kA CG stroke at 260 km range and 90 km altitude.

This comparison indicates that the model represents amplitude variations in time very well. There is some discrepancy at high frequencies near the beginning of the waveform, possibly due to the shape of the input current waveform or the filtering of the rocket data. By modifying the characteristic time, τ, from 15μs to 25μs, the magnitude of the initial downward peak decreases by 17% and the first upward peak decreases by 50%. By filtering the model results using a 4-kHz Butterworth filter instead of a 18-kHz filter, we get the modeled result shown in Figure 8.3. This comparison between the model results with a 4-kHz filter and the data is a much closer agreement than with the 18-kHz filter. This finding suggests that the rocket may actually be filtering off lower frequencies than reported from the pre-flight calibration.

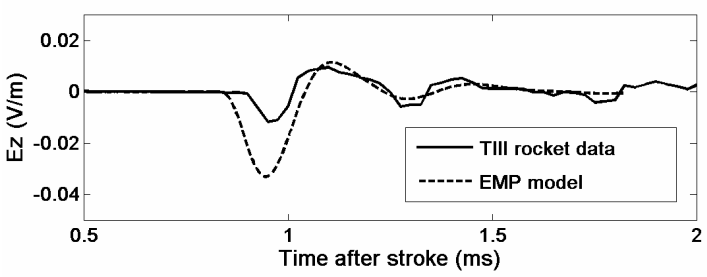

Figure 8.3: Comparison of same rocket-measured vertical electric field (solid line) with 2-D EMP model output (dotted line) as in Figure 8.2, but using a 4kHz Butterworth filter.

Another source of error in the magnitude could be the background electron density profile. While the Wait profile models the situation better than the original Cho and Rycroft [1998] profile, it most likely does not represent the actual profile perfectly, either. As is found below in Section 8.5, previous lightning strokes could modify the electron density profile so that it can no longer be represented by a simple exponential. In a test case, the 2D-EMP code was run with a background electron density of 6 times the original profile. The results showed a decrease in magnitude of electric field at 90 km by a factor of 3. This test shows that the background electron density can have a significant impact on the magnitude of the electric field at lower ionospheric altitudes. Based on these variations resulting from different input model parameters in addition to uncertainty in the validity of the 18-kHz Butterworth filter on the rocket, it is unclear whether this is a limitation of the rocket data or an error in the 2D-EMP model.

8.4 **Relaxation of enhanced electron density.**

The 2-D EMP code runs for 2 ms while the lightning stroke propagates to the lower ionosphere. After the EMP perturbation, the perturbed electron density undergoes recombination (capture of an electron by a positive ion) and attachment (electron capture by neutral molecule) and will eventually return to the original steady state electron density. A numerical solution has been determined by using a 4^{th} order Runge-Kutta method to describe nighttime relaxation of ionospheric electron density perturbations caused by an impulsive sferic. The differential equation used to describe the change in electron density in this simulation is:

$$\frac{\partial N_e}{\partial t} = q - \beta N_e - \alpha N_e{}^2 \text{ [Rodger et al. 1998],} \tag{8.18}$$

with q steady-state ionization rate due to cosmic rays, β as the attachment coefficient, α as the recombination coefficient. The value of q for steady-state is determined by setting the left-hand side of Equation (8.18) to zero. The values for α and β also are taken from Rodger et al. [1998] in which a simplified ionospheric chemistry model is described and found to give similar results to the much more complex Sodankyla Ion Chemistry model [Verronen et al., 2005]. Attachment dominates below 80 km altitude due to high concentrations of cluster ions, and recombination dominates above 85 km altitude due to high concentrations of O_2^+.

The value of β is determined as the combination of attachment coefficients for the two reactions, $O_2 + e + N_2 \rightarrow O_2^- + N_2 + 0.5\text{eV}$ and $O_2 + e + O_2 \rightarrow O_2^- + O_2 + 0.5\text{eV}$, by the equation $\beta = (\beta_1 + \beta_2)/1.4$, with β_1 for the former reaction and β_2 for the latter. β_1 is given by $\beta_1 = 1 \cdot 10^{-43}[O_2][N_2]$, where the number density of O_2 and N_2 in m^{-3} is represented by $[O_2]$ and $[N_2]$, respectively, and determined by the MSIS-E-90 ionospheric model developed by NASA Goddard Space Flight Center [Hedin et. al., 1977; http://omniweb.gsfc.nasa.gov/vitmo/msis_vitmo.html]. The value for β_2 is more complicated, and determined by the following equations:

$$\beta_2 = \beta(T_n)(1/T_e)^{0.65} \exp\left[-\frac{a_1}{T_e} - \left(\frac{a_2}{T_e}\right)^2 - \left(\frac{a_3}{T_e}\right)^3\right][O_2]^2 \tag{8.19}$$

$$\beta(T_n) = 1.1617 \cdot 10^{-39} - 3.4665 \cdot 10^{-42} T_n + 3.2825 \cdot 10^{-45} T_n{}^2 \tag{8.20}$$

$$a_1(T_n) = 7.8193 \cdot 10^2 - 3.2964 T_n \tag{8.21}$$

$$a_2(T_n) = -1.9159 \cdot 10^2 + 3.7646 T_n - 4.5446 \cdot 10^3 T_n{}^2 \tag{8.22}$$

$$a_3(T_n) = -7.6834 \cdot 10^1 + 1.2277 \cdot 10^{-2} T_n - 7.6427 \cdot 10^{-3} T_n{}^2 + 1.7856 \cdot 10^{-5} T_n{}^3 \tag{8.23}$$

where T_e is the electron temperature as determined by the MSIS-E-90 ionospheric model, and we assume T_n, the neutral temperature, is equal to the electron temperature.

Recombination reactions are dominated by hydrated cluster ions (i.e. $H^+(H_2O)_n$) for altitudes below 80 km and dominated by O_2^+ for altitudes above 80 km. The value of the recombination coefficient is approximated in Rodger et al. [1998]:

$$\alpha = 2.5 \cdot 10^{11} \sqrt{300 / T_e} \ \text{m}^3\text{s}^{-1} \text{ for z} \le 80 \text{ km}, \tag{8.24}$$

$$\alpha = 2 \cdot 10^{12} \left(T_e / 300\right)^{-0.55} \ \text{m}^3\text{s}^{-1} \text{ for z} > 80 \text{ km}. \tag{8.25}$$

Figure 8.4 shows the results of this relaxation code for a 200% enhancement in electron density at different ionospheric altitudes. At the altitudes of 85 and 90 km, relaxation to within 5% of original levels is very slow. These altitudes are also the altitudes at which the EMP has the most significant impact on electron density. From this simulation, we see that if large strokes occur more frequently than the relaxation time of the electron density enhancement, then the enhancement may accumulate over a period of a number of strokes. Subsequent strokes then will interact with a modified ionosphere, and may create non-linear behavior. This non-linear behavior will be analyzed in Section 8.5.

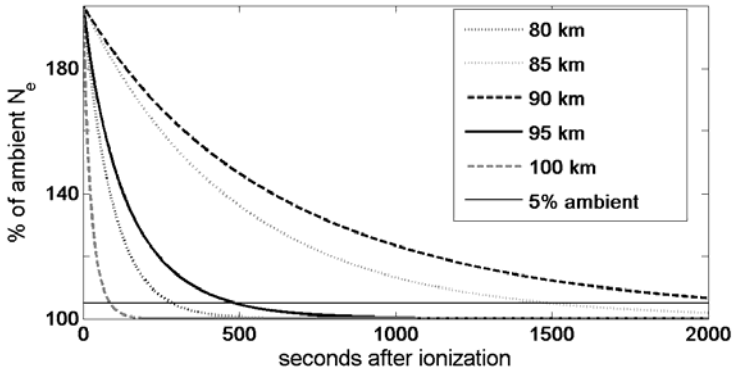

Figure 8.4: Numerically-calculated relaxation times for different altitudes for an electron density enhancement of 200%. At the altitudes of 85 and 90 km, relaxation to within 5% of original levels is 1500 seconds or longer.

8.5 **Accumulated enhancements due to successive lightning strokes.**

In the following simulation, the above-described 2-D EMP model predicts the change in electron density due to lightning EMP. The electron density enhancement then is allowed to relax for a time *t* via the above numerical method. Next, the 2-D EMP

model simulates a second lightning stroke occurring at a time *t* after the first and interacting with the modified ionosphere. This process is repeated nine times to simulate 10 successive lightning strokes. This is the first time the non-linearity of the interaction is taken into account in this type of simulation.

Lightning flash rates from storm 1 in Section 7.4 are used to determine the time between strokes, *t*, to be used in this simulation. The detection efficiency of ~4% calculated by Jacobson et al. [2006] for the southeast U.S. is used to estimate a stroke rate of 2 strokes per second during the peak of the storm for a period of 20 minutes. Based on findings in Golde [1977] and Rakov and Uman [2003], Rodger et al. [2005b] approximated a function to describe the probability that a lightning stroke could be larger than a given peak current. The cumulative probability versus lightning peak current in kA is approximated by the curve in Figure 8.5.

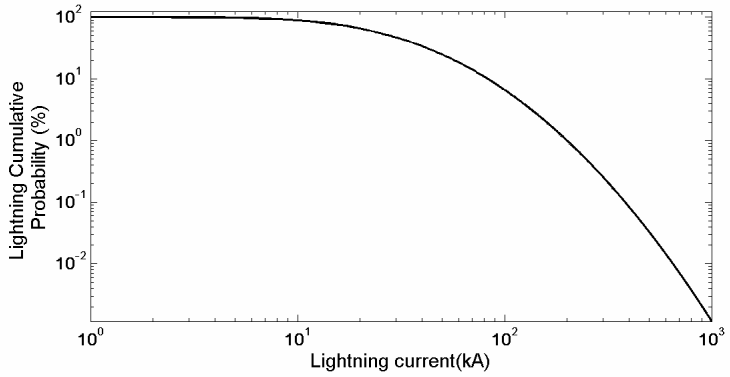

Figure 8.5: Cumulative lightning probability vs. lightning peak current (in kA), reproduced from Rodger et al., [2005], based on results from Golde [1977].

The 2-D EMP simulation results show a minimum peak current of 100 kA in order to produce any increase in electron density in the lower ionosphere. From the cumulative lightning peak current probability [Rodger et al., 2005] shown in Figure 8.5, we find that approximately 5% of all WWLLN-detected strokes have peak current greater than 100 kA and ~2.5% of all strokes have peak current greater than 150 kA. These results are used to calculate the estimated WWLLN stroke rate for strokes with 150 kA or greater. This cutoff is chosen so that half of all strokes that cause electron

density enhancements have peak currents larger than 150 kA and half have peak currents less than 150 kA. The estimated stroke rate of 150-kA-or-greater strokes in storm 1 is 0.2 s^{-1}, or 1 every 5 seconds. For this simulation, a 150-kA stroke excites the ionospheric electron density using the 2-D EMP simulation, and then the electron density relaxes for 5 seconds via the numerical method described in the previous section before the next 150-kA stroke occurs at the same location. For real lightning locations, subsequent strokes would not occur in exactly the same location, but most probably within the storm region of 30-50 km. This initial simplification is used since we are focused on investigating the non-linear affect of successive strokes. Hopefully, this will extend to a more realistic case in the future.

Figure 8.6 shows the steady-state electron density profile (right side), along with the electron density profile after one 150-kA stroke (left side, top panel) and after ten 150-kA strokes (left side, bottom panel), spaced 5 seconds apart. Figure 8.7 shows the percent change in electron density from steady-state for the same two simulation cases. After one stroke, the maximum change in electron density is 34%, and occurs at 88.5 km altitude and 103 km range. After ten strokes, the maximum percentage change is 295% at an altitude of 87 km and a range of 103 km. It is also apparent that the space around the region of enhanced electron density actually has a slight decrease in electron density, and the region near the horizontal origin (in the electrostatic field of the stroke) has a substantial decrease in electron density.

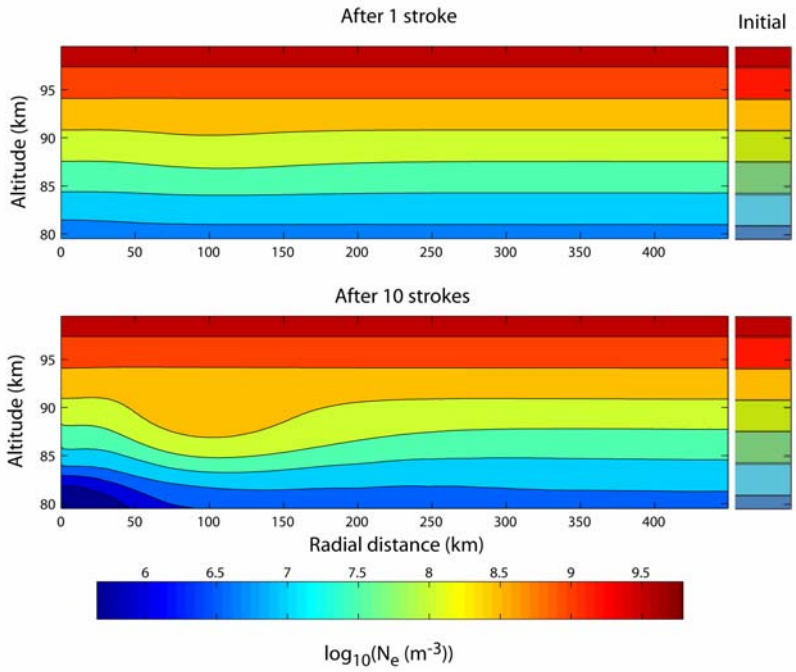

Figure 8.6: Initial, or steady-state, electron density profile (right side), along with the electron density profile after one 150-kA stroke (top panel) and after ten 150-kA strokes (bottom panel), spaced 5 seconds apart.

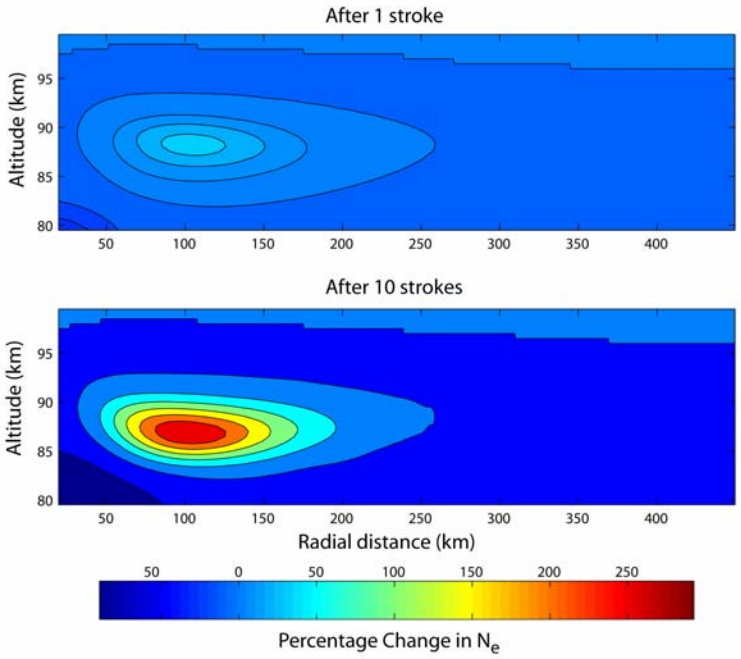

Figure 8.7: Percentage change in electron density from steady-state after one 150 kA stroke (top panel) and after ten 150 kA strokes (bottom panel).

Figure 8.8 shows the electron density at 92, 90, 88, and 85 km altitude and Figure 8.9 shows the percentage change in electron density at these altitudes after each successive stroke. The non-linear behavior of the effect of EMP on the medium is clear at all altitudes. At 92 km altitude, the electron density approaches a limit of ~5.45 x 10^8 m^{-3}, or about a 13% increase. The electron density at 90 km seems more slowly to approach a limit of ~100% increase. The increase in electron density at 88 km appears to be the most linear, with an increase of ~250% over 10 strokes. The change in electron density per stroke at 85 km actually increases as the number of successive strokes grows. Based on results from 90 and 92 km, one might expect electron densities at 85 and 88 km to reach limits eventually, but they show no sign of converging within these 10 strokes. Over 10 successive strokes, the electron density at 85 km increases 183%.

An explanation of processes underlying this behavior is the following: The amount of ionization at a particular location due to a lightning stroke is dependent on the magnitude of the electric field at that location, and electric fields that surpass an ionization threshold increase electron density. However, the magnitude of the electric field is dependent on the conductivity, which is in turn directly dependent on electron density. Because the relaxation times for enhanced electron density are slow, as shown in Figure 8.4, an electron density enhancement may remain when the next stroke occurs. This enhancement leads to increased conductivity of the medium. As conductivity increases, the electric field of the wave attenuates to a greater degree as it passes through the medium. At some point, the medium reaches a limit where conductivity is too high to allow the electric field to penetrate with enough amplitude to reach the ionization threshold, and therefore, the electron density does not increase past that point. At 92 km altitude, that limit seems to be reached at an electron density of ~5.45 x 10^8 m^{-3}. At 85 km, the rate of electron density increase is actually higher for subsequent lightning strokes. An explanation of this effect is that 85 km is near the lower boundary of the region of electron density enhancement. Below the region of enhancement, a region of decreased electron density develops over successive strokes as shown in

Figure 8.7. The lower region of decreased electron density allows the radiated electric field to penetrate to 85 km altitude with less attenuation.

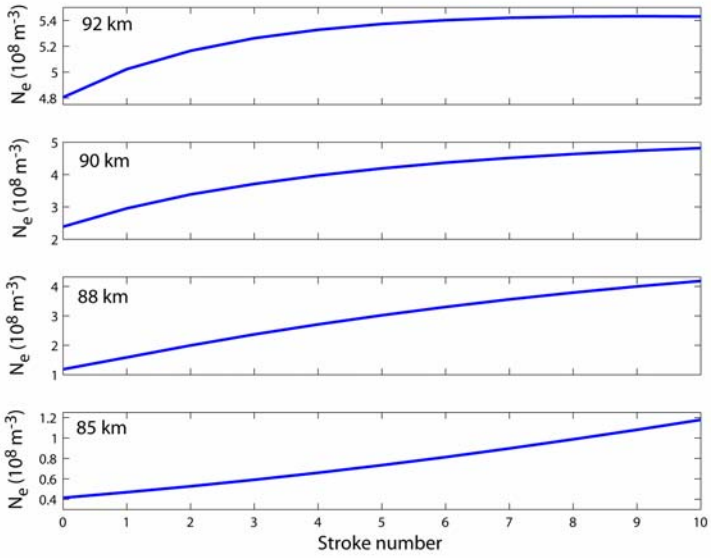

Figure 8.8: Electron density at 92, 90, 88, and 85 km altitude after each successive stroke.

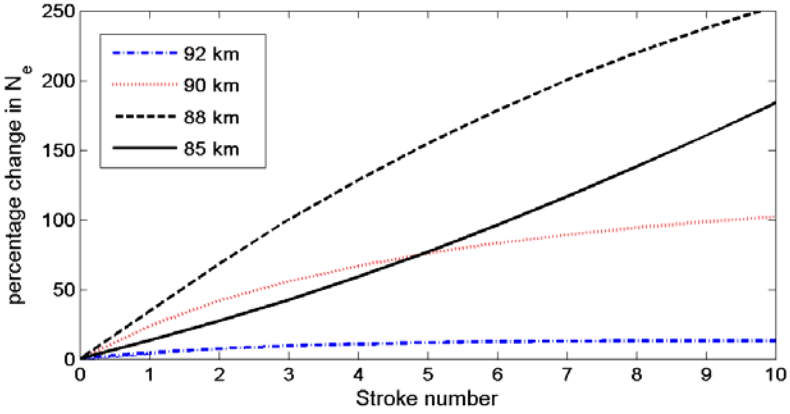

Figure 8.9: Percent change in electron density for 92, 90, 88, 85 km altitude after each successive stroke.

In order to investigate the dependence of the model output on the input electron density profile, we ran the 10 successive stroke 2D-EMP model for an initial electron density profile with the parameters H' = 85 km and $\beta = 0.4$ km^{-1}, instead of the original profile of H' = 85 km and $\beta = 0.5$ km^{-1}. This creates a background electron density profile with the same characteristic height, but with a less steep increase in electron

density with altitude. This profile is chosen to compare to the background electron density profile found just before the elve-producing perturbation measured in Cheng et al. [2006].

Figure 8.10 shows a perturbed electron density profile taken vertically at the range of maximum percentage change after 1 stroke (Figure 8.10a) and after 10 strokes (Figure 8.10b) for both the original electron density profile ($\beta = 0.5$ km^{-1}; dotted line) and the new electron density profile ($\beta = 0.4$ km^{-1}; solid line). One can see from Figure 8.10b that despite the different starting profiles, the perturbed profile in both cases begins to reach the same electron density in the region between 83 and 91 km altitude. This indicates that the electron density limit in the 83 to 91 km range seems to be independent of initial electron density.

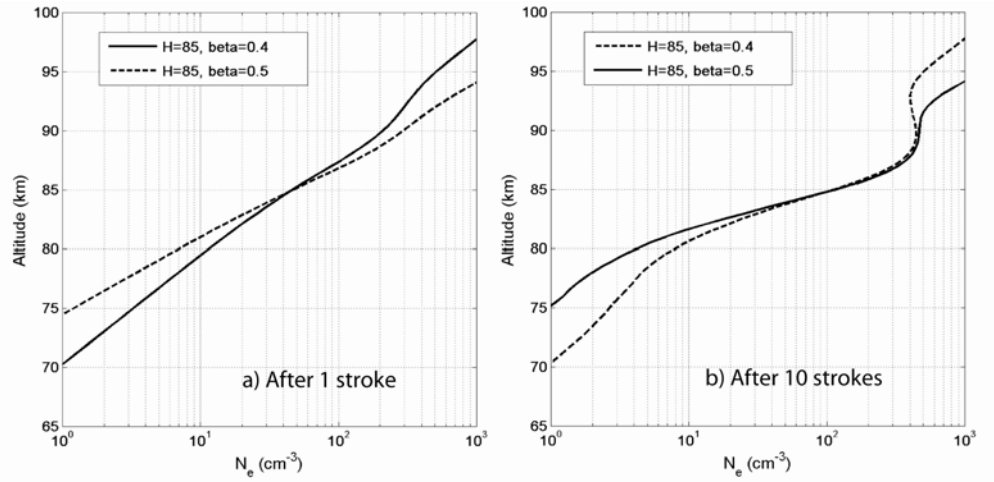

Figure 8.10: Perturbed electron density profile taken vertically at the range of maximum percentage change after a) 1 stroke and b) 10 strokes for 2 initial electron density profiles (solid and dotted lines).

From the profiles in Figure 8.10, we can compare 2D-EMP model results to empirically-based calculations of ionospheric modifications due to lightning from Cheng et al. [2006] that were made using the remote sensing technique presented in Cummer et al. [1998]. This technique detects long-path VLF radiation from lightning strokes before and immediately after a strong elve-producing lightning stroke in the path. By working with the received VLF spectrum and the LWPC model for ionospheric propagation, they iteratively recover the parameters H' and β for a Wait

electron density profile in the VLF propagation path following the technique presented in [Cheng and Cummer, 2005]. Using this technique, Cheng et al. [2006] found a background Wait electron density profile with values of H'=85 km and β=0.4 immediately before an elve-producing lightning stroke. The error in their method is estimated at 0.2 km in H' and 0.01 km^{-1} in β [Cummer et al., 1998]. Cheng et al. [2006] also statistically analyzes the effects on lower ionospheric electron density of 27 lightning strokes with peak current >60 kA.

Figure 4a of Cheng et al. [2006] presents a perturbed electron density profile associated with an elve-producing lightning stroke estimated by the NLDN to have -106 kA peak current. They find that this lightning stroke causes an enhancement in electron density between 88 and 96 km altitude, with a 2-fold increase at ~92 km. It also creates a decrease in electron density between 78 and 88 km, with a 5-fold decrease at ~82 km. Figure 4b of Cheng et al. [2006] presents an averaged perturbed profile for the 27 averaged lightning strokes with mean peak current -79 kA. They find that these strokes cause an average enhancement in electron density between 83 and 95 km altitude, with a 2-fold increase at ~88 km. These strokes also create an average decrease in electron density between 75 and 83 km, with a 1.5-fold decrease at ~80 km.

Although the background electron density profiles are different, with the background profile of the solid line in Figure 8.10a being closer than that of the dotted line to the background profile in Figure 4b of Cheng et al. [2006], the perturbed profile in Figure 8.10a of this dissertation (modeled 1 -150 kA stroke) is similar to the profile (in terms of regions and magnitudes of increase and decrease) for the averaged strokes of -79 kA presented in Figure 4b of Cheng et al. [2006]. This signifies that the model may underestimate the perturbed change in electron density for a lightning stroke of a given peak current. In this case, a -150 kA stroke models a perturbation that represents the experimentally determined perturbation for strokes with an average peak current of -79 kA. The perturbed profile in Figure 8.10b (modeled 10 -150 kA strokes) is slightly larger in magnitude than the perturbation due to one elve-producing lightning stroke

shown in Cheng et al. [2006] Figure 4a. Also, after 10 strokes the modeled electron density enhancement has moved lower than that shown in Figure 4a of Cheng et al. [2006], which is consistent with the findings presented above that successive lightning strokes effectively move the region of enhanced electron density lower in altitude as the electron density at higher altitudes reaches a limiting amount.

In the following paragraphs, we will discuss some of the remaining uncertainties that could be producing these discrepancies between the empirically-based calculations of electron density perturbations and the 2D-EMP modeled results. Peak currents estimated by the NLDN are noted to have uncertainties of at least 20% to 30% [Cummins et al., 1998]. This uncertainty could modify the 2D-EMP estimate of electron density enhancement by a factor of 3 because of a larger radiated electric field from the lightning stroke. Another source of error is the description of the lightning stroke current pulse. By narrowing the pulse, dI/dt increases (where I is the current in the stroke), and, therefore, the radiated electric field increases because it is dependent on dI/dt. A change in the width of the pulse by 10 μs can increase the magnitude of the electric field in the EMP by 30%. Uncertainty in peak current and in dI/dt could increase or decrease the electric field of the lightning radiation that is responsible for ionization and attachment as it passes through the lower ionosphere.

Another source of error may be the overall shape of the lightning current pulse. In a recent study, Frey et al. [2005] found that 50% of ISUAL-detected elves were accompanied by a lightning stroke with a β-type stepped leader. The stepped leader is one of the original stages of a lightning stroke in which a conducting path is created between cloud and ground in a number of discrete steps. The β-type stepped leaders are characterized by long, bright steps with higher average speed than the more typical α-type stepped leader. In an electric field waveform associated with a β-type stepped leader, a series of bipolar pulses are evident about 2 to 5 ms before the return stroke [Rakov and Uman, 2003]. It is possible that this β-type leader radiation could be a factor in the total lightning EMP electron density modification. This leader activity has

not been included in the simple current pulse of the modeled return stroke, and could be a cause of the discrepancy between the experimentally-based estimates of electron density enhancement and the modeled electron density enhancement.

In addition to error in the magnitude of the electric field, there could be error in the reduced electric field thresholds for ionization and attachment. The thresholds used in the Cho and Rycroft [1998] model were determined in laboratory electron swarm experiments. It is possible that the real world case (ionospheric plasma) behaves differently than the controlled experiment. Therefore, the thresholds for ionization may be different than those used in the model. This error could cause an underestimate in ionization even if the magnitude of the electric field were correct. These uncertainties reveal the need for more in situ measurements to better understand the many unknown quantities in this type of ionospheric research. Bearing these uncertainties in mind, it is possible that the 2-D EMP code underestimates the electron density enhancements in the lower ionosphere.

The findings based on this model suggest that one must take the non-linearity into account when modeling the effect of successive strokes on lower ionospheric nighttime electron densities. It also shows that the non-linear behavior is different at different altitudes. A maximum electron density limit is reached after fewer strokes for higher altitudes than lower altitudes. The region with the most significant effect (88 km) does not seem to reach an electron density limit for these ten strokes. The limiting modeled electron density profile is the same in the 83 to 91 km altitude range regardless of the initial electron density. The non-linearity suggests that a linear approach, such as that in Rodger et al. [2001] may significantly overestimate the change in electron density at higher altitudes and underestimate it at lower altitudes. One must also remember that in general the Cho and Rycroft [1998] model may underestimate changes in electron density. However, this simulation describes qualitative behavior of electron density enhancements at different altitudes due to multiple successive lightning strokes.

Chapter 9: Conclusion and Future Work

9.1 **World-Wide Lightning Location Network Characterization**

During the course of this dissertation research, the World-Wide Lightning Location Network has developed from a fledgling network of 13 stations world wide with little known about its behavior and characteristics to a much better characterized network with fairly uniform global coverage by 30 stations. This research has provided preliminary location and timing accuracy, detection efficiency, and lightning-type studies, finding excellent location and timing accuracy, even in a worst-case scenario. The lightning-type studies using FORTE RF data indicated that WWLLN detects in-cloud lightning that are most likely NBEs, but only 3 such events were found in a 49-day case study of LASA waveforms of WWLLN-detected events in the Great Plains region. This finding indicates that either NBEs radiate more energy from Austral-asian storms, similarly energetic NBEs are more likely to be detected by 5 WWLLN stations due to higher station density, or NBEs comprise a smaller percentage of total lightning in the Great Plains. The relative detection efficiency world-wide has been characterized in comparison to the FORTE PDD instrument. Global relative detection efficiency in combination with localized regional detection efficiencies led to normalized WWLLN global lightning count rates for the first time, as shown in Chapter 4.

However, we must continue work to determine the dynamic detection efficiency of WWLLN as new stations are added. The study of station detection range, presented in Section 3.4, shows that we must include day/night differences in lightning propagation to VLF stations as well as the near-range detection voids in a reliable model of dynamic detection efficiency.

In addition to these improvements in the characterization of the network, the first attempts were made at providing an estimate of stroke energy. We found that WWLLN could be used to provide relative stroke energies for lightning in the same storm, but there are still some obstacles to overcome in determining an absolute lightning energy

calibration. The main two obstacles are determining the gain and frequency response of each VLF station and better understanding ionospheric propagation of lightning energy in different ionospheric conditions.

9.2 **Findings on energetic events correlated with lightning**

In this dissertation, WWLLN was used to investigate spacecraft-detected elves and TGFs. We have been able to use WWLLN to help better locate ISUAL-detected elves by exposing an error in the location-estimating algorithm for the spacecraft data. More accurate elve locations could allow a more accurate study of differences in elves that occur over water and over land. WWLLN is able to detect elve-causative lightning world-wide, and now could be used to determine the relative strength of lightning stroke as compared to non-elve-producing strokes in the same storm.

Lightning locations from WWLLN were able to help address some of the questions regarding terrestrial gamma-ray flashes. These data were able to provide the first evidence that TGFs are not narrowly beamed from the source. WWLLN data were also used to determine that RHESSI-detected TGFs are most likely associated with the first stroke in a lightning flash, and with large peak current lightning (greater than 40 kA).

The analysis presented in this dissertation provides the first global study of regional differences in lightning count rates versus local time using continuous ground-based data. The findings from WWLLN agree well with satellite averages over the whole world, but also provide new information on the amount of lightning over each continent under the nighttime ionosphere. We find that over 60% of lightning in the Americas occur under the nighttime ionosphere while less than 40% of lightning in Europe occurs during that time. We are also able to provide global mapping of nighttime lightning for different seasons without the need for many years of averaging, as is required by satellites. As mentioned in the previous section, a dynamic detection ability that considers the diurnal and spatial variability in WWLLN sensitivity would greatly enhance the usefulness of WWLLN data in addressing these types of studies. With such

capabilities, WWLLN could provide information on regions of the ionosphere most likely to be associated with conductivity variations, and in which one would be most likely to detect TLEs during a field campaign.

9.3 **Modeling of lightning electromagnetic pulse**

This dissertation has described a 2D-EMP model to predict the lightning-to-ionosphere energy coupling. Cho and Rycroft [1998] has shown that optical emissions as simulated by this model are consistent with observations of elves. The first in situ comparison of modeled data with rocket-measured electric fields has been performed. This comparison shows that the temporal extent of the modeled pulse is similar to the rocket-measured electric field pulse, but the high frequency peak of the modeled electric field is about 10 times larger than the rocket-measured electric field pulse. It is unclear whether this is a limitation of the rocket data or an error in the 2D-EMP model.

A comparison of the modeled electron density enhancements to experimentally-estimated enhancements [Cheng et al., 2006] has shown that the model underestimates electron density enhancements in the 85 the 95 km altitude range for a -150 kA stroke. Therefore, one must not consider modeled results as quantitative truth, but may use them to determine qualitatively how the EMP from successive lightning strokes couples to the lower ionosphere. In this light, we find that the EMP from successive strokes interacts non-linearly with the ionospheric plasma. The maximum electron density is reached earlier for higher altitudes, yet the region with the most significant affect (88 km) behaves fairly linearly for these ten strokes. The maximum modeled electron density profile is the same in the 83 to 91 km altitude range regardless of the initial electron density. The non-linearity suggests that the results in Rodger et al. [2001] may significantly overestimate the change in electron density at higher altitudes and underestimate it at lower altitudes.

9.4 **Future Work**

9.4.1 *WWLLN Characterization*

The work in this dissertation has provided much improvement in the characterization of WWLLN detection efficiency, but a concrete global estimate of WWLLN detection efficiency still must be completed. One beneficial study would be to determine the detection efficiency by comparing WWLLN to the yearly averaged OTD satellite-detected lightning count rate globally. This comparison requires a collaboration with member of the OTD team, and will only provide an annual detection efficiency estimate relative to a 5-year average, not a dynamic estimate. However, this comparison would be highly beneficial to WWLLN. Next, one must support the findings from the OTD/WWLLN comparison with a determination of the day/night dynamics in detection efficiency as well as changes in detection efficiency as more stations are added and as stations sporadically go off the air due to loss of power or internet connectivity. An expansion of the study of station detection range presented in Section 3.4 could be used for this project. Also, a better characterization of the threshold trigger levels at each individual station would be useful to achieve this goal.

An improved estimate of radiated stroke energy could be provided by determining a more accurate absolute calibration for each WWLLN VLF station, in conjunction with a better understanding of daily ionospheric variations. This dissertation has proposed the possibility of transmitting the amplitude of narrowband VLF transmitters as detected by WWLLN stations to the central processing computer. This would effectively create a global ionospheric monitoring network out of the already existing WWLLN, which could in turn be used as input to a dynamic detection efficiency estimate.

By using either the relative stroke energy as determined by the method proposed in this dissertation or an improved absolute energy estimate, correlation studies between radiated energy per stroke and elves/TGFs could provide more information about the

strength of lightning required to produce such events, and allow WWLLN data to be used to more accurately predict where these lightning-produced energetic effects will occur.

9.4.2 *Lightning/Ionospheric Coupling*

Given the difficulty of experimentally determining lower ionospheric electron densities, it is nearly impossible to verify a model of the lightning EMP effect on the lower ionosphere. However, further study using the remote sensing technique of Cheng and Cummer [2005] in the VLF band and of Jacobson et al. [2007] in the LF (30-300 kHz) band would be valuable.

Modeling of lightning/ionospheric coupling will continue to be useful while experimental measurements are difficult. It would be useful to improve the lightning EMP/ionosphere model by more accurately determining uncertainties. The model should also be modified to predict electron density variations based on WWLLN lightning counts, locations, and stroke radiated energy. A model of this sort could provide a real-time estimate of ionospheric regions likely to be perturbed by lightning activity. Such a model would have to be based on improved estimates of WWLLN stroke radiated energy as well as on results of the 2D-EMP successive-strokes model. In order to make real-time predictions without overwhelming computer time, one could use the results from Section 8.5 to estimate equations for the non-linear behavior of electron density enhancements for various altitudes.

9.4.3 *Narrow Bipolar Events*

The findings in this dissertation regarding NBEs are somewhat contradictory, given that a comparison with satellite RF measurements indicated a large number of WWLLN-detected NBEs while comparisons with a ground-based regional network indicated very few coincident NBEs. It may be useful to probe this question further by studying coincidences with ground-based regional networks for a longer period of time,

as well as for different regions. Once may be able to determine if WWLLN is more likely to detect NBEs at different times of year and in certain regions.

It may also be useful to use the LASA-detected lightning waveform, and, using the LWPC, propagate radiation from that wave to all WWLLN stations that detected the lightning stroke. This simulation could provide an idea of the trigger thresholds at different stations for detecting NBEs.

9.4.4 *Global electric circuit*

While this dissertation has not investigated the hypothesis of the global electric circuit, the global circuit hypothesis is a main motivation for providing a better characterization of WWLLN. With a dynamic detection efficiency estimate of WWLLN, one could begin a real-time study of measuring global lightning variations simultaneously with fair weather return current.

Similarly, the improvements of WWLLN presented in this dissertation hopefully will allow WWLLN data to be used to address many atmospheric electricity and meteorological questions.

REFERENCES

Barnum, H.B. (1999), Electromagnetic and optical characteristics of lightning measured in the Earth's ionosphere, Ph.D. thesis, Univ. of Washington, Seattle, Washington.

Barrington-Leigh, C.P. and U.S. Inan. (1999), Elves triggered by positive and negative lightning discharges. *Geophys. Res. Letters, 26*, 6, 683-686.

Barrington-Leigh, C.P., U.S. Inan, M. Stanley, and S.A. Cummer (1999), Sprites Triggered by Negative Lightning Discharges, *Geophys. Res. Lett.*, 26(24), 3605–3608.

Boccippio, D.J., K. Driscoll, W. Koshak, R. Blakeslee, W. Boeck, D. Buechler, H. Christian, and S. Goodman (2000a), The Optical Transient Detector (OTD): Instrument characteristics and cross-sensor validation. *J. Atmos. Oceanic Tech.*, *17***,** 441-458.

Boccippio, D.J., S.J. Goodman, and S. Heckman (2000b), Regional differences in tropical lightning distributions. *J. Appl. Meteor.*, *39***,** 2231-2248.

Boeck, W.L., O.H. Vaughan Jr., R.J. Blakeslee, B. Vonnegut, M. Brook, and J. McKune (1995), Observations of lightning in the stratosphere, *J. Geophys. Res.*, 100(D1), 1465–1475.

Budden, K.G. (1961), *The Waveguide Mode Theory of Wave Propagation.*, Logos Press, London.

Cheng, Z., and S.A. Cummer (2005), Broadband VLF measurements of lightning-induced ionospheric perturbations, *Geophys. Res. Lett.,* 32, L08804, doi:10.1029/2004GL022187.

Cheng, Z., S.A. Cummer, D.N. Baker, and S.G. Kanekal (2006), Nighttime D region electron density profiles and variabilities inferred from broadband measurements using VLF radio emissions from lightning, *J. Geophys. Res.,* 111, A05302, doi:10.1029/2005JA011308.

Cho, M and M.J. Rycroft (1998), Computer simulation of the electric field structure and optical emission from cloud-top to the ionosphere, *J. of Atmos. and Solar-Terr. Phys.,* 60, 871-888.

Christian, H.J., R.J. Blakeslee, S.J. Goodman, D.A. Mach, M.F. Stewart, D.E. Buechler, W.J. Koshak, J.M. Hall, W.L. Boeck, K.T. Driscoll, and D.J. Boccippio (1999), The Lightning Imaging Sensor. *11th International Conference on Atmospheric Electricity*, Global Hydrology and Climate Center, NASA Marshall Space Flight Center, Huntsville, Alabama.

Christian, H.J., R.J. Blakeslee, D.J. Boccippio, W.L. Boeck, D.E. Buechler, K.T. Driscoll, S.J. Goodman, J.M. Hall, W.J. Koshak, D.M. Mach, and M.F. Stewart (2003), Global frequency and distribution of lightning as observed from space by the Optical Transient Detector, *J. Geophys. Res.*, *108*(D1), 10.1029/2002JD002347.

Crombie, D.D. (1964), Periodic fading of VLF signals received over long paths during sunrise and sunset. Journal of Research National Bureau of Standards, *Radio Science*, 68D, 27-34.

Cummins, K.L., M.J. Murphy, E.A. Bardo, W.L. Hiscox, R. Pyle, and A.E. Pifer (1998), Combined TOA/MDF technology upgrade of U.S. National Lightning Detection Network. *J. Geophys. Res.*, *103***,** 9035-9044.

Cummer, S.A., Inan, U.S. and Bell, T.F. (1998), Ionospheric D region remote sensing using VLF radio atmospherics. *Radio Science* **33**, pp. 1781–1792.

Cummer, S.A., and W.A. Lyons (2005), Implications of lightning charge moment changes for sprite initiation, *J. Geophys. Res*., 110, A04304, doi:10.1029/2004JA010812.

Cummer, S.A., Y. Zhai, W. Hu, D.M. Smith, L.I. Lopez, and M.A. Stanley (2005), Measurements and implications of the relationship between lightning and terrestrial gamma ray flashes, *Geophys. Res. Lett.*, 32, L08811, doi:10.1029/2005GL022778.

Dowden, R.L., J.B. Brundell, and C.J. Rodger (2002), VLF lightning location by time of group arrival (TOGA) at multiple sites. *J. Atmos. Solar-Terrest. Phys.*, *64***,** 817-830.

Dwyer, J.R., and D.M. Smith (2005), A comparison between Monte Carlo simulations of runaway breakdown and terrestrial gamma-ray flash observations, *Geophys. Res. Lett., 32,* L22804, doi:10.1029/2005GL023848.

Ferguson, J.A., and F.P. Snyder (1987), The segmented waveguide program for long wavelength propagation calculations. Technical Document No. 1071, Naval Ocean Systems Center, San Diego, California, USA.

Fernsler, R.F. and H.L. Rowland (1996), Models of lightning-produced sprites and elves, *J. Geophys. Res.,* 101(D23), 29,653-662.

Fishman, G.J., P.N. Bhat, R. Mallozzi, J.M. Horack, T. Koshut, C. Kouveliotou, G.N. Pendleton, C.A. Meegan, R.B. Wilson, W.S. Paciesas, S.J. Goodman, H.J. Christian (1994), Discovery of intense gamma-ray flashes of atmospheric origin, *Science, 264*, 5163: 1313-1316.

Frey, H.U., S.B. Mende, S.A. Cummer, A.B. Chen, R.R. Hsu, H.T. Su, Y.S. Chang, T. Adachi, H. Fukunishi, and Y. Takahashi (2005), Beta-type stepped leader of elve-producing lightning, *Geophys. Res. Lett.*, 32, L13824, doi:10.1029/2005GL023080.

Fukunishi, H., Y. Takahashi, M. Kubota, K. Sakanoi, U.S. Inan, W.A. Lyons (1996), Elves: Lightning-induced transient luminous events in the lower ionosphere, *Geophys. Res. Lett.*, *23*, 16, 2157-2160.

Fullekrug, M., and S. Constable (2000), Global triangulation of intense lightning discharges, *Geophys. Res. Lett.*, 27, 333-336.

Goldberg, R.A., J.R. Barcus, L. Hale, S.A. Curtis (1986), Direct observation of magnetospheric electron-precipitation stimulated by lightning, *J. of Atmos. And Terr. Phys., 48* (3), 293-299.

Golde, R.H. (1977), *Lightning*, Academic Press, London, UK.

Hedin, A.E et al. (1977), A Global Thermospheric Model Based on Mass Spectrometer and Incoherent Scatter Data MSIS, 1, N_2 Density and Temperature, *J. Geophys. Res.*, 82(16), 2139–2147.

Helliwell, R.A., Katsufrakis, J.P. and Trimpi, M.L. (1973), Whistler-induced amplitude perturbations in VLF propagation. *J. Geophys. Res.* **78**, pp. 4679–4688.

Holzworth R.H, R.M. Winglee, B.H. Barnum, Y.Q. Li, and M.C. Kelley (1999), Lightning whistler waves in the high-latitude magnetosphere, *J. Geophys. Res., 104*, A8, 17369-17,378.

Holzworth, R.H., E.A. Bering III, M.F. Kokorowski, E.H. Lay, B. Reddell, A. Kadokura, H. Yamagishi, N. Sato, M. Ejiri, H. Hirosawa, T. Yamagami, S.Torii, F. Tohyama, M. Nakagawa, T. Okada, and R.L. Dowden (2005a), Balloon observations of temporal variation in the global circuit compared to global lightning activity, *Advances in Space Res., 36,11*, 2223-2228.

Holzworth, R.H., M.P. McCarthy, J.N. Thomas, J. Chin, T.M. Chinowsky, M.J. Taylor, and O. Pinto Jr. (2005b), Strong electric fields from positive lightning strokes in the stratosphere, *Geophys. Res. Lett.*, 32, L04809, doi:10.1029/2004GL021554.

Inan, U.S., T.F. Bell, J.V. Rodriguez (1991), Heating and ionization of the lower ionosphere by lightning, *Geophys. Res. Lett., 18,* 705-708.

Jacobson, A.R., R. Holzworth, J. Harlin, R. Dowden, and E. Lay (2006), Performance Assessment of the World Wide Lightning Location Network (WWLLN), Using the Los Alamos Sferic Array (LASA) as Ground Truth, *J. Atmos. and Oceanic Technology*, *23*, 1082-1092.

Jacobson, A.R., R. Holzworth, E. Lay, M. Heavner, and D.A. Smith (2007), Low-frequency ionospheric sounding with Narrow Bipolar Event lightning radio emissions: regular variabilities and solar-X-ray responses, *Ann. Geophys.,* 25, 2175–2184.

Kelley, M.C., C.L. Siefring, R.F. Pfaff, P.M. Kintner, M. Larsen, R. Green, R.H. Holzworth, L.C. Hale, J.D. Mitchell, and D. LeVine (1985), Electrical measurements in the atmosphere and the ionosphere over an active thunderstorm. 1. Campaign overview and initial ionospheric results, *J. Geophys. Res., 90*, A10, 9815-9823.

Kirkland, M.W., D.M. Suszcynsky, J.L.L. Guillen, and J.L. Green (2001), Optical observations of terrestrial lightning by the FORTE satellite photodiode detector. *J. Geophys. Res.*, *106***,** 33,499-33,509.

Lay, E.H., R.H. Holzworth, C.J. Rodger, J.N. Thomas, O. Pinto, Jr., and R.L. Dowden (2004), WWLL Global Lightning Detection System: Regional Validation Study in Brazil, *Geophys. Res. Lett., 31*, L03102, doi: 10.1029/2003GL018882.

Le Vine, D.M. (1980), Sources of the Strongest RF Radiation From Lightning, *J. Geophys. Res.*, 85(C7), 4091–4095.

Li, Y.Q., R.H. Holzworth, H. Hu, M. McCarthy, R.D. Massey, P.M. Kintner, J.V. Rodrigues, U.S. Inan, and W.C. Armstrong (1991), Anomalous optical events detected by rocket-borne sensor in the WIPP campaign, *J. Geophys. Res., 96*, A2 1315-1326.

Light, T.E., S.M. Davis, W. Boeck, A.R. Jacobson (2003), Global nighttime lightning flash rates and characteristics observed with the FORTE satellite, *Los Alamos National Laboratory technical report*, LA-UR 03-5909.

MacGorman, D.R., and R.W. Rust (1998), *The Electrical Nature of Storms,* Oxford University Press, Oxford.

McRae, W.M. and N.R Thomson (2000), VLF phase and amplitude: daytime ionospheric parameters. *J. of Atmos. and Solar-Terr. Physics* **62** 7, pp. 609–618.

Mende, S.B., H.U. Frey, R.R. Hsu, H.T. Su, A.B. Chen, L.C. Lee, D.D. Sentman, Y. Takahashi, and H. Fukunishi (2005), D region ionization by lightning-induced electromagnetic pulses, *J. of Geophys. Res., 110*, A11312, doi:10.1029/2005JA011064.

Nesbitt, S.W. and E.J. Zipser (2003), The Diurnal Cycle of Rainfall and Convective Intensity according to Three Years of TRMM Measurements. *J. of Climate*, *16*, 1456-1475.

Orville, R.E. and G.R. Huffines (2001), Cloud-to-Ground Lightning in the United States: NLDN Results in the First Decade, 1989–98. *Monthly Weather Rev., 129***,** 1179-1193.

Parkinson, W.C, and O.W. Torrenson (1931), The diurnal variation of the electrical potential of the atmosphere over the oceans, Compt. Rend. De l'Assemblee de Stockholm, 1930; IUGG (sect. *Terres. Magn. Electr. Bull.* 8, 340-345.

Pasko, V.P, U.S. Inan, T.F. Bell, and Y.N. Tarenenko (1997), Sprites produced by quasi-electrostatic heating and ionization in the lower ionosphere, *J. of Geophys. Res., 102*, A3, 4529-4561.

Petersen, W.A. and S.A. Rutledge (2001), Regional variability in tropical convection: Observations from TRMM. *J. Climate*, *14***,** doi:10.1175/1520-0442.

Pinto, I.R.C.A., and O. Pinto Jr.(2003), Cloud-to-ground lightning distribution in Brazil, *J. Atmos. Solar-Terr. Physics*, 65(6): 733-737.

Pinto, Jr. O., I.R.C.A. Pinto, and K.P. Naccarato (2007), Maximum cloud-to-ground lightning flash densities observed by lightning location systems in the tropical region: A review, *Atmos. Res.,* 84(3): 189-200.

Pinto, Jr. O., I.R.C.A. Pinto, J.H. Diniz, A.C. Filho, A.M. Carvalho, and L.C.L. Chechiglia (2003), A long-term study of the lightning flash characteristics in the southeastern Brazil, *J. Atmos. Solar-Terr. Physics*, 65(6): 739-748.

Rakov, V.A. and M.A. Uman (2003), Lightning: Physics and Effects. Cambridge University Press. Cambridge, United Kingdom.

Razier, Y.P. (1991), *Gas Discharge Physics*, Springer-Verlag, Berlin.

Roble, R.G. and I. Tzur (1986), The global atmospheric-electrical circuit. *In The Earth's Electrical Environment, Studies in Geophysics*, pages 206-231. National Academy Press, Washington, DC.

Rodger, C.J., O.A. Molchanov, and N.R. Thomson (1998), Relaxation of transient ionization in the lower ionosphere, *J. Geophys. Res.*, 103(A4), 6969–6975.

Rodger, C.J. (1999), Red sprites, upward lightning, and VLF perturbations, *Rev. Geophys*., 37, 317-336.

Rodger, C.J., M. Cho, M.A. Clilverd, and M.J. Rycroft (2001), Lower ionospheric modification by lightning-EMP: Simulation of the night ionosphere over the United States. *Geophys. Res. Lett.*, *28*(2), 199-202.

Rodger, C.J., J.B. Brundell, R.L. Dowden, and N.R. Thomson (2004), Location accuracy of long distance VLF lightning location network. *Ann. Geophys.*, *22***,** 747-758.

Rodger, C.J., J.B. Brundell, and R.L. Dowden (2005a), Location accuracy of VLF World Wide Lightning Location (WWLL) network: Post-algorithm upgrade. *Ann. Geophys.*, *23***,** 277-290.

Rodger, C.J., M.A. Clilverd, N.R. Thomson, D. Nunn, and J. Lichtenberger (2005b), Lightning driven inner radiation belt energy deposition into the atmosphere: regional and global estimates, *Ann. Geophys.*, 23, 3419-3430.

Rodger, C.J., S.W. Werner, J.B. Brundell, N.R. Thomson, E.H. Lay, R.H. Holzworth, and R.L. Dowden (2006), Detection efficiency of the VLF World-Wide Lightning Location Network (WWLLN): Initial case study, *Ann. Geophys.,* 24, 3197-3214.

Schlegel, K., G. Diendorfer, S. Thern, and M. Schmidt (2001), Thunderstorms, lightning and solar activity - Middle Europe, *J. Atmos. Sol.-Terr. Phys.*, *63*, 1705-1713.

Sentman, D.D., E.M. Wescott, D.L. Osborne, D.L. Hampton, and M.J. Heavner (1995), Preliminary Results from the Sprites94 Aircraft Campaign: 1. Red Sprites, *Geophys. Res. Lett.*, 22(10), 1205–1208.

Smith, D.A., X.M. Shao, D.N. Holden, C.T. Rhodes, M. Brook, P.R. Krehbiel, M. Stanley, W. Rison, and R.J. Thomas (1999), A distinct class of isolated intracloud lightning discharges and their associated radio emissions, *J. Geophys. Res.*, 104(D4), 4189–4212.

Smith, D.A., K.B. Eack, J. Harlin, M.J. Heavner, A.R. Jacobson, R.S. Massey, X.M. Shao, and K.C. Wiens (2002), The Los Alamos Sferic Array: A research tool for lightning investigations, *J. Geophys. Res.,* 107(D13), 4183, doi:10.1029/2001JD000502.

Smith, D.M., L.I. Lopez, R.P. Lin, C.P. Barrington-Leigh (2005), Terrestrial gamma-ray flashes observed up to 20 MeV, *Science,* 307, 5712, 1085 – 1088, DOI: 10.1126/science.1107466.

Smith, D.M., J.R. Dwyer, B.W. Grefenstette, B.J. Hazelton, Y. Yair, J. Bor, E.H. Lay, R.H. Holzworth (2007), *Eos Trans. AGU, 88*(52), Fall Meet. Suppl., Abstract AE31A-0051

Stanley, M.A., X.M. Shao, D.M. Smith, L.I. Lopez, M.B. Pongratz, J.D. Harlin, M. Stock, and A. Regan (2006), A link between terrestrial gamma-ray flashes and intracloud lightning discharges, *Geophys. Res. Lett*., 33, L06803, doi:10.1029/2005GL025537.

Suszcynsky, D.M., M. Kirkland, P. Argo, R. Franz, A. Jacobson, S. Knox, J. Guillen, J. Green, and R. Spalding (1999), Thunderstorm and lightning studies using the FORTE optical lightning system (FORTE/OLS), *Proceedings of the 11th International Conference on Atmospheric Electricity,* edited by H. Christian, *NASA/CP-1999-209261*, 672-675.

Suszcynsky, D., A. Jacobson, J. Fitzgerald, C. Rhodes, E. Tech, and D. Roussel-Dupre (2000a), Satellite-based global lightning and severe storm monitoring using VHF receivers. *EOS, Trans. Am. Geophys. Union*, *81***,** F91.

Suszcynsky, D.M., M.W. Kirkland, A.R. Jacobson, R.C. Franz, S.O. Knox, J.L.L. Guillen, and J.L. Green (2000b), FORTE observations of simultaneous VHF and optical emissions from lightning: Basic Phenomenology. *J. Geophys. Res.*, *105***,** 2191-2201.

Suszcynsky, D.M., T.E. Light, S. Davis, M.W. Kirkland, J.L. Green, and J. Guillen, (2001), Coordinated Observations of Optical Lightning from Space using the FORTE Photodiode Detector and CCD Imager. *J. Geophys. Res.*, *106***,** 17,897-17,906.

Tapia, A., J.A. Smith, M. Dixon (1998), Estimation of convective rainfall from lightning observations, *Journal of Appl. Meteor., 37*, 1497-1509.

Tarenenko, Y.N., U.S. Inan, and T.F. Bell (1993), Interaction with the lower ionosphere of electromagnetic pulses from lightning: heating, attachment, and ionization, *Geophys. Res. Lett., 20,* 15, 1539-1542.

Taylor, M., M. Bailey, P. Pautet, S. Cummer, N. Jaugey, J. Thomas, N. Solorzano, F. Sao Sabbas, R. Holzworth, O. Pinto Jr., and N. Schuch (2008), Rare Measurements of a Sprite with Halo Event Driven by a Negative Lightning Discharge Over Argentina, *Geophys. Res. Lett.,* doi:10.1029/2008GL033984, in press.

Thomson, N.R. (1993), Experimental daytime VLF ionospheric parameters. *Journal of Atmospheric and Terrestrial Physics* **55** 2, pp. 173–184.

Verronen, P.T., A. Seppälä, M.A. Clilverd, C.J. Rodger, E. Kyrölä, C.F. Enell, T. Ulich, and E. Turunen (2005), Diurnal variation of ozone depletion during the October–November 2003 solar proton events, *J. Geophys. Res.,* 110, A09S32, doi:10.1029/2004JA010932.

Volland, H. (1984), *Atmospheric Electrodynamics*, Springer-Verlag, New York.

Wait, J.R. (1970), *Electromagnetic Waves in Stratified Media*, Pergamon Press Inc., New York.

Wait, J.R. and K.P. Spies (1964), Characteristics of the Earth-Ionosphere Waveguide for VLF Radio Waves, *Nat. Bureau of Standards Tech. Notes*, 300, Washington, DC.

Whipple, F.J.W., and F.J. Scrase (1936), Point discharge in the electric field of the Earth, *Geophys. Memoirs (London) VIII*(68), 20.

Wiens, K.C., T. Hamlin, J. Harlin, and D.M. Suszcynsky (2008), Relationships among Narrow Bipolar Events, ‘‘total’’ lightning, and radar-inferred convective strength in Great Plains thunderstorms, *J. Geophys. Res*., 113, D05201, doi:10.1029/2007JD009400.

Willett, J.C., J.C. Bailey, and E.P. Krider (1989), A Class of Unusual Lightning Electric Field Waveforms With Very Strong High-Frequency Radiation, *J. Geophys. Res.*, 94(D13), 16,255–16,267.

Williams, E., K. Rothkin, D. Stevenson, and D. Boccippio (2000), Global Lightning Variations Caused by Changes in Thunderstorm Flash Rate and by Changes in the Number of Thunderstorms. *J. of Applied Meterology*, *39*, 2223-2230.

Wilson, C.T.R. (1920), Investigation on lightning discharges and on the electric field of thunderstorms. *Phil. Trans. A 221*, 73-115.

Zajac, B.A. and S.A. Rutledge (2001), Cloud-to-ground lightning activity in the contiguous United States from 1995 to 1999. *Monthly Weather Rev., 129 (5),* 999-1019.

Appendix A: Schematics for WWLLN Service Unit and Preamplifier

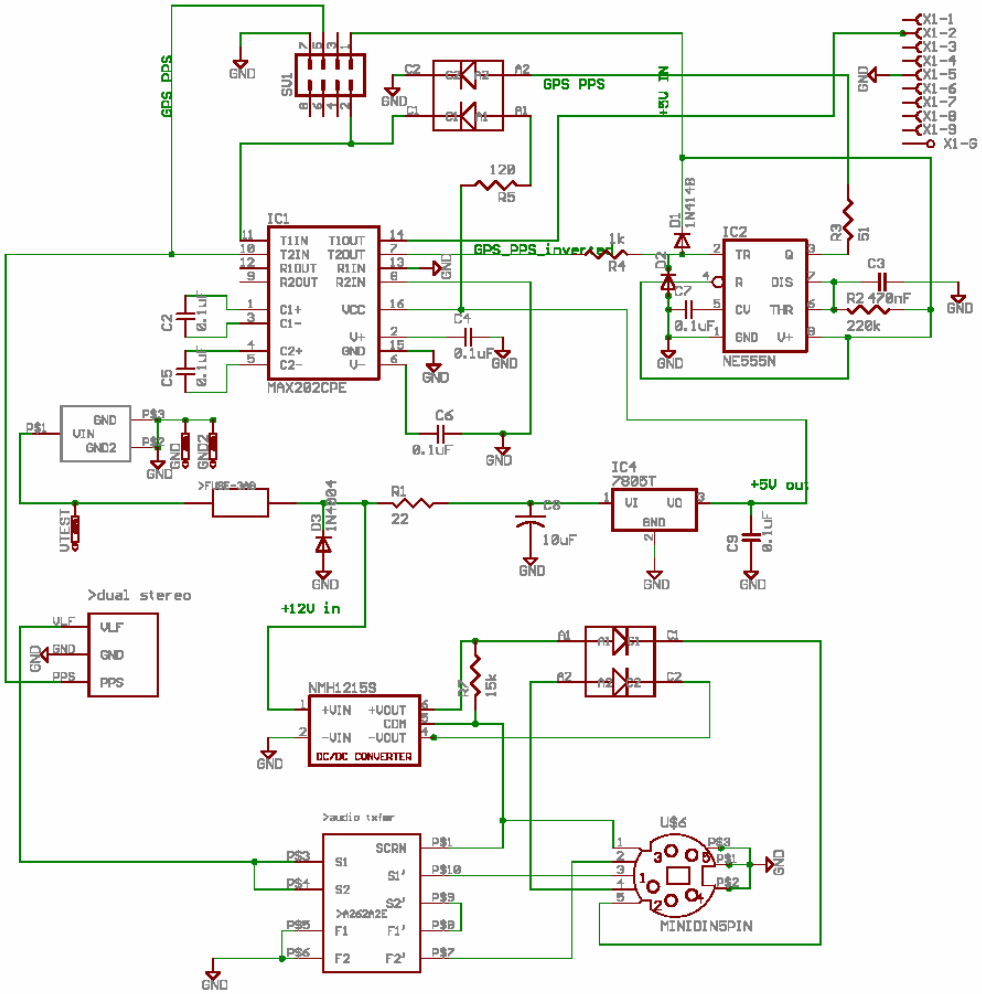

Figure A.1: Schematic for WWLLN Service Unit

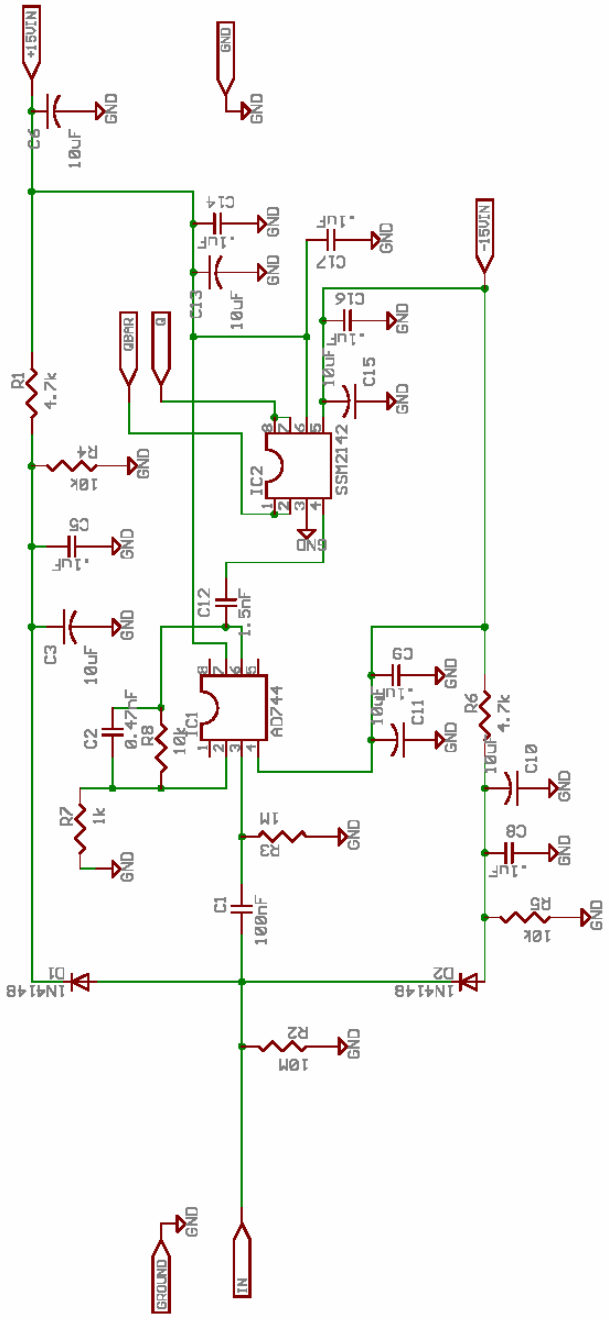

Figure A.2: Schematic for WWLLN preamplifier

VITA

Erin Hoffmann Lay

Degrees Earned:

Bachelor of Arts, Physics
Grinnell College, Grinnell, IA
Spring 2002

Master of Sciences, Physics
University of Washington, Seattle, WA
Fall 2003

Doctor of Philosophy, Physics
University of Washington, Seattle, WA
Spring 2008